Vibrational Entropy Contributions to the Phase Stability of Iron- and Aluminum-Based Binary Alloys

Thesis by
Tabitha L. Swan-Wood

In Partial Fulfillment of the Requirements
for the Degree of
Doctor of Philosophy

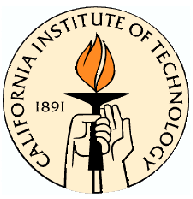

California Institute of Technology
Pasadena, California

2006

(Defended August 12, 2005)

Acknowledgements

Brent Fultz is a brilliant scientist, but that is not what set him apart from other advisors at Caltech to me. It was his wonderfully supportive nature as an advisor that drew my attention. He has always been encouraging. I am constantly impressed by the amount of faith he has in his students. His confidence in us helps us have confidence in ourselves. I am grateful to have had the privilege of being advised by Brent. His gentle guidance not only taught me practically everything I know about our research but has also helped to make my graduate experience a very enjoyable one.

I am indebted to all the scientists before me, on whose shoulders I have stood to carry out my work, most recently Peter Bogdanoff and Mike Manley.

My time at Caltech would have been much more boring without all my colleagues there who have also become my good friends. Their company and help I appreciate immensely. Olivier Delaire, you have had many wonderful insights into our work. You have also made all those long research trips a blast. Max Kresch, you are a great person and scientist and you have made many valuable contributions to our work. I will continue to treasure my friendship with you and Nessie and I am really going to miss our lunches together! Rebecca Stevens and Matt Lucas I wish you all the best for your future! Jiao Lin, Alex Papandrew, Joanna Dodd, and Ryan Monson, it has been wonderful to work with you; our conversations have been enlightening and, more importantly, enjoyable! Mike McKerns, Tim Kelley, Carol Garland, and Channing Ahn, your guidance has been as invaluable as your friendship has been delightful. I will miss you all and I have no doubt that you will all have marvelous futures.

There is no one in my life who has been a stronger influence than my wonderful mother. She has always been and forever will be my dear friend, my advisor, and my cheerleader. I am extraordinarily lucky to have such an amazing mom.

I would never have chosen to go into physics without my father. His love of math and physics ignited my interested in the field. His enthusiasm and support of my major has always been a comfort.

I am blessed to have Greg in my life, and even more so as my husband and best friend. He is always there to prop me backup when I am feeling down. His love for me is unconditional

and he is filled with kindness. Greg is always there with good advice and insightful thoughts when I talk to him about my research. Finding Greg was the luckiest thing that ever happened to me and marrying him was the smartest.

From childhood playmates to best friends as adults, my dear sister has filled my life with love. I am grateful to have such a loving sister who is always there for me.

I was so very lucky to grow up with my grandmother, lovingly dubbed "Mamo," as a next-door neighbor. I have countless memories of fresh-picked fruit and homemade treats. She is a strong and caring woman who I admire and dearly love. Family has been a strong and wonderful influence in my life; I owe all of my family a great deal of thanks.

I have a great appreciation for my previous advisors: Prof. Beyermann, a great friend and mentor, who spent countless hours chatting with me as an energetic undergraduate–if he ever regretted his open door policy, he never let it show; Prof. Ellison, who gave me a chance to experience high energy physics; Dr. Camparo, who was a wonderful mentor and friend–my summer at the Aerospace Corp. taught me a great deal about industrial and atomic physics; and Dr. Orbach, who is not only brilliant but completely endearing. He and his darling wife are incredibly enthusiastic, supportive, and sweet to his students; I often think of them and smile.

To my dear dear friends: Erin who is practically a sister; Jason, Shana, Happy, Geeti, Dave, Terri, and Tracy, your friendship has meant so much to me.

Vibrational Entropy Contributions to the Phase Stability of Iron- and Aluminum-Based Binary Alloys

by

Tabitha L. Swan-Wood

In Partial Fulfillment of the
Requirements for the Degree of
Doctor of Philosophy

Abstract

This work considers phonon entropy effects on phase stability of three binary alloys: Fe-Cr, FeAl, and Al-Ag. In all cases the vibrational entropy plays an interesting role.

The phonon density of states was measured on body-centered cubic $Fe_{0.50}Cr_{0.50}$ prepared as a solid solution, and in increasingly un-mixed states induced by annealing the solid solution at 773 K. Mössbauer spectrometry was used to characterize the extent of decomposition after annealing. A neutron-weight correction was performed, using results from the Mössbauer spectra and recent data on inelastic nuclear resonant scattering from ^{57}Fe-Cr. The vibrational entropy of decomposition was found to be –0.17 $\pm$ 0.01 $k_B/atom$, nearly equal to the change in configurational entropy after spinodal decomposition. Vibrational entropy has a large effect on the critical temperature for spinodal decomposition in equi-atomic $Fe_{0.50}Cr_{0.50}$.

The vibrational entropy of formation of vacancies in FeAl is studied in detail. Born von Kármán calculations show that the point defects due to vacancy formation have a strong stiffening effect on one of the transverse acoustic branches in the (1 1 0) direction. The vibrational entropy of vacancy formation is measured to be –0.75 k_B/vacancy.

The anharmonic vibrational entropy of FeAl is measured in the temperature range of 10 K to 1323 K. It is shown that there is an abnormally large softening between 10 K and 300 K, which is attributed to a local magnetic moment corresponding to Fe anti-site defects at 10 K. Also measured is an anomalously small anharmonic entropy between 300 K and 1323 K. This could be caused by thermal vacancies and point defects.

The anharmonic entropy of $Al_{0.40}Ag_{0.60}$ have been measured to be extremely large between 20 °C and 520 °C. The origins of this anharmonicity are unclear. The anharmonic entropy of $Al_{0.93}Ag_{0.07}$ between 20 °C and 520 °C was found to be fully described by lattice expansion. A large Ag resonance peak was measured in $Al_{0.93}Ag_{0.07}$ at 20 °C. The Mannheim method was used to show that this peak could make a large contribution to the increased solubility of Ag in Al at high temperatures.

Contents

List of Figures

List of Tables

Chapter 1

Introduction

1.1 Phase Equilibria: *To BCC, or not to BCC, that is the question...*

1.1.1 The State of Equilibrium

Throughout your life you have experienced systems in and out of equilibrium. The research presented in this work is primarily focused on equilibrium states. Let's briefly examine the state of equilibrium.

A system reaches equilibrium once the macroscopic parameters do not experience time evolution. Within the volume of the equilibrium system, there are no gradients in the intensive variables of the system (T, P, μ). If there happened to be gradients in the intensive variables, thermodynamic forces would work to reduce these gradients to zero. Thus, these forces would work to bring the system to a state of equilibrium.

The equilibrium state is the most energetically favorable state available to the system. A system that is out of equilibrium will evolve toward equilibrium. The driving force for this transformation is derived from the requirement that the system minimize its free energy.

1.1.2 Free Energy

The free energy of solid-state phases at atmospheric pressure are described by the Gibb's Free Energy to be precise. However, because the volume changes of a solid are small enough to be negligible and can therefore be described by the Helmholtz Free Energy,

$$F = E - TS \,, \tag{1.1}$$

where E is the total internal energy, T is the temperature, and S is the total entropy. The usual contributions to the total entropy can be divided into two groups: static and dynamic. There are two typical static contributions, atomic configurational and magnetic configurational. The dynamic contributions are: vibrational, magnetic, and electronic. Usually these dynamic components are independent of each other (or orthogonal). However, in special cases there can be coupling between these components (phonon-phonon, electron-phonon, etc.). For nonmagnetic systems there are no magnetic contributions to the total entropy. The electronic contributions to the total entropy are generally small in magnitude due to the Fermi temperature being significantly larger than the temperature of the transformation.

1.2 Calculating Phase Diagrams

1.2.1 Starting with the Free Energy

The ability to accurately calculate phase diagrams has been the goal of a great deal of research. Much progress has been made toward this goal. Materials systems are complicated, however, making accurate calculations hard to achieve and leaving many questions unanswered.

Phase diagrams are derived from free energy minimization calculations. Of all the phases available to the system, the phase with the lowest free energy will be the equilibrium phase. The calculation of a eutectic phase diagram (lovingly referred to here as the bunny diagram) is shown in Fig. 1.1. If two phases are available to our binary alloy, $A_{1-\chi}B_{\chi}$, at temperature T_c, then for $\chi \leq c_1$ the α phase has the smallest free energy and therefore will be the equilibrium phase; likewise for $\chi \geq c_2$ the equilibrium phase will be β. In the region where $c_1 < \chi < c_2$, both the α and β phases will be present with a volume ratio following the Lever Rule. The common tangent is required for equilibrium when two phases are present so that the chemical potential of A in phase α is equal to the chemical potential of A in phase β so that there is no diffusion of A atoms between α and β while in equilibrium; likewise for B atoms.

Recently, there has been much headway made in the calculation of E using density functional theory. This reduces the many-electron problem down to many one-electron problems. This in combination with linear augmented plane wave, linear muffin-tin orbitals, pseudo-potential method, or linear combination of atomic orbitals allows for solving electronic band structure.

Many advances have been made in the calculation of the total entropy. Calculations of the static components of the entropy are very advanced now.

The simplest model to calculate the configurational entropy in a binary alloy, $A_{1-\chi}B_{\chi}$, assumes a perfectly disordered random solid solution. In other words, each lattice point has a χ probability of being atom B and a $1-\chi$ probability of being atom A. This is the point approximation,

$$S_C^{simple} = -k_{\mathrm{B}}\Big[(1-\chi)\ln(1-\chi) + \chi \ln \chi\Big] \,, \tag{1.2}$$

where k_{B} is the Boltzmann constant. This model breaks down in cases when clustering of atom species occur. When the atom species prefer to have neighbors of the same type, clusters will be present. However, as clustering reduces the configurational entropy, Eq. 1.2 can be used as an upper limit on the configurational entropy in such cases. Modern calculations include this short range order or clustering of atoms with the cluster variation method (CVM).[16, 17, 19, 32, 33]

Calculating vibrational entropy from first principles remains a challenge, especially for disordered systems. There has been much progress in calculation of vibrational entropy, or phonon density of states at low temperatures[46, 57, 62]. However, the temperature dependence of the density of states is not well-predicted. We hope that our work helps to aid the understanding of phonons and anharmonic phonon phenomena, allowing for better future computational predictions of vibrational entropy as a function of temperature.

1.2.2 The Role of Vibrational Entropy

Recently, it has been repeatedly shown experimentally, and accepted by the theoretical community, that the vibrational entropy, ΔS_{vib}, contribution to certain phase transformations can be large.[2, 25, 23, 52, 54, 53, 3, 4, 82, 75, 77] Of course, here we are referring to the

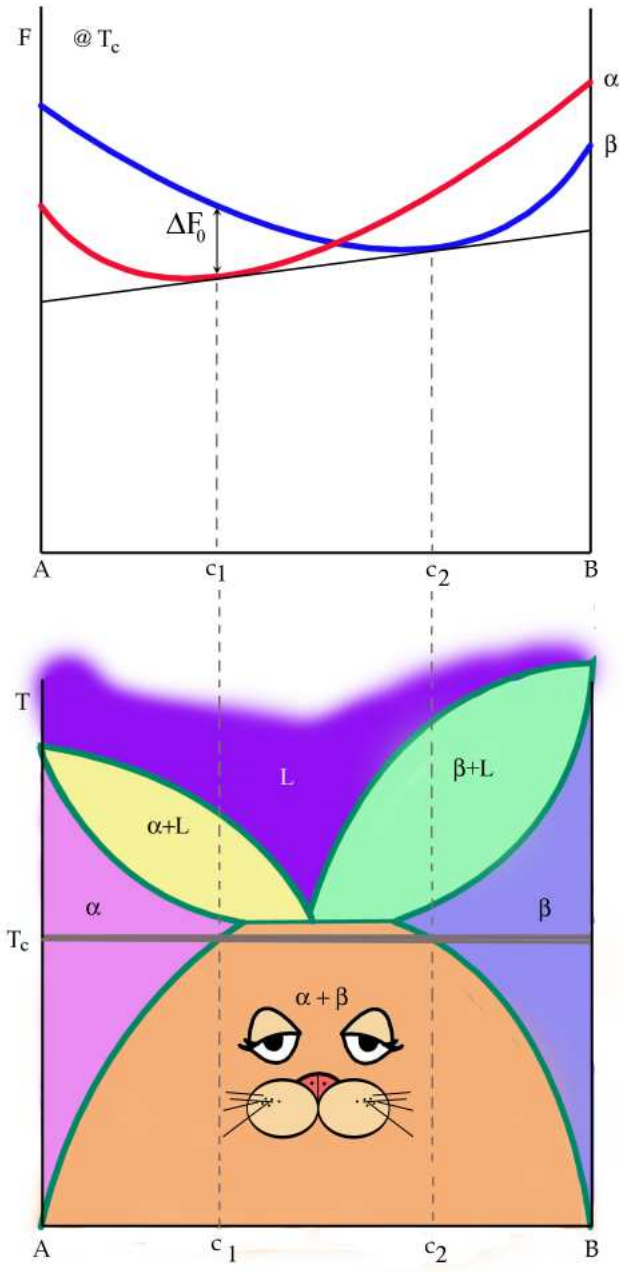

Figure 1.1: Calculation of phase diagrams is done via the free energy.

change in S_{vib} between two phases. It was previously believed that although the magnitude of the S_{vib} is large, the difference between phases would be insignificant. Therefore, previous free energy calculations neglected the S_{vib} contribution to the free energy.

This is in conflict with many systems where the measured change in S_{vib} has been a large contribution to the change in free energy between phases. One can calculate the percent change in the critical temperature for transformation by inclusion of the S_{vib} versus no inclusion of the S_{vib}. First we must assume that the S_{vib} will not change the curvature of F as a function of concentration (i.e., the S_{vib} is not dependent on concentration).[1]

Let's look at the system in Fig. 1.1 for a reference. Consider the critical temperature for phase α at concentration c_1. Define the free energy between phase α and β at which the phase change will occur as ΔF_0. If we only consider the configurational entropy, S_{conf}, the free energy can be written as

$$\Delta F_0 = \Delta E - T_0 \Delta S_{conf} \ , \tag{1.3}$$

where T_0 is the critical temperature when only S_{conf} is considered.

Correspondingly, if we consider both S_{conf} and S_{vib} and call the critical temperature T_c for this case then:

$$\Delta F_0 = \Delta E - T_c(\Delta S_{conf} + \Delta S_{vib}) \ . \tag{1.4}$$

Setting these two equations equal to each other and reducing to the appropriate form gives the percent change in the critical temperature due to the inclusion of S_{vib} as

$$\%\ change = -\frac{\Delta S_{vib}}{\Delta S_{conf} + \Delta S_{vib}} \ . \tag{1.5}$$

We see that the critical temperature is reduced by the ratio of ΔS_{vib} to the total change in entropy. If ΔS_{vib} is equal to ΔS_{conf} then the critical temperature will be reduced by 50%! A very large difference. If the magnitude of ΔS_{vib} is equal to ΔS_{conf}, but their signs are opposite, the phase transformation disappears.

[1] This is obviously not accurate; however, if the dependence on concentration is small, this can be a valid exercise.

Chapter 2

Neutron Scattering

2.1 Introduction

Neutron scattering is a powerful tool for measuring a large variety of material properties such as crystal structure (including short range order), magnetic configuration, diffusion constants, crystal field splitting, phonons, and spin waves.

Neutrons have no charge and therefore do not interact easily with materials. Thus, they measure bulk properties due to their deep penetration of materials. Neutrons are also massive, unlike x-rays or electrons. This is an extremely useful property, allowing for the energy of neutrons to be near that of inelastic processes in the material while still having wavelengths similar to the lattice constant.

2.2 Spallation Neutron Sources

The majority of phonon measurements in this work were done at spallation neutron sources. Spallation sources are very efficient for measurements over a large portion of phase space.

A typical spallation neutron source, see Fig. 2.1, begins with front-end systems that comprise an ion source and preaccelerator that create a pulsed, accelerated H^- beam. The values of energy, pulse frequency, and current range between 750 keV–2.5 MeV, 30 Hz–60 Hz, and 26 mA–30 mA depending on the facility design. New facilities are pushing the limits of design every time they are built. Next the H^- are accelerated to 50 MeV - 1 GeV in a linear accelerator (linac). The pulses are also focused and directed by the superconducting

magnets of the linac while they are accelerated.

At the end of the linac, the H^- are stripped of their electrons as the pulse enters an accumulator ring. The purpose of the accumulator ring is to squeeze the pulse in time so that it is a shorter more intense pulse. The final pulse is approximately 10^{-6} sec in length. The final average current delivered to the target is 14 μA to 1.4 mA. The final step is the spallation of neutrons at the heavy metal target. The target is heavy metal so that there are plenty of neutrons available to be "spalled," or knocked out, in a series of nuclear reactions that expel 20 to 30 neutrons for every incident proton that reacts with multiple nuclei. The neutrons come out of the target with large energies and in all directions.

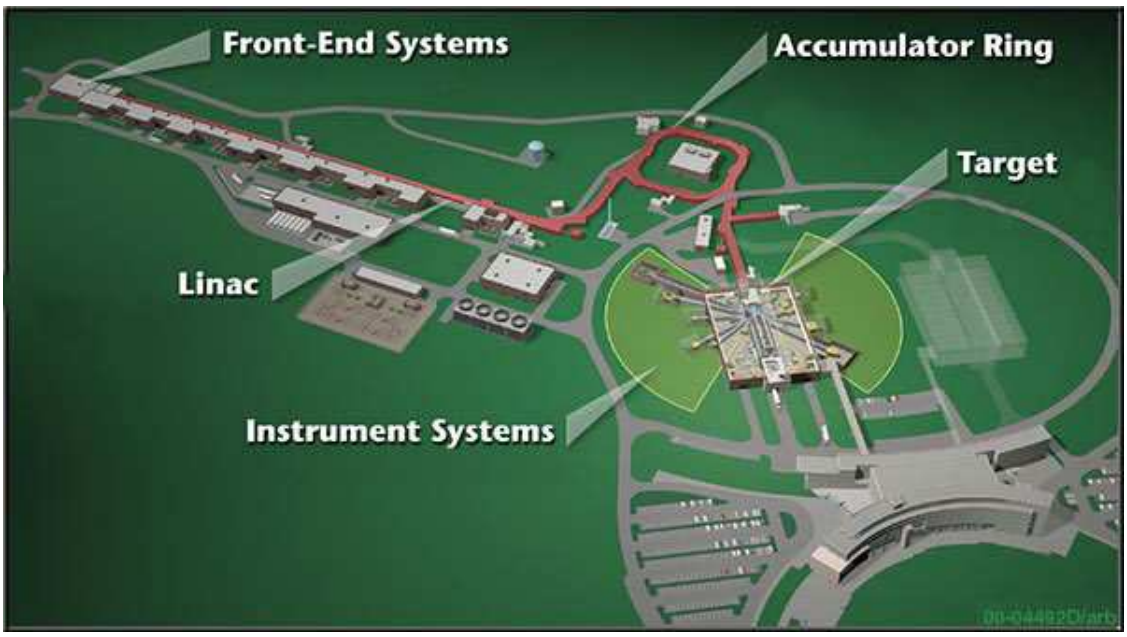

Figure 2.1: Typical layout of a spallation neutron facility. This particular schematic is of the SNS currently being built at Oakridge National Laboratory, due for completion in 2006.

2.3 Direct Geometry Chopper Spectrometer

Inelastic neutron scattering measurements were performed on direct geometry chopper spectrometers, Fig. 2.2. First, the neutrons need to be slowed in order to obtain wavelengths necessary to excite phonons. The neutrons are "thermalized" from energies of MeV to tens

of meV. This occurs by scattering in a *moderator*, often water. The neutrons reach a kind of equilibrium with the material of the moderator, attaining energies useful for phonon scattering. Moderators often use materials with large quantities of hydrogen because hydrogen is a very large neutron scatterer, thus giving the neutrons opportunity to experience the necessary energy loss into the moderator through multiple inelastic collisions. The neutron pulse leaving the moderator is a Maxwellian flux distribution (see Fig. 2.3). the energy peak of this distribution can be modified depending on the type of moderator used.

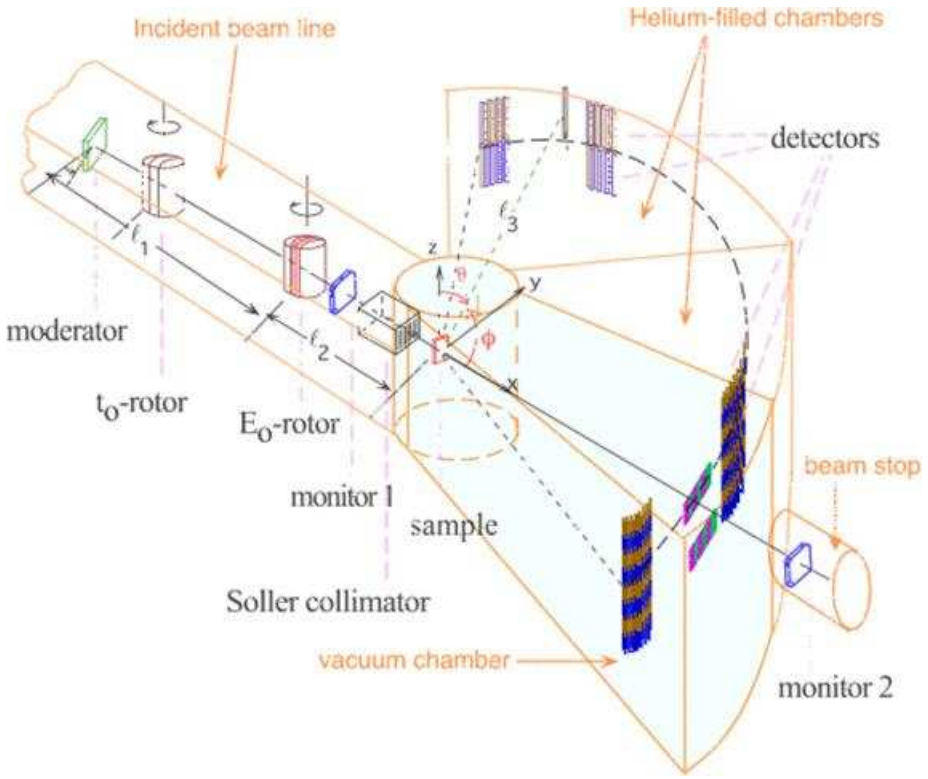

Figure 2.2: Typical layout of a direct geometery chopper spectrometer. This particular schematic is of the High Resolution Medium Energy Chopper Spectrometer (HRMECS) at Argonne National Laboratory.

The inelastic measurement requires a monochromatic incident beam. Let us assume a desired incident energy of $E = E_0$. To achieve this, the instruments utilize choppers (noted as rotors in Fig. 2.2). Each instrument typically uses two choppers. The neutrons first encounter a t_0 chopper; the second is the E_0 chopper (or Fermi chopper). The choppers act

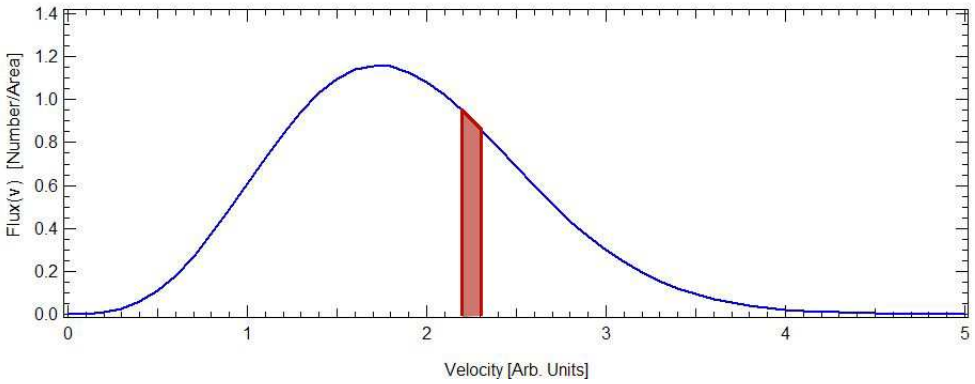

Figure 2.3: The Maxwellian distribution exiting the moderator is shown in blue. The portion of these neutrons passed by the Fermi chopper is shown in red.

like windows in time; they are open when the neutrons with the desired energy are at the position of the chopper, and closed at the times when neutrons with the wrong energies are at the chopper. Thus they "chop" the neutron pulse into a smaller segment in time. The t_0 is employed to pass the neutrons with energy ranging around $E_0 \pm E'$ and remove any high energy neutrons from a later pulse that could be phased just right to get through the E_0 chopper. The t_0 chopper also blocks the initial gamma flash and burst of unmoderated MeV fast neutrons that happens when the proton pulse hits the target. The E_0 chopper refines the energies that reach it through the t_0 chopper to a much smaller range of energies, $E_0 \pm \epsilon$, where $\epsilon \ll E'$. The shaded region in Figure 2.3 shows the neutrons that are passed through the open E_0 chopper.

Figure 2.4 gives a graphical explanation of how the t_0 and E_0 choppers work together to ensure a neutron pulse that is reasonably monochromatic. The lines radiating from p_1 are neutrons that are part of the first pulse. Their velocities are equal to the slope of the line. Three energies are shown for p_1. The desired energy, E_0, is the middle line. The horizontal lines labeled t_0 and E_0 indicate the position of the corresponding chopper. They have no slope because they are not moving in distance as a function of time. When the chopper is open the line disappears allowing neutrons to pass; conversely the horizontal line does not allow neutrons that hit it to pass, thus indicating that the chopper window is closed. First consider p_1 alone: The t_0 chopper allows many energies through but the E_0 chopper only allows energies very close to E_0 through. Now consider what happens upon the second

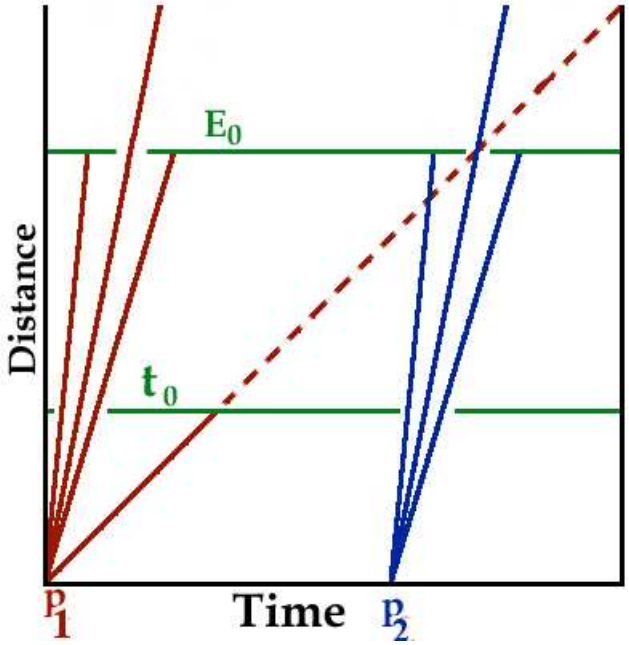

Figure 2.4: t_0 and E_0 chopper timing

pulse, p_2. Everything is the same for the second pulse as it was with the first save one thing, the t_0 chopper stops a low energy neutron, which the dashed line shows would have been let through the E_0 chopper. If this low energy neutron had not been stopped by the t_0 chopper it would have corrupted the data.

Energy resolution and neutron flux are inversely related in this type of instrument. The longer the E_0 chopper window is open, the more neutron flux on the sample, and the larger the range of incident energy on the sample which corresponds to a lower energy resolution. In other words, to have better energy resolution the width of the red region in Fig. 2.3 will decrease; however that will also reduce the area under the curve of the red region, which is the total flux on the sample. Another way to view the energy resolution of the spectrometer that is from the E_0 chopper is seen in Figure 2.5. The solid line indicates the desired incident energy. The longer the chopper is open the more neutron energies will be able to pass, contributing to the energy resolution of the instrument.

The monitors measure the incident neutron flux, which is used in the normalization of data sets. Many instruments utilize the advancing collimation technologies. LRMECS has

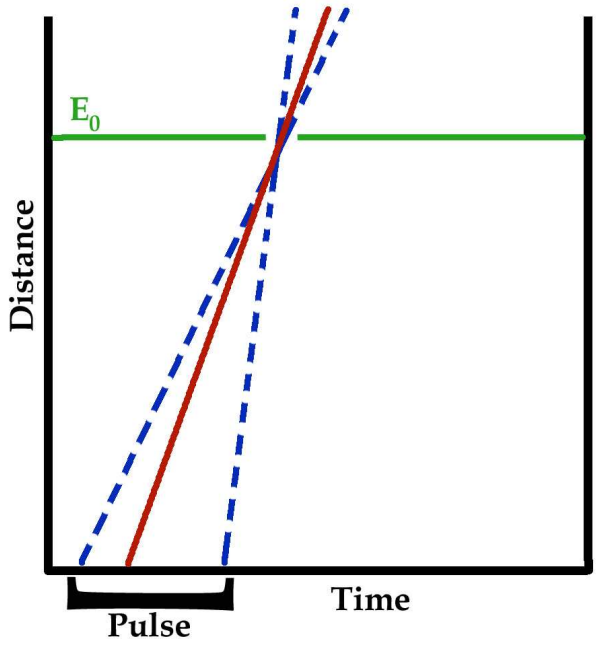

Figure 2.5: An alternate view of the range in energies that pass through the open Fermi-Chopper. The longer the the chopper is open, the more energies pass.

a Soller collimator to reduce angular spread of the neutrons after leaving the Fermi chopper. Collimators absorb neutrons that are divergent. Also available are neutron guides, which are made of neutron-reflective materials that will increase the neutron flux on the sample however divergence remains.

The neutrons scatter inelastically with the sample exciting available states within the sample. In this work we will assume all the energy change in the neutron goes into the creation or annihilation of phonons. Neutrons can excite spin waves; however, magnetic scattering is most prominent at low scattering angle, and these data can be neglected in the subsequent analysis.

The loss or gain of the energy of each neutron is determined from its change in velocity. The incident energy is monochromatic with known incident velocity. For the fixed distance in the instrument, the time at which the neutron scatters from the sample is known. This, along with the time the neutron reaches the detector, gives the velocity of the scattered neutron. Thus it is a simple calculation to find the energy loss or gain of the neutron.

This time-of-flight design means that the sample is assumed to be at one point in space, the radius point for the detector array. Real samples have dimension; neutrons scattered from the edge of the sample have a different path length from the scattering point to the detector. If the scattering event is elastic and is closer to the detector than the radius point, the calculated energy of the scattering event will look inelastic. It will look as though the neutron gained energy upon scattering. This will contribute to the energy resolution of the experiment. For example, cylindrical geometry samples will have a double elastic peak surrounding the zero energy point.

2.4 Coherent and Incoherent Scattering

First consider the interference of two waves: $\Psi_1 = A_1 \exp[i(-\omega t) + \phi_1]$ and $\Psi_2 = A_2 \exp[i(-\omega t + \phi_2)]$. The intensity of the superposition of the two waves is

$$I = |\Psi_1 + \Psi_2|^2 = |\Psi_1|^2 + |\Psi_2|^2 + \Psi_1^* \cdot \Psi_2 + \Psi_1 \cdot \Psi_2^* \, . \tag{2.1}$$

$$I = A_1^2 + A_2^2 + 2A_1 A_2 cos\Delta\phi \, . \tag{2.2}$$

Let's generalize the above to a superposition of N waves with the same frequency. The superposition of all the waves is

$$\Psi = \sum_{r=1}^{N} \Psi_r \, . \tag{2.3}$$

The total wave will oscillate with frequency, ω, and with an amplitude that is the result of the phasor sum of each of the individual waves. If all the component waves are inphase then the amplitude is maximized. The minimum will be zero unless one component amplitude is so large that the component amplitudes cannot cancel it.

The phasor for the wave is

$$\Psi_r = A_0 e^{-i(\omega t - \phi_r)} \, . \tag{2.4}$$

Therefore the intensity will be

$$I = |A_0|^2 \Big| \sum_{r=1}^{N} e^{i\phi_r} \Big|^2 . \tag{2.5}$$

The exponential can be expanded as

$$\Big| \sum_{r=1}^{N} e^{i\phi_r} \Big|^2 = \Big(\sum_r cos\phi_r \Big)^2 + \Big(\sum_r sin\phi_r \Big)^2 \tag{2.6}$$

$$\Big| \sum_{r=1}^{N} e^{i\phi_r} \Big|^2 = \sum_r cos^2\phi_r + \sum_{r\neq s} \sum_{s\neq r} cos\phi_r cos\phi_s + \sum_r sin^2\phi_r + \sum_{r\neq s} \sum_{s\neq r} sin\phi_r sin\phi_s . \tag{2.7}$$

If all the phases are the same, then we have coherent constructive interference and the intensity of the superposition is $N^2A_0^2$. If the phases are, however, uncorrelated, then they are incoherent. If N is also large then the terms with double summations in Eq. 2.7 will average out to zero as they will have equal amounts of positive and negative contributions. This will leave

$$\sum_r (cos^2\phi_r + sin^2\phi_r) = \sum_r^N 1 = N , \tag{2.8}$$

giving the intensity of incoherent superposition of waves to be NA_0^2. We see now that the intensity of of the superposition of incoherent waves is

$$I = \Sigma_N |\Psi_N|^2 , \tag{2.9}$$

where the intensity of the superposition of two coherent waves is

$$I = |\Sigma_N \Psi_N|^2 . \tag{2.10}$$

All waves interfere; it is the nature of a wave to interfere with other waves. However, when many waves are interfering it is helpful to consider whether their phase relationships are fixed or varying. Coherent scattering produces very different results than incoherent scattering. A coherently scattered wave has a distinct phase relationship with the incident wave. This being the case, the interference of the waves will be magnified by all the other coherently scattered neutrons. The interference of coherently scattered neutrons gives rise to variation in intensity with scattering angle. In contrast, waves scattered incoherently

do not maintain a distinct phase relationship with the incident wave after scattering. The phase relationship varies randomly for each scattering event. Therefore, the interference of each pair of scattered incoherent waves will be "washed out" once averaged over all phase relationships. Incoherently scattered neutrons do not have sharp intensity variations with angle. They can vary with angle; indeed, phonon scattering increases as a function of the square of the phonon moment.

2.5 Multiphonon Scattering

The simplest type of inelastic scattering is when one neutron scatters off the sample creating or annihilating one phonon, seen on the left hand side of Fig. 2.6. However, also possible is an N-phonon process which is any scattering that involves a total of N phonons. Also shown in Fig. 2.6 are all the possible two-phonon processes. These processes are detailed in Chapter 3.

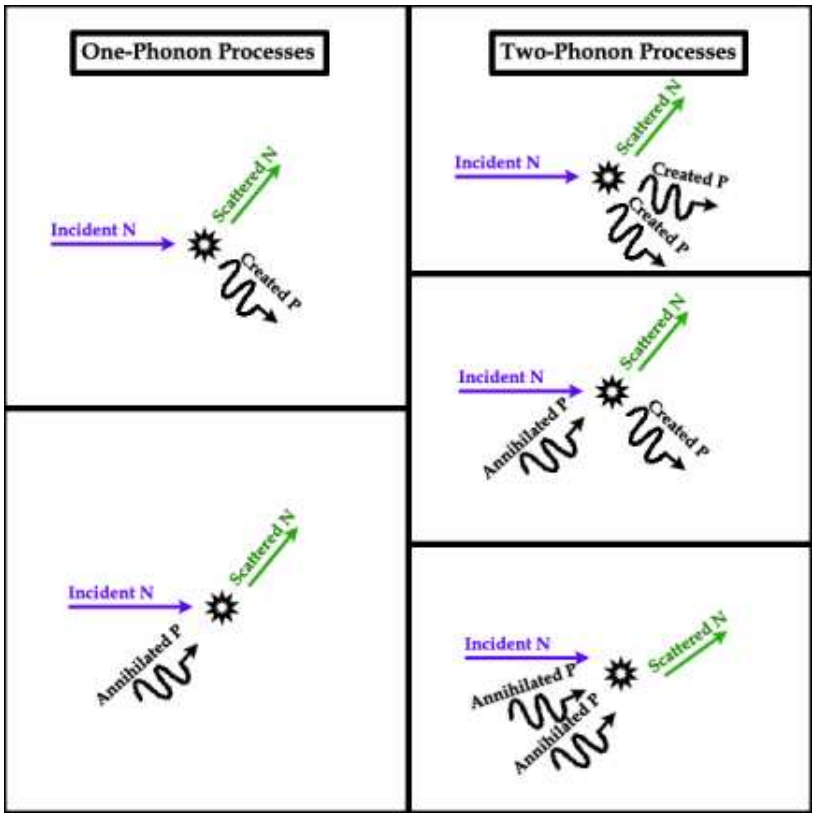

Figure 2.6: Phonon Scattering Processes

Chapter 3

Data Analysis

3.1 Raw Neutron Scattering to Vibrational Density of States

3.1.1 Incoherent Approximation

The incoherent approximation [67, 56] is an essential step to the multiphonon correction. Within the incoherent approximation we are able to assume that the coherent scattering summed over all angles approximates the incoherent scattering up to a scaling factor. The idea is that the variations in coherent scattering will average, once summed over all angles, to be similar to the incoherent scattering. This approximation is particularly well-suited to poly-crystalline samples since they access more angles than the detector array.

3.1.2 The One-Phonon Scattering Function

Raw data from the chopper spectrometer are in the form of counts vs. angle and time-of-flight. This raw data includes artifacts of each detector's efficiency (or sensitivity). Individual detectors have different efficiencies that vary over the lifetime of the detector. A correction for this variation in efficiency is performed by utilizing a vanadium spectrum. Vanadium is used because for all practical purposes V scatters completely incoherently; the cross-sections for V are σ_{inc}=5.08 barns and σ_{coh}=0.02 barns. Therefore, the scattering intensity varies smoothly as a function of angle, so any sharp variations in the counts between detectors is due to detector efficiency variations. Thus, V data give correction factors for detector counts, allowing a normalization of the detector array.

Data also need to be normalized by the total number of monitor counts (i.e., the total number of incident neutrons). For example, if we are going to compare samples A and B, and sample A was measured twice as long as sample B, then the data need to be normalized in such a way as to keep sample A from having two times the intensity necessary for the comparison. Therefore, sample A should be divided by two, otherwise it will have twice the scattered intensity. This correction is performed by dividing by the monitor counts for all data sets (monitor 1 can be seen in Fig. 2.2).

The data are then converted or re-binned into angular bins that are approximately 10° per bin. The time-of-flight axis is also re-binned into energy bins of approximately 0.5 meV. The energy axis represents energy transferred from the neutron into the sample and is taken to be the energy of the phonon created (> 0) or annihilated (< 0).

Next we subtract the "time-dependent background." This is the empty can data. It is usually best to subtract $(1 - a)$ times the empty can spectra if your sample is a $(a \times 100)\%$ scatterer. This is often best left to the eye for judgement; by overlaying the background spectra on the data and playing with a multiplication factor so that the high energy background is mostly removed you may find that you get a better result. (Note: This is only valid for room temperature and lower measurements where multiphonon scattering is small.) Typically the factor is between 0.9 and 1.[1] Let's call the data up to this point "raw-data*". The data at this point can be seen in Fig. 3.1, and an enlargement of the inelastic scattering can be seen in Fig. 3.2.

Once the above corrections have been performed on the raw-data* the data are:

$$\left(\frac{\partial^2\sigma}{\partial\Omega\partial E'}\right)_{total} = \sum_N \left[\left(\frac{\partial^2\sigma}{\partial\Omega\partial E'}\right)_{coh\pm N} + \left(\frac{\partial^2\sigma}{\partial\Omega\partial E'}\right)_{inc\pm N}\right], \tag{3.1}$$

the sum of both the coherent and incoherent scattering for all N-phonon processes. However, within the incoherent approximation after summing over all angles for a poly-crystalline sample it is assumed that all scattering is incoherent:

[1] One can use data from a cadmium absorber run in combination with the empty can to account more accurately for the time-dependent background. However I have not found that this is necessary as the error is minimal.

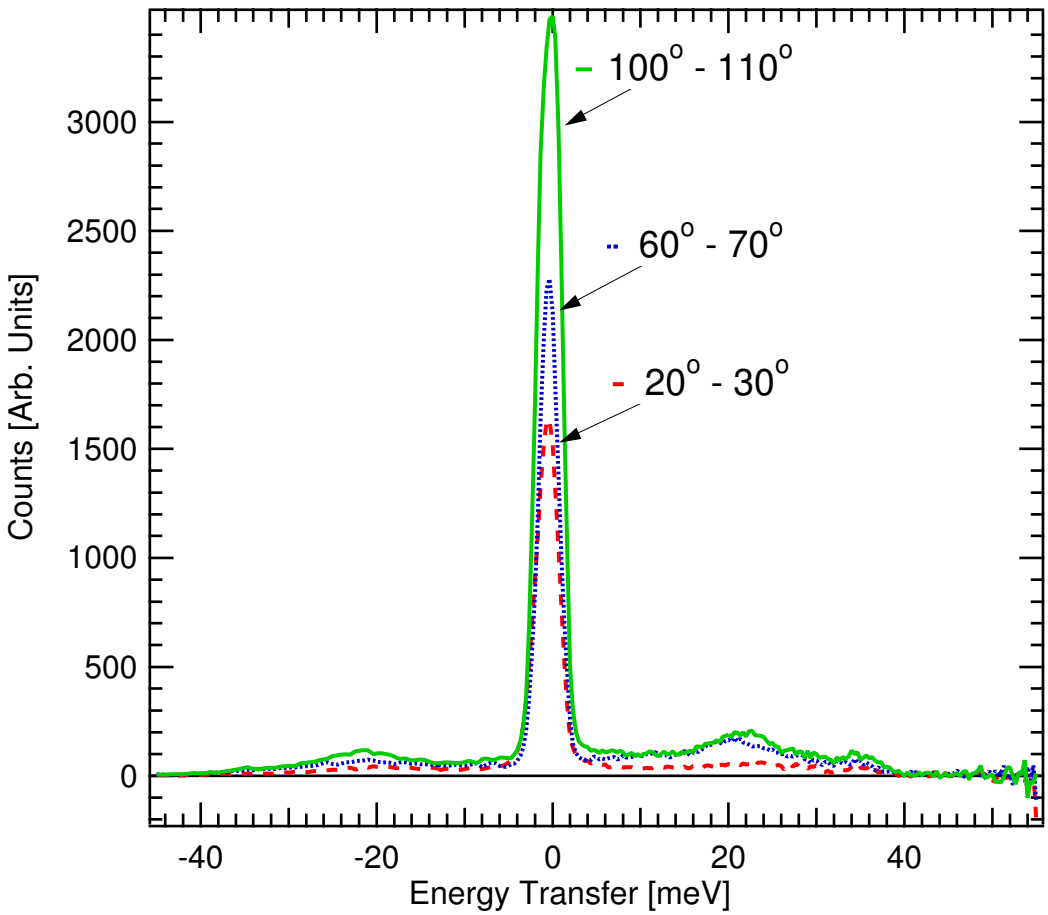

Figure 3.1: Raw neutron scattering data (raw-data*) for angle bins 20 °–30 °, 60 °–70 °, and 100 °–110 °.

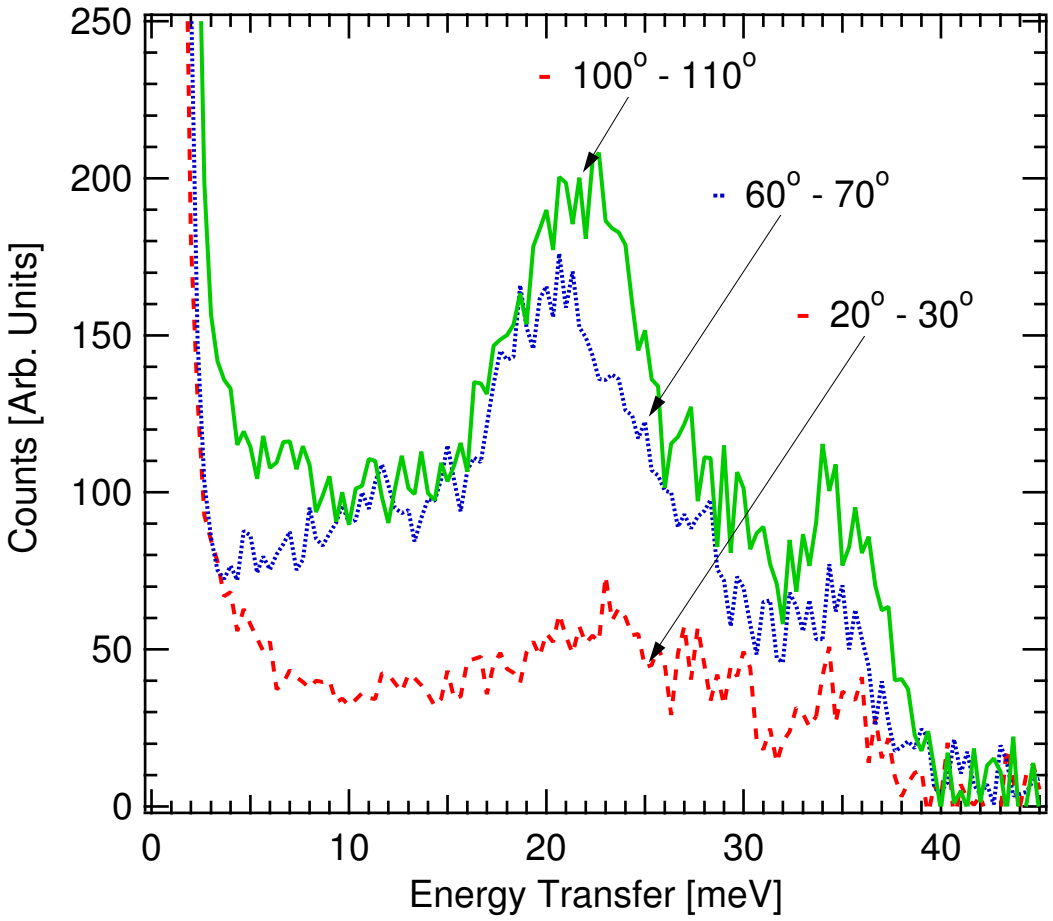

Figure 3.2: Raw inelastic neutron scattering data (raw-data*) for angle bins 20 °–30 °, 60 °–70 °, and 100 °–110 °.

$$\left(\frac{\partial\sigma}{\partial E'}\right)_{total} = \sum_N a\left(\frac{\partial\sigma}{\partial E'}\right)_{inc\pm N}, \tag{3.2}$$

where a is a constant coefficient.

Conveniently, the one-phonon scattering can be related to the vibrational density of states (DOS), which is what we are after! [67]

$$\left(\frac{\partial^2\sigma}{\partial\Omega\partial E'}\right)_{inc\pm1} = \frac{\sigma_{inc}}{4\pi}\frac{k'}{k}\frac{N}{4M}\kappa^2\exp(-2W)\frac{g(\omega)}{\omega}\left\{\coth\left(\frac{\hbar\omega}{2k_BT}\right)\pm1\right\}, \tag{3.3}$$

where σ is the the incoherent cross-section of the scattering atom, and k and k' are the initial and final wavevectors, respectively, of the scattered neutron. The change in wavevector of the scattered neutron, $\kappa = |\vec{\kappa}| = |\vec{k}-\vec{k'}|$, is taken to be the average value of κ for each angular bin; 2W is the Debye-Waller factor; and $g(\omega)$ is the vibrational density of states. Notice that the inelastic scattering intensity is proportional to κ^2 (i.e., increases with scattering angle). In Fig. 3.2 you can see the phonon scattering intensity increases as κ^2 in Eq. 3.3. From Eq. 3.3, it follows that if we can isolate the incoherent 1-phonon scattering from our data then it is just a matter of scaling factors to get the DOS. To be left with only the 1-phonon scattering data, the 0-phonon (or elastic) scattering and the multiphonon scattering involving a total of 2 or more phonons (or 2-∞ phonon scattering) must be removed from the our data.

First consider the 0-phonon or elastic scattering correction. The elastic scattering must be removed. This can be a very daunting task. However, the other factors in the double differential cross-section approach zero with such strength that it tends to wash out the elastic peak. This allows for some error in the elastic peak correction. After trying many different methods including fitting the elastic peak to a Voigt function, Peter Bogdanoff[4] found that a simple horizontal cut of the elastic peak at the point where inelastic scattering is obviously present was the easiest method. It has proven to be quite reliable and is appropriate theoretically within the continuum limit.[4, 6] The "Corrected Data" in Fig. 3.3 has had the elastic peak removed.

Removal of the 2-∞ phonon scattering is not as easy to accomplish. We are at least able to assume the 6-∞ phonon scattering is negligible, requiring only the 2-5 phonon

scattering to be taken into account. If this were not true, we would be in the classical limit and identification of the phonon spectrum would be impossible. Fig. 3.3 also shows the calculated 2-5 multiphonon scattering, the "Corrected Data" are the data after the elastic and the multiphonon correction. The next section covers the multiphonon scattering calculation in detail. So assuming we can calculate the 2-5 phonon scattering as described below; we can extract the DOS by an iterative process that converges on the Debye-Waller factor, see Fig. 3.4 for a reference.

For the first iteration, we calculate an initial rough DOS by assuming the raw data is completely incoherent one-phonon scattering. We do this by dividing out the extra factors in Eq. 3.3 for each angular bank. We then utilize the incoherent approximation by summing over all angular bins (see Sect. 3.1.1) leaving only the rough DOS, $g'(\omega)$. In this first iteration we guess a value for the average mean-square displacement of the atoms for the Debye-Waller factor. For a room temperature measurement, $< u^2 >= 0.02\text{Å}^2$ is a good start. This rough DOS, $g'(\omega)$, is then used to calculate the 2-5 multiphonon scattering (described in Sect. 3.1.3). The 1-5 multiphonon scattering is fit to the raw-data* (see Fig. 3.3) to obtain the scaling factor for the 1-5 phonon scattering. The rough DOS is also used to calculate the Debye-Waller factor for the next iteration. Now that the multiphonon contribution is calculated. We start with the raw-data*, subtract the elastic peak and the multiphonon scattering from it, which gives us a better estimate of the incoherent one-phonon double differential cross-section from which we can calculate a new estimate of the DOS using the mean-square displacement measured from the last DOS. Now we iterate this process until we converge on the average mean-square displacement or essentially the Debye-Waller factor. [5]

3.1.3 Multiphonon Scattering Correction

Sect. 2.5 has shown that the scattering of neutrons can excite and annihilate phonons with infinite possible combinations. Multiphonon scattering processes occur when two or more phonons are involved in a single scattering of a neutron. All multiphonon scattering must be removed from the data to achieve scattering involving only one phonon. This is an essential step in the previous section. This section explains the process that starts with

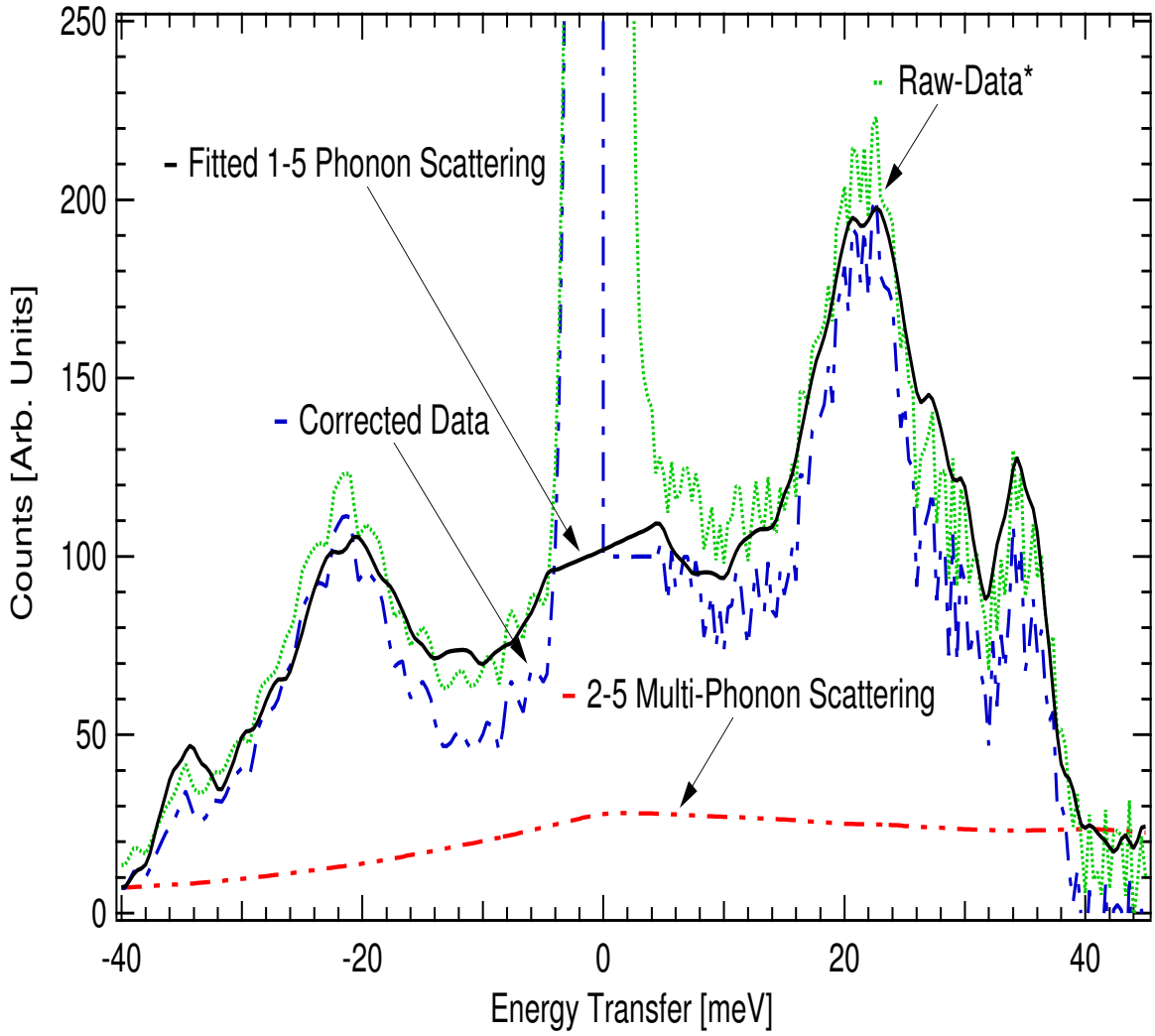

Figure 3.3: Data at various stages throughout the DOS reduction process.

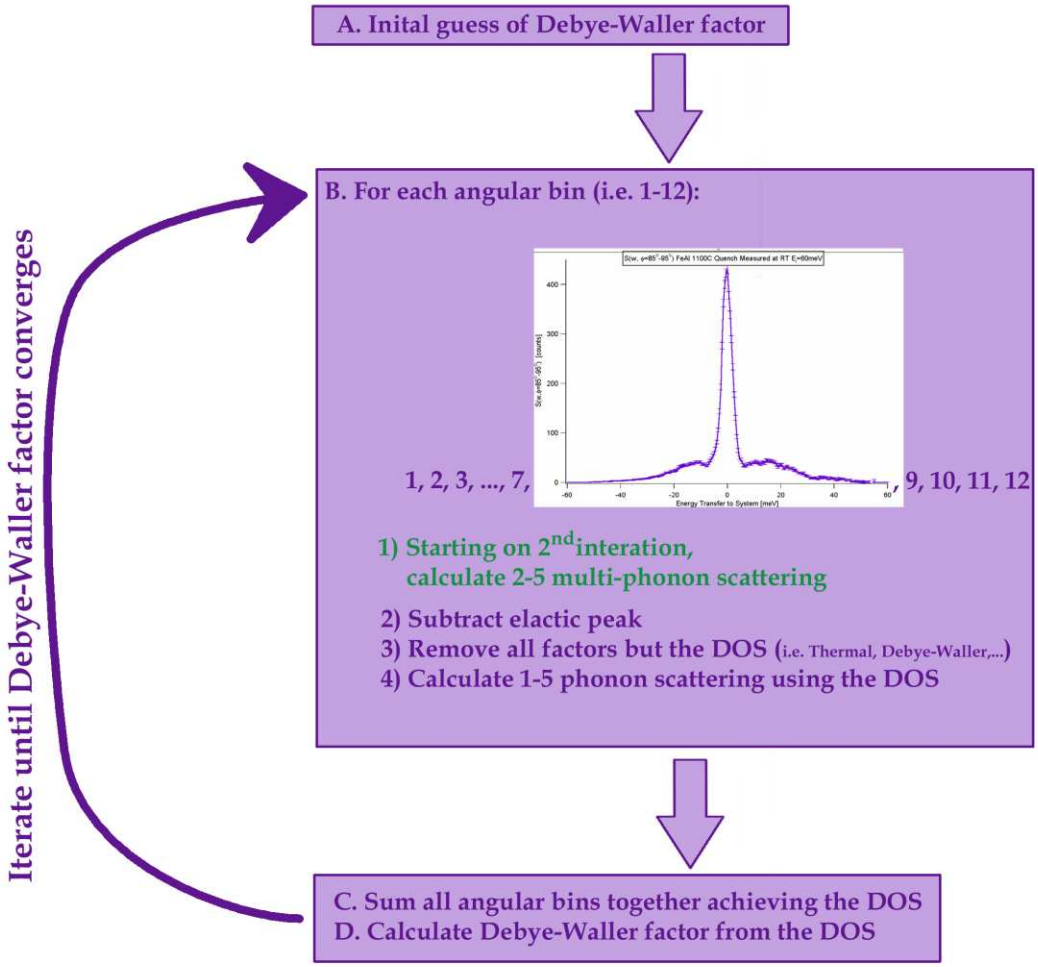

Figure 3.4: Iterative data reduction, described in the text to extract the DOS.

the first estimate of the DOS, and proceeds to generate the intensity from a 2-phonon through 5-phonon multiphonon scattering. [5] The calculated multiphonon scattering is then subtracted from the raw data to isolate the 1-phonon scattering, from which a better DOS is created, using the procedure described in Sect. 3.1.2.

All scattering is assumed to be incoherent in the multiphonon correction. Inclusion of the coherent scattering has not yet been attempted, as this would require an in depth simulation of lattice dynamics to obtain the $\vec{\kappa}$ dependence of the scattering. However the incoherent approximation has proven to be reliable for powder samples even when there is large coherent scattering from the sample. This is because the powder averages over all $\vec{\kappa}$ covering a large portion of reciprocal space.

The double-differential cross-section can be written for incoherent scattering in the form

$$\left(\frac{\partial^2\sigma}{\partial\Omega\partial E'}\right)_{inc\pm N} = \frac{\sigma_{inc}}{4\pi\hbar}\frac{k'}{k}\frac{N}{n!}e^{-2W}\left(\frac{3\hbar}{2m}\right)^n\Big[P(\omega)\Big]^{n-convolution} , \tag{3.4}$$

where

$$P(\omega) = \frac{\langle(\vec{\kappa}\cdot\vec{e}_s)^2\rangle_\omega}{\omega}g(\hbar\omega)\langle n_\omega+1\rangle + \frac{\langle(\vec{\kappa}\cdot\vec{e}_s)^2\rangle_{-\omega}}{-\omega}g(-\hbar\omega)\langle n_{-\omega}+1\rangle , \tag{3.5}$$

and n_ω is the Bose-Einstein distribution. The convolutions are calculated as

$$[P(\omega)]^{1-convolution} = P(\omega) , \tag{3.6}$$

$$[P(\omega)]^{2-convolution} = \int_{-\infty}^{\infty} P(x)P(\omega-x)dx . \tag{3.7}$$

To achieve the 3-phonon convolution one can convolve the 1-phonon with the 2-phonon; computationally this turns out to be the easiest as the 1- and 2-phonon convolutions are already stored in memory.

3.1.4 Partial Density of States

Each atomic species, d, of concentration χ_d in an alloy has a partial density of states (PDOS), g_d^χ, which combine linearly to create the DOS:

$$g(E) = \sum_d \chi_d g_d^\chi(E). \tag{3.8}$$

3.1.5 Introduction to Neutron-Weighting and Various Corrections

"Neutron-weighting" is a term used to describe the distortion of the DOS that is caused by the varying efficiency of different isotopes in scattering neutrons. Therefore, what is measured by inelastic neutron scattering is the "neutron-weighted density of states" (NWDOS), which is a weighted linear combination of the PDOS:

$$g^{\mathrm{nw}}(E) \propto \exp(2W) \sum_d g_d^\chi(E) \exp(-2W_d) \frac{\sigma_d}{M_d} \,, \tag{3.9}$$

where $\exp(-2W_d)$ is the Debye-Waller factor, σ_d is the total scattering cross section, and M_d is the molar mass of atom d. The factor $\exp(2W)$ is the average Debye-Waller correction calculated from the self-consistent neutron-weighted DOS. We can consider $\exp[-2(W - W_d)] = 1$, an assumption that is most reliable at low temperatures. Thus,

$$g^{\mathrm{nw}}(E) = A \sum_d g_d^\chi(E) \frac{\sigma_d}{M_d} x_d \,, \tag{3.10}$$

where the normalization factor, A, depends on concentrations of the elements and their scattering strengths,

$$A = \left(\sum_d \frac{\sigma_d}{M_d} \chi_d \right)^{-1} . \tag{3.11}$$

One can see the neutron-weighting factor, σ_d/M_d, quite clearly when comparing Eq. 3.10 to Eq. 3.8. If σ_d/M_d for all atomic species were equal, Eq. 3.10 would equal Eq. 3.8.

Many methods of correcting for this scattering efficiency difference have been developed for alloys. The most straightforward is to measure multiple samples under the same measuring conditions with appropriately weighted isotopic distributions so as to remove all scatter from all but one element. Although this method is very reliable, it can be prohibitively

expensive.

3.2 Quasi-Harmonic Vibrational Entropy

By measuring the DOS it is possible to calculate the vibrational entropy using the quasi-harmonic approximation. This measurement includes the vibrational entropy due to the thermal expansion of the lattice and is given as

$$S_{\mathrm{vib}}(T_m, T_p) = 3\, k_{\mathrm{B}} \int_0^\infty g(E, T_m) \left[(n_E(T_p) + 1) \ln(n_E(T_p) + 1) - n_E(T_p) \ln(n_E(T_p)) \right] \mathrm{d}E \,, \tag{3.12}$$

where $g(E, T_m)$ is the DOS measured at T_m, and $n_E(T_p)$ is the Bose-Einstein factor populated at the temperature T_p. Notice that the DOS is weighted by a thermal factor in square brackets. This factor lays more weight to the low energy modes than to the high energy modes. This is displayed in Fig. 3.5. The final integrand clearly has higher contributions at lower energies.

One way to think of this is to consider classical harmonic oscillators. If two simple harmonic oscillators are at the same temperature and are identical except for different spring constants, k, which will have more vibrational entropy?

The thermal energy available to the harmonic oscillators will be E, thus the maximum energy attained by that oscillator will be

$$E = \frac{kx^2}{2} + \frac{p^2}{2m} \,, \tag{3.13}$$

where k is the spring constant, p is the momentum, m is the mass on the end of the spring, and x is the position of the mass. The number of states explored by the system is related to the phase-space explored by the system. The phase-space can be seen by plotting p vs. x, Fig. 3.6. Recall from geometry the equation of an ellipse is

$$1 = \frac{x^2}{\alpha^2} + \frac{p^2}{\beta^2} \,, \tag{3.14}$$

therefore the area of phase-space accessible to the system is elliptical. If we put Eq. 3.13 in

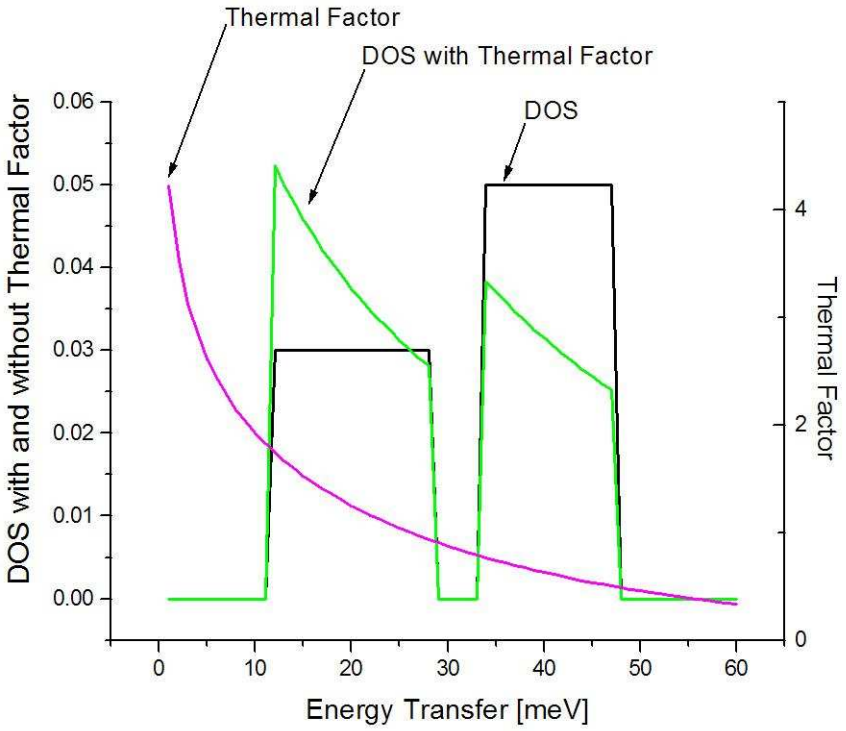

Figure 3.5: When the DOS is weighted by the thermal factor, the low energy vibrational modes have a larger contribution to the quasi-harmonic entropy than the high energy modes.

this form we get

$$1 = \frac{kx^2}{2E} + \frac{p^2}{2mE} \,, \tag{3.15}$$

showing that

$$\alpha = \sqrt{\frac{2E}{k}}, \beta = \sqrt{2mE} \,. \tag{3.16}$$

If the two oscillators have spring constants k_1 and k_2, where $k_2 < k_1$, then which oscillator has more entropy? Notice that a decrease in k corresponds to an increase in α, since β stays the same, and the area of the ellipse ($\pi\alpha\beta$) or the phase-space increases. That means that the number of states explored by the spring, Ω, increases because Ω is proportional to the area of the ellipse. Therefore, because

$$S = k_B ln\Omega \,, \tag{3.17}$$

the entropy increases as k decreases. So the softer the spring constant, the more entropy of the oscillator. Thus, the spring with k_2 will have more entropy than the spring with k_1. For a harmonic oscillator, $k = m\omega^2$, where omega is the frequency of vibration. The energy of vibration is $\hbar\omega$, so if the energy of the vibration decreases then ω decreases and k decreases. We already showed that a decrease in k is an increase in entropy. So a decrease in vibrational energy is an increase in entropy. This is one way to understand why low energy modes contribute more entropy to the system.

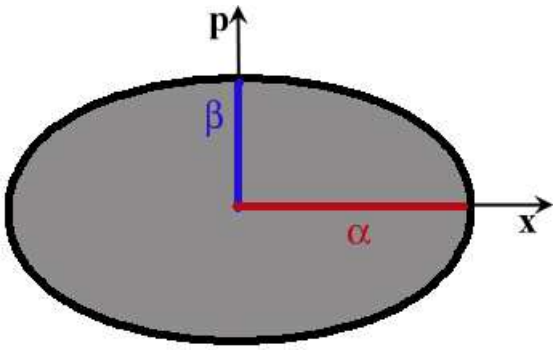

Figure 3.6: Effect of the energy of vibration on the entropy of vibration.

3.3 Anharmonic Vibrational Entropy

3.3.1 Measurement of the Anharmonic Vibrational Entropy

The most obvious model for lattice vibrations is the Born von Kármán model. This assumes that the crystal is made of masses (atoms), which are connected to each other by springs (atomic forces). This model is essentially an immense system of coupled harmonic oscillators. Of course, no atomic potential is purely harmonic, but for low temperatures the harmonic potential well is a reasonable first-order approximation.

Unfortunately, at higher temperatures the harmonic model begins to break down as the atoms begin to access higher energy states. It is not necessarily so obvious how one would measure the anharmonic vibrational entropy. How do you separate the harmonic from the anharmonic within the total vibrational entropy for high temperature data?

It is best to first define what the anharmonic vibrational entropy is. Theoretically the anharmonic vibrational entropy would be the entropy associated with changes in the DOS due to a non-harmonic atomic potential well. The total vibrational entropy will be the sum of the anharmonic and the harmonic contributions. For some familiarity with these two contributions, let's briefly explore some of the differences between harmonic and anharmonic potentials and crystals.

The perfect harmonic crystal does not experience lattice expansion as the temperature increases. Lattice expansion is caused by the break in symmetry of the atomic potential energy wells of the atoms in the crystal. In a harmonic well the average atomic position remains constant at all energies. Also the DOS of a perfect harmonic crystal is not temperature-dependent. In the anharmonic well the average position shifts with energy.

We can now write down a method for extracting the anharmonic vibrational entropy from our data. To measure the anharmonic entropy we must have two DOS curves from the same phase at different temperatures, T_1 and T_2. T_1 should be a low temperature; room temperature is really the upper limit for this if one is trying to get the purely harmonic contribution. T_2 can be any temperature at which anharmonic effects might be large enough to notice. What we want to do is measure the difference between what the harmonic sample would be at high temperatures and what the in-situ sample was at high temperatures. In

general, using Eq. 3.12,

$$S^{\text{Anh}} = S^{Tot}(T_2, T_2) - S^{Harm}(T_1, T_2) \ , \tag{3.18}$$

where we are populating the harmonic DOS at the high temperature to get the harmonic vibrational entropy at $T = T_2$.

3.3.2 Contributions to the Anharmonic Vibrational Entropy

Contributions to the anharmonic vibrational entropy include lattice expansion, phonons coupling with themselves, or other phenomena (such as electrons or magnons). It can be very difficult to figure out which of these are contributing and how much they contribute. There is a great deal to learn in this field of lattice dynamics.

One of these contributions is well-understood, lattice expansion. Lattice expansion will "soften" the DOS–as the lattice expands, there is a reduction in the atomic forces between the atoms corresponding to softer springs. We can use thermodynamics to get the magnitude of the lattice expansion contribution to the anharmonic entropy.

The expansion of the lattice against the bulk modulus requires elastic energy. The vibrational entropy must balance this and can be calculated as

$$S^{Anh}_{Vib,Elastic}(T_1, T_2) = \int_{T_1}^{T_2} 9B\nu\alpha^2 dT \ , \tag{3.19}$$

where B is the bulk modulus, ν is the specific volume, α is the coefficient of thermal expansion, and T_1 and T_2 are the low and high temperatures over which the anharmonic changes occur. Ideally, the low temperature, T_1, would be as close to 0 K as one can get experimentally. However, often this is 300 K as it is experimentally easier to measure the DOS at this temperature.

3.4 Bond-Length vs. Bond Stiffness

We often find ourselves needing the ability to predict the relationship between a bond's length and its stiffness (or force constant). The bond stiffness and how it changes with various conditions is directly related to the DOS and how the DOS changes with the same

conditions. Stiffer bonds result in a DOS that exists at higher energies while softer bonds correspond to smaller energies. Recently, there has been theoretical work on this matter that can help us in the bond length vs. bond stiffness question.

Although we seek intuition and understanding, the theoretical community's interest in the question of bond length vs. bond stiffness has also been derived from the need for calculational efficiency. The largest portion of ab-initio calculations of phonon DOS comes from the time spent calculating the force constant tensor. The primary goal of the work on this matter has been to reduce this time by using force constants calculated for one structure to predict another structure's force constants. Sluiter et al.[66] and van de Walle and Ceder[74] found that force constants are not directly transferable between different structures. However in the work by van de Walle and Ceder[74] it was shown that in general a particular chemical bond will stiffen as the bond length decreases. Therefore by breaking apart the structure into bond types (A-B, A-A, and B-B) and considering the change in the length of these bonds after a phase transition van de Walle and Ceder can gain better precision in their calculations. An extensive review of this subject is found in Ref. [76]. We can therefore be somewhat secure in assuming that for a given chemical bond, if the bond length is decreased the bond will stiffen.

Chapter 4

Vibrational Entropy of Spinodal Decompostion in FeCr

4.1 Introduction

This work explores the contribution of vibrational entropy to the phase stability of FeCr. The Fe-Cr system has a region of spinodal decomposition in its phase diagram. Spinodal decomposition has been a phenomenon of much theoretical debate over the years and continues to be re-examined. Since the famous Cahn-Hilliard non-linear diffusion equation[9, 10] many improvements have been made to decomposition theory. The original advancements simply increased the precision of the non-linear term.[69, 38, 72] Now that modern computers are capable of calculating the full diffusion equation, simulations have been used to describe the dynamics of decomposition.[51, 49, 70] Recently, a new method to calculate decomposition based on the Onsager equation has been developed[78] and modified[35]. During spinodal decomposition of Fe-Cr, the alloy that is originally in a state of solid-solution decomposes, or unmixes, in a continuous process into a state with Fe-rich and Cr-rich regions. The internal energy term favors a completely un-mixed state, while the configurational entropy of mixing promotes the fully mixed state. Unlike structural phase transitions, which occur from one crystal structure to another, each structure with its own free energy curve, spinodal decomposition occurs within a single crystal structure with a single free energy curve that in a simple model has a double minima at low temperatures where the internal energy term dominates over the entropy term. At high temperatures the

configurational entropy works to stabilize the solid-solution state. Thus the internal energy must overcome the configurational entropy contribution at lower temperatures in order to un-mix. The curvature of each term in the free energy with respect to concentration drives the decomposition. Appendix A gives a brief introduction to spinodal decomposition. It is not clear how or if the vibrational entropy would be concentration-dependent, or even if it is important.

A large amount of work has been done on the Fe-Cr system. Much of this work has focused on the spinodal decomposition region of the alloy due to its connection with the brittleness of ferric stainless steels.[81, 79] Therefore the kinetics of decomposition has been of particular interest.[73] Mössbauer spectroscopy[13] and position-sensitive atom probe[47, 48, 11, 29] continue to be utilized in these studies to view the configurational state as a function of decomposition, the latter obtaining a three-dimensional atomistic sample mapping.

Thermal neutron scattering from cubic crystals can be used to measure directly the vibrational density of states (DOS) of an alloy. The quasi-harmonic approximation gives a way to calculate the vibrational entropy from the DOS. However the spectra measured by neutron scattering for an alloy are weighted by the scattering efficiency of each elemental isotope in that alloy. Therefore unless isotopes are combined in proper proportions to balance scattering from all elements, which is not always possible and can be prohibitively expensive, the spectra provide a neutron-weighted DOS (NWDOS). Here a novel approach is used to correct for neutron-weighting, thus obtaining a true DOS from which the vibrational entropy of decomposition is measured, –0.17 $\pm$ 0.01 $k_{\mathrm{B}}/atom$. This vibrational entropy is approximately equal to the configurational entropy of decomposition. Additionally, the critical temperature for spinodal decomposition is lowered by 20% of its original value by including the vibrational entropy into the free energy.

4.2 Experimental Methods

Shots of 99.99% Fe and 99.995% Cr were weighed to make stoichiometric FeCr samples within an error of 0.1 atomic percent. These were then arc-melted in an argon atmosphere, with negligible mass loss and little visible surface oxidation. FeCr ingots were cold-rolled to

1.5 mm thick, optimizing the sample geometry for a 10% neutron scatterer. Next, samples were heat-treated to obtain various states of decomposition. The decomposed samples were annealed at 500 °C in a small argon atmosphere for 12, 46, and 433 hours and allowed to air cool. The solid-solution sample was quenched into ice brine from 1000 °C.

X-ray diffraction data were taken on an Inel CPS-120 position-sensitive detector with Co Kα radiation. These data confirmed that the crystal structure was body-centered cubic. Determining the extent of decomposition of each sample is not easily done by x-ray diffraction. However, Mössbauer spectrometry is an ideal technique to determine the amount of decomposition attained by the anneal, especially for ferromagnetic Fe-rich phases. Mössbauer spectrometry measures the chemical environments surrounding the Fe atoms. Spectra consist of dips (hereafter referred to as peaks) that correspond to the ^{57}Fe nuclear excited state energy splitting caused by the hyperfine magnetic fields (HMF) at ^{57}Fe nuclei.

The Mössbauer spectrometer utilizes a radioactive source, dilute ^{57}Co in Rh, which emits a γ-ray of energy that is approximately equal to the energy of the unperturbed ^{57}Fe nuclear excited state, E_o. This source is mounted on a Doppler drive that oscillates the source, moving it towards and away from a stationary sample. Data are in the form of counts vs. velocity of the Doppler drive, where velocity is directly related to energy. From the Mössbauer spectra of the Fe alloy, it is possible to tell how many Cr atoms are first nearest neighbors (1nn) around each Fe atom. This is covered more thoroughly in section 4.3.1. The Mössbauer spectra that were measured are consistent with previous experimental data.[13]

Time-of-flight inelastic neutron scattering data were taken on both the Low Resolution Medium Energy Chopper Spectrometer (LRMECS) and the High Resolution Medium Energy Chopper Spectrometer (HRMECS) at the Intense Pulsed Neutron Source in Argonne National Laboratory. On both chopper spectrometers the thin walled aluminum cans, 7 cm x 10 cm and 10 cm x 11 cm respectively, of powder samples were measured at a 45 degree angle w.r.t. the incident beam, minimizing self-shielding. LRMECS data were measured with an incident energy of 55 meV; 60 meV was used for HRMECS. All samples were mounted on a displex refrigerator and measured at room temperature and atmospheric pressure. Spectra from empty aluminum cans were also obtained for both instruments.

Spectra were re-binned into energy from time-of-flight. Data were corrected for detector

efficiency using a white beam vanadium spectrum and normalized w.r.t. the incident flux on the samples. The time-independent background was removed. The time-dependent background empty can spectra were then removed from their corresponding sample spectra. Detector data were re-binned into angular bins of 10 ° each. LRMECS data angular range was taken to be 60 ° to 120 °. The low angle data were neglected to significantly reduce any magnetic scattering. The HRMECS data angular ranges were 38 °–59 °, 88 °–91 °and 102 °–133 °. Spectral data less than approximately 5 meV were linearly approximated in the hydrodynamic limit. All extra factors in the one-phonon double-differential cross-section were divided out, leaving the NWDOS in an iterative incoherent approximation process that converges on the mean-square displacement of the atoms from equilibrium and the 2-5 multiphonon scattering. [5] The iterative process assumes a one-phonon scattering function to create a vibrational density of states. The NWDOS is used to find the two through five multiphonon scattering contribution to the scattering function which is then removed. The above data reduction is described in detail in sections 3.1.2 and 3.1.3.

4.3 Results

4.3.1 Mössbauer Spectroscopy

Mössbauer spectroscopy measures the local environment at Fe atoms through effects of HMF. Cr neighbors contribute to that HMF by contracting the full width of the spectra w.r.t. a pure Fe spectrum. Each Fe with m Cr neighbors within the shell of interest contributes a sextet of peaks that is added to produce the total spectra. Using the additive perturbation model (APM)[22], these sextets can be modeled, including isomer shifts, to fit the experimental spectra and find the concentration of Cr in Fe. The APM calculates shifts in reference to a pure Fe sample. The isomer shift moves the sextet for Fe with m Cr neighbors uniformly by an amount $m\Delta i$. The isomer shift depends on the element being alloyed with Fe. In our case, Cr has an isomer shift of $\Delta i = -0.02\ mm/sec$, slightly shifting all sextets to lower velocities than the pure Fe spectra.

In the case of Cr in Fe, the first and second nearest neighbor shells (1-2 shells) can be considered as one shell because the HMF and isomer shift contributions are equal for 1nn

and 2nn chromium. The sextet is composed of three pairs of peaks, each at approximately $\pm v_i$, where i goes from 1 to 3. These peaks are approximately positioned at points that are symmetric across $v = 0$. From the APM the Δv_i^m or difference in velocity between peaks in pair i, for Fe with m Cr neighbors in the shell of interest, each pair represented by i, can be measured.

$$\Delta v_i^m = \Delta v_i^{Fe} + m\Big[\Delta H_{1,2}^x + \kappa c\Big]\Big(\frac{\Delta v_i^{Fe}}{330kG}\Big)\ , \tag{4.1}$$

where $\Delta H_{1,2}^x$ is the change in the HMF of Fe due to one Cr in the 1-2 shells, Δv_i^{Fe} is the full width of pure Fe spectra, m is the number of Cr neighbors in the 1-2 shells around each Fe, and κ is the cumulative contribution to the HMF of Cr in neighbor shells beyond the 2nn shell. For Cr the 1nn shell (eight atoms for bcc) and 2nn shell (six atoms for bcc) are combined into one shell of 14 atoms. In the calculation of the APM all numbers of Cr neighbors have been considered, therefore, $m \in \{1, 2, ..., 14\}$. Eq. 4.1 gives the sextet positions for Fe atoms having m Cr atoms in the 1-2 shells. By a linear combination of sextets calculated using Δv_i^m for $m \in \{1, 2, 3, 4, 5\}$, the positions of all peaks in the measured spectra are calculated. The relative intensities of the component peaks must also be included in the calculation. The pure Fe sextet peak intensities, from negative velocity to positive velocity, are typically 3, 3, 1, 1, 3, and 3. We assume a random solid-solution and use the binomial distribution factors to weight the population distribution fractions of Cr neighbors for Fe in the shell of interest at a given concentration. The binomial distribution factor is

$$P(M, m, \chi) = \frac{M!}{m!(M-m)!}\chi^m(1-\chi)^{M-m}\ , \tag{4.2}$$

where M is the total number of neighbors in the shell of interest, m is the number of Cr neighbors in the shell of interest, and χ is the concentration of Cr for the alloy. Because the 1-2 shells have been combined into one shell for Cr, $M = 14$.

Our solid-solution spectrum was broader than previous work done on Fe-60 at. % Cr[13]; however this is still consistent as the larger Cr concentration will contract the distribution. The decomposed data are superpositions of two spectra: one from the Fe-rich regions of the

sample, which will be similar to pure Fe, the other from the Cr-rich regions of the sample. In the spectrum from material subjected to a 433 hour anneal, the Cr-rich region gives a paramagnetic peak in the spectra. Experimental Mössbauer spectra from all samples can be seen in Fig. 4.1. The dashed lines are the best fit of the APM to the spectra giving a Cr percentage, χ. For the solid-solution spectra, χ is the original Cr concentration of 50%. For the decomposed spectra, χ is the Cr concentration in the Fe-rich regions. This measured composition is an average composition, therefore it should slightly take into account the interfacial regions where the sample changes from Fe-rich to Cr-rich. The composition deduced for the most decomposed sample is consistent with previous measurements of the spinodal for this alloy after an anneal of 433 hours at 500 °C.[80, 13]

4.3.2 The FeCr Neutron-Weight Correction

In our case, natural Fe scatters neutrons three times more than natural Cr, or $\sigma_{Fe}/m_{Fe} = 3\sigma_{Cr}/m_{Cr}$. The iterative technique, described previously in Chapter 3, results in the NWDOS, thus the Fe PDOS is overweighted by a factor of 3.

Ruckert, Keune, and Sturhahn, et al. have performed inelastic nuclear resonant x-ray scattering (INRXS) on various α-Fe(001)/Cr(001) multilayer materials produced by molecular beam epitaxy with different layering orders.[31, 60] INRXS measures only scattering from ^{57}Fe thus, obtaining the ^{57}Fe PDOS. Novel experiments were performed using ^{57}Fe, which has resonant scattering, and ^{56}Fe, which does not. The experimenters directly measured PDOS for monolayers of ^{57}Fe atoms in different layer positions, which corresponds to ^{57}Fe PDOS from Fe with increasing numbers of Cr neighbors in the 1-2 shells of ^{57}Fe. Table 4.1 gives data labels and layering order for each of the INRXS samples.

Equation 3.8 showed that the linear combination of PDOS from each alloy component combines to make the DOS of the alloy. To approximate a neutron-weight correction for our data using the experimental INRXS data, the Fe PDOS must be broken apart further into a linear combination of Fe PDOS with increasing numbers of Cr neighbors in the 1-2 shells. This additional separation of the PDOS assumes that the DOS of the alloy is primarily described by first and second nearest-neighbor interactions, a reasonable assumption as the force constants for Fe and Cr are dominated by the 1-2 shells. For our data this means that

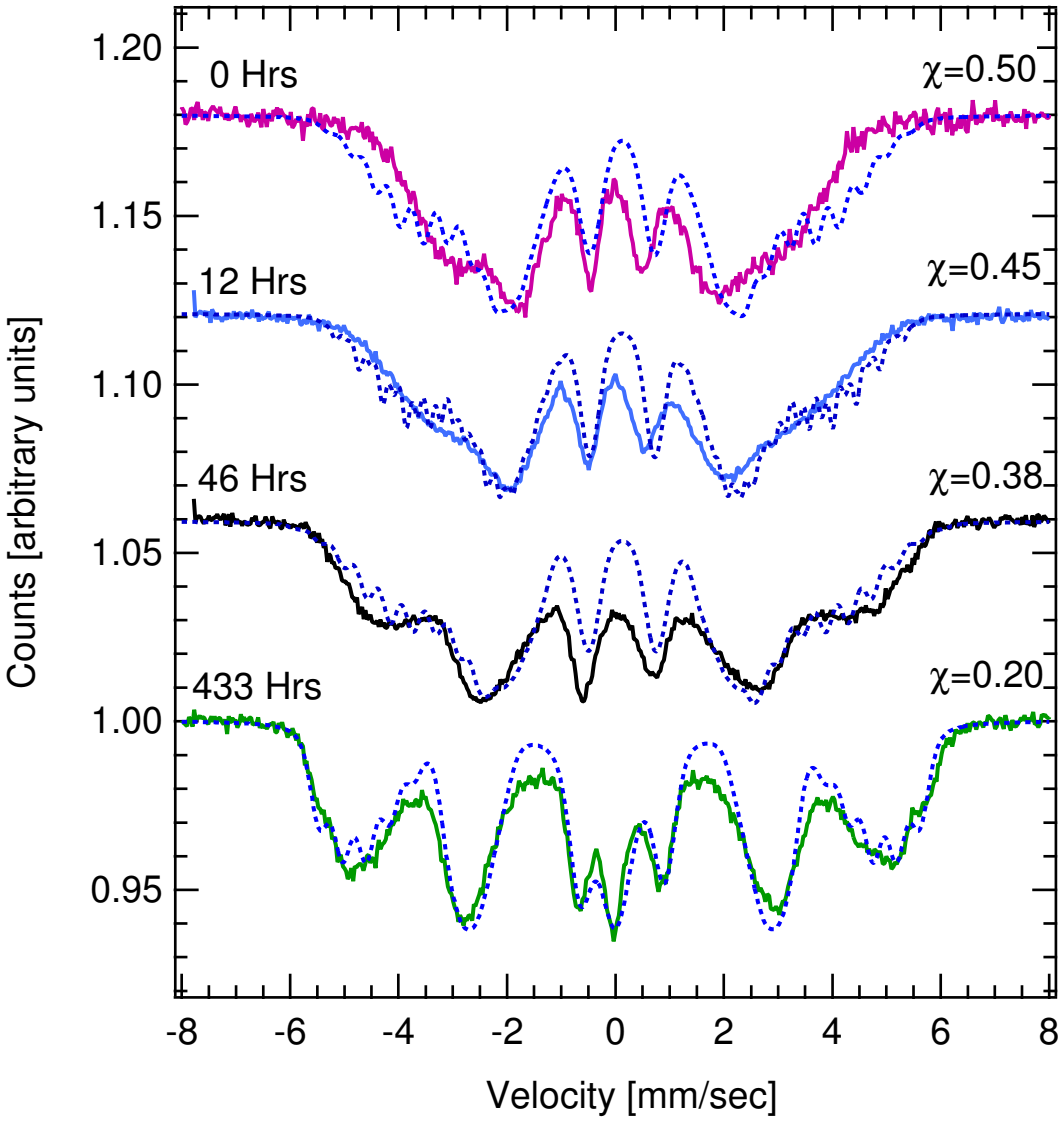

Figure 4.1: Experimental Mössbauer data from all samples. The additive perturbation model was used to calculate all fits to the experimental spectra and are shown as dotted lines. The Cr concentration of the sample or Fe-rich regions (where appropriate) are also given.

Label	FeCr1	FeCr2	FeCr3	FeCr4
Layering Order	^{56}Fe/ ^{57}Fe/ ^{56}Fe	Cr/^{57}Fe/ ^{56}Fe	Cr/^{57}Fe/Cr	$^{57}Fe_{0.03}Cr_{0.97}$
μ	0	5	10	13.58
$\{m\}_\mu$	[0,1,2]	[3,4,5,6,7,8]	[9,10,11]	[12,13,14]
$\sum_{m\in\{m\}_\mu} P(\chi = 0.20)$	0.448	0.552	0.000	0.000
$\sum_{m\in\{m\}_\mu} P(\chi = 0.38)$	0.054	0.904	0.042	0.000
$\sum_{m\in\{m\}_\mu} P(\chi = 0.45)$	0.017	0.864	0.117	0.002
$\sum_{m\in\{m\}_\mu} P(\chi = 0.50)$	0.006	0.782	0.206	0.006
$\sum_{m\in\{m\}_\mu} P(\chi = 0.55)$	0.002	0.661	0.320	0.017
$\sum_{m\in\{m\}_\mu} P(\chi = 0.62)$	0.000	0.452	0.494	0.054
$\sum_{m\in\{m\}_\mu} P(\chi = 0.80)$	0.000	0.044	0.508	0.448

Table 4.1: Inelastic nuclear resonant x-ray scattering Fe-Cr multilayer sample information.[60] In samples FeCr1, FeCr2, and FeCr3 the ^{57}Fe layer is a monolayer or one atom thick. The layers surrounding the ^{57}Fe layer are significantly thick. FeCr4 is a regular bulk non-layered alloy of $^{57}Fe_{0.03}Cr_{0.97}$.

we should further separate the Fe PDOS into a linear combination of PDOS from each Fe with m Cr neighbors in its 1-2 shells,

$$g_{Fe}^{\chi}(E) = \sum_{m\in[0,1,2,..14]} P(M=14,m,\chi) g_{Fe,m}(E)\ , \tag{4.3}$$

where χ is the Cr concentration of the alloy, and $g_{Fe,m}(E)$ is the Fe PDOS for Fe with m Cr neighbors in its 1-2 shells. Unfortunately, the INRXS data were obtained for only four samples, each with a certain number of Cr atoms in the 1-2 shells of ^{57}Fe, where μ is the number of Cr neighbors for these samples. Thus by re-binning m into μ we obtain the fraction of Fe atoms in the alloy $Fe_{1-\chi}Cr_{\chi}$ that have μ Cr first and second nearest-neighbors. This binning range will be referred to as $\{m\}_{\mu}$. Values for μ and $\{m\}_{\mu}$ are given for each INRXS sample in Table 4.1. Incorporation of the new re-binning changes Eq. 4.3 to

$$g_{Fe}^{\chi}(E) = \sum_{\mu} [\sum_{m\in\{m\}_{\mu}} P(M=14,m,\chi)] g_{Fe,Layered}^{\mu}(E), \tag{4.4}$$

where $g_{Fe,Layered}^{\mu}(E)$ is the normalized measured Fe PDOS from the layered INRXS samples. The values of $\sum_{m\in\{m\}_{\mu}} P(M,m,\chi)$ for each χ are seen in Table 4.1. Equation 4.4 is an approximation for the Fe PDOS of a random bcc Fe-Cr binary alloy with Cr concentration χ. Thus, Eq. 4.4 was used to correct the neutron-weighting of the solid-solution data, $\chi = 0.5$. Equation 4.4 is in a form where it can be used in Eqs. 3.8 or 3.10.

However, for the 433 hour anneal data there is a 50% volume fraction of $\chi = 0.2$ and a 50% volume fraction of $\chi = 0.8$. This complicates the Fe PDOS by dividing it into two Fe PDOS–one for the Fe-rich region and one for the Cr-rich region. Thus the combined Fe PDOS including the concentration factor is:

$$g_{Fe}^{\chi}(E)\chi_{Fe} = \sum_{\chi=0.2,0.8} \chi\nu_{\chi} g_{Fe}^{\chi}(E), \tag{4.5}$$

where ν_{χ} is the volume fraction associated with each χ. Equation 4.5 is in a form where it can be substituted into Eqs. 3.8 or 3.10. It should be noted that the probabilities are normalized:

$$\sum_{m} P(M,m,\chi) = 1 = \sum_{\mu} [\sum_{m\in\{m\}_{\mu}} P(M,m,\chi)]. \tag{4.6}$$

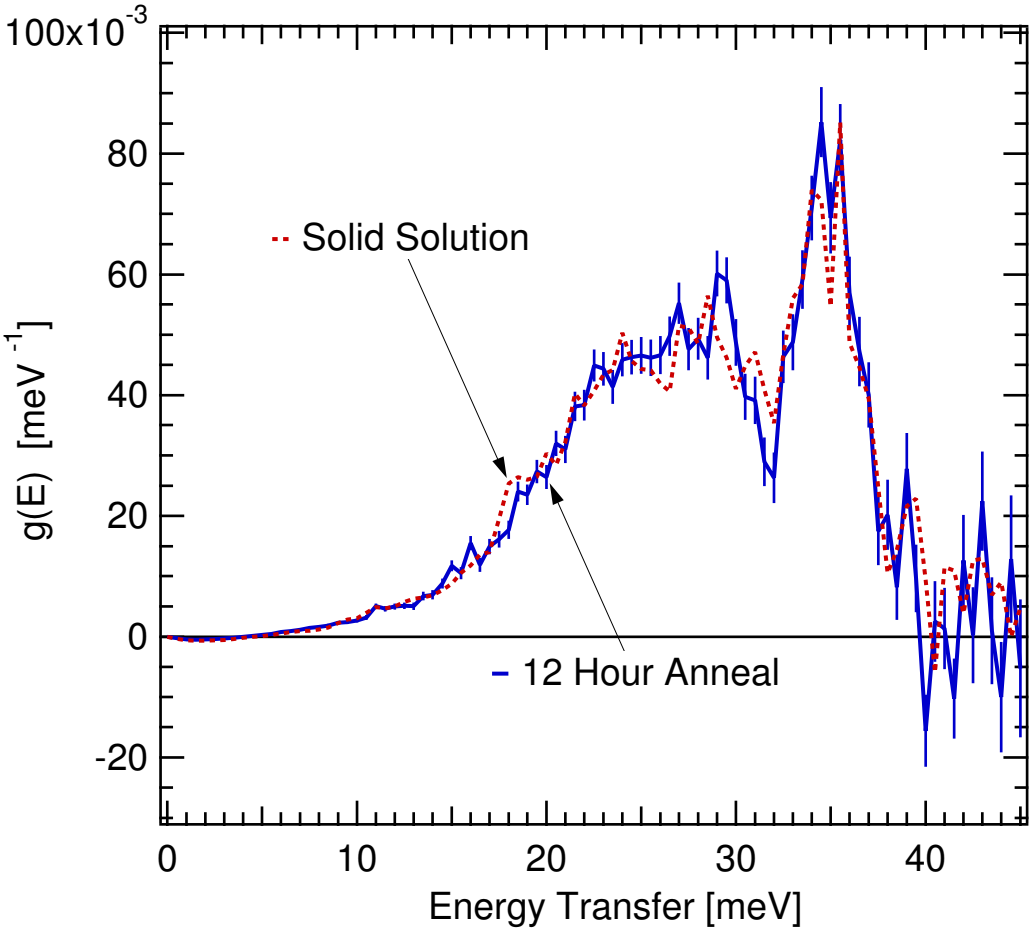

Figure 4.2: Neutron-weight corrected density of states of FeCr, measured on LRMECS at the Intense Pulsed Neutron Source.

The calculated Fe PDOS can then be employed in a neutron-weight correction for the solid-solution and the 433 hour anneal. From Eq. 3.10 the process for a neutron-weight correction is clear. The Fe PDOS is used along with the weighting factors $\chi\sigma/M$, which are all known, to isolate the Cr PDOS in the measured data. Once the Cr PDOS is isolated the true, unweighted DOS (Eq. 3.8) is calculated. These corrected DOS curves are seen in Fig. 4.2 and Fig. 4.3. The decomposed samples show a distinct and increasing stiffening of all modes with the amount of decomposition. All modes of the DOS stiffen monotonically with decomposition of the alloy. This stiffening will suppress the vibrational entropy.

The quasi-harmonic vibrational entropy is calculated by Eq. 3.12 with $T_m = 20\,^{\circ}\mathrm{C}$ and $T_p = 500\,^{\circ}\mathrm{C}$. The vibrational entropy of decomposition is then given by

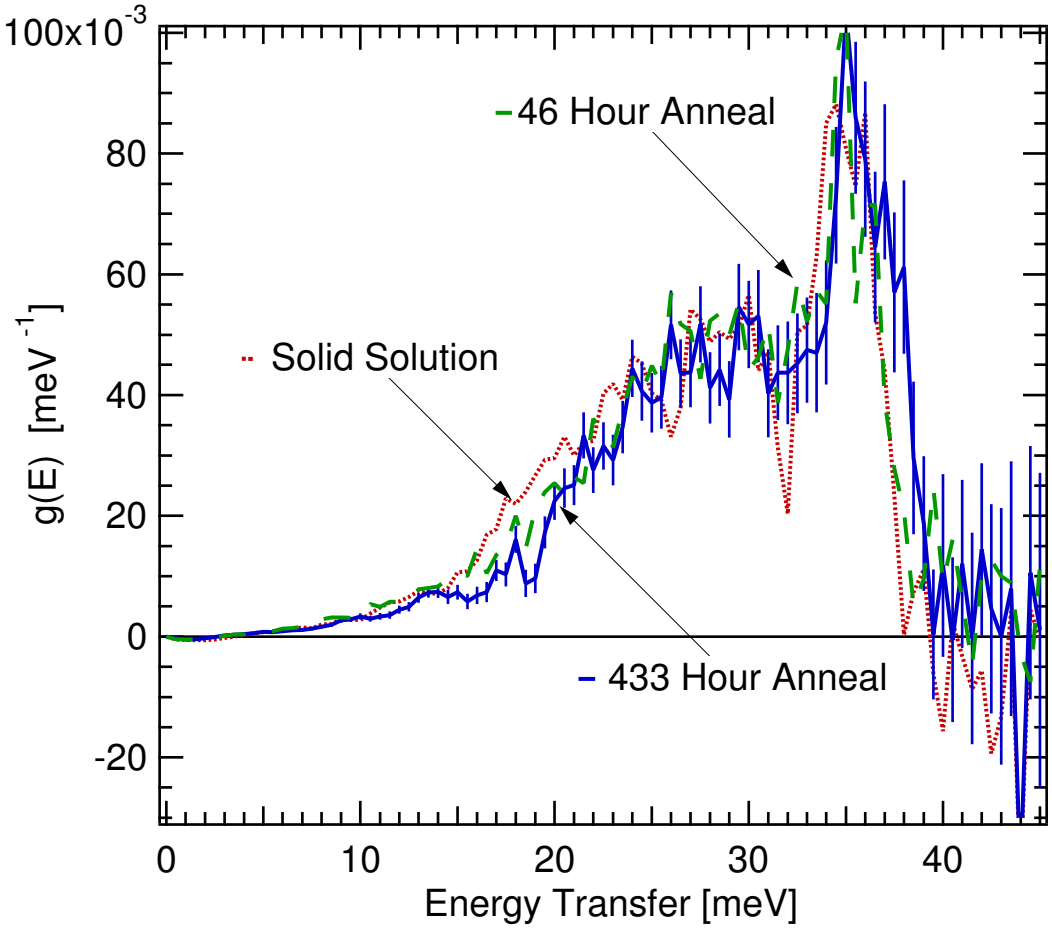

Figure 4.3: Neutron-weight corrected density of states of FeCr. Neutron-weight correction was performed using previously measured Fe partial density of states from α-Fe(001)/Cr(001) multilayers.

$$\Delta S_{V,anneal\ time} = S_{V,anneal\ time} - S_{V,solid\ solution}\ , \tag{4.7}$$

and was calculated for all anneal times. The results were $\Delta S_{V,12Hr}$ = –0.01 ± 0.01 $k_{\mathrm{B}}/atom$, $\Delta S_{V,46Hr}$ = –0.035 ± 0.01 $k_{\mathrm{B}}/atom$, and $\Delta S_{V,433Hr}$ = –0.17 ± 0.01 $k_{\mathrm{B}}/atom$.

4.4 Discussion

4.4.1 Comparison to Configurational Entropy

Configurational entropy calculations for disordered binary alloys have grown beyond the simple model of the point approximation, Eq. 1.2, for a perfectly disordered alloy. The cluster variation model has proven to be more accurate. Experimentally, previous diffuse x-ray scattering measurements on $Fe_{0.53}Cr_{0.47}$ found a slight clustering in the alloy.[59] However, for the purpose of a simple comparison between the configurational entropy and the vibrational entropy, Eq. 1.2 will be useful and adequate. It is, nevertheless, worth noting that the cluster variation model will calculate a smaller configurational entropy than Eq. 1.2 by constraining the configurational possibilities. Thus Eq. 1.2 will give the uppermost bound on the configurational entropy. When considering this effect on $\Delta S_C = S_C^{433Hr} - \Delta S_C^{Solid\ Solution}$ it is clear that if the solid-solution sample experiences some clustering as expected, ΔS_C^{simple} will be larger than the true ΔS_C^{real}. It is also worth noting that using Eq. 1.2 to calculate the configurational entropy for the decomposed alloy also assumes implicitly an atomically sharp interface between large Fe-rich and the Cr-rich regions. However in reality the interface in a spinodally decomposed sample will have some width, perhaps characterized by a function resembling the error function. This means that the calculated ΔS_C^{simple} is larger than ΔS_C^{real}. Because the APM gives an average Cr concentration for the Fe-rich zones, the clustering and interface is included in that average to some extent. Thus the correction to ΔS_C^{simple} for obtaining a true ΔS_C^{real} could be small. For our two extreme concentrations of Fe-50 at. % Cr and Fe-20 at. % Cr, Eq. 1.2 gives a maximum possible value for the change in configurational entropy, $\Delta S_C^{simple} = -0.19 k_{\mathrm{B}}/atom$. Thus, $\Delta S_V \geq \frac{8}{9}\Delta S_C$, a truly thermodynamically significant result. Figure 4.4 shows the full comparison between the vibrational and configurational entropy of decomposition as a function of annealing

time, and hence degree of decomposition.

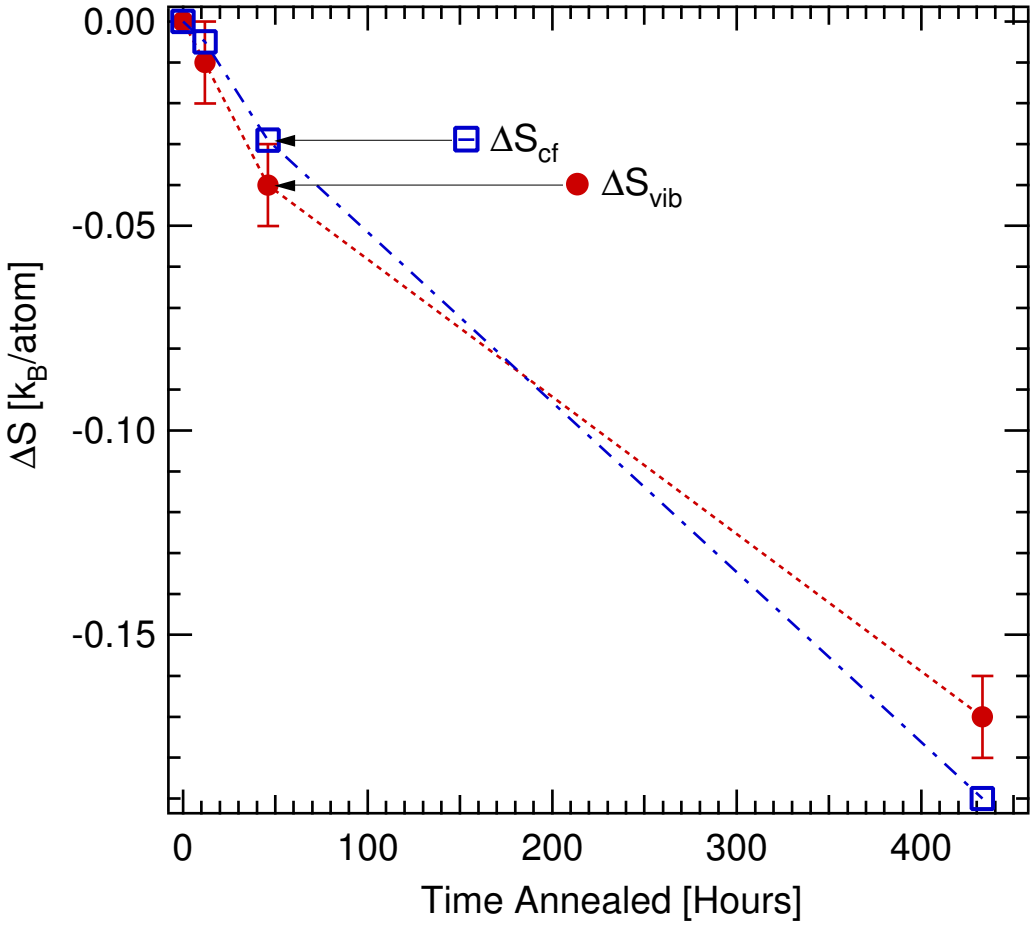

Figure 4.4: The development over time of the neutron-weighted vibrational entropy of decomposition.

4.4.2 Effect on Critical Temperature

In the mean-field approximation, spinodal decomposition in a binary alloy of solute concentration χ occurs below a critical temperature T_{C}, at which the curvature of the free energy with respect to concentration is zero at χ. The fractional change of the critical temperature by including the vibrational entropy with the configurational entropy, as opposed to the configurational entropy alone, depends on curvatures with composition

$$\frac{T_{\mathrm{Ccf}} - T_{\mathrm{C}}}{T_{\mathrm{Ccf}}} = \frac{S''_{\mathrm{vib}}(\chi)}{S''_{\mathrm{cf}}(\chi) + S''_{\mathrm{vib}}(\chi)} \,, \tag{4.8}$$

where T_{Ccf} is the critical temperature assuming all entropy is configurational, T_{C} is the critical temperature assuming entropy is configurational and vibrational, $S''_{\mathrm{vib}}(\chi)$ is the second derivative of the vibrational entropy with respect to χ, and $S''_{\mathrm{cf}}(\chi)$ is the second derivative of the configurational entropy with respect to χ.

To assess the effect of vibrational entropy on the critical temperature for un-mixing through Eq. 4.8, we used Eq. 1.2 to obtain the curvature $S''_{\mathrm{cf}}(\chi = 0.5) = -4\,k_{\mathrm{B}}/\mathrm{atom}$. Measurements of S_{vib} at different Cr concentrations are needed to obtain the vibrational entropy as a function of χ, and then its curvature. Force constants for Fe and Cr were obtained by fitting triple-axis measured phonon dispersions to a set of Fe-Cr alloys, and these force constants were used in a Born von Kármán simulation to calculate a DOS.[24] These DOS curves gave vibrational entropies shown in Fig. 4.5, from which we obtain an approximate numerical value $S''_{\mathrm{vib}}(\chi = 0.5) = -1.0\,k_{\mathrm{B}}/\mathrm{atom}$. With these curvatures, Eq. 4.8 predicts a decrease in critical temperature for spinodal decomposition of 20%. This is a large effect, and is consistent with the large change in vibrational entropy during spinodal decomposition that was measured in the present work.

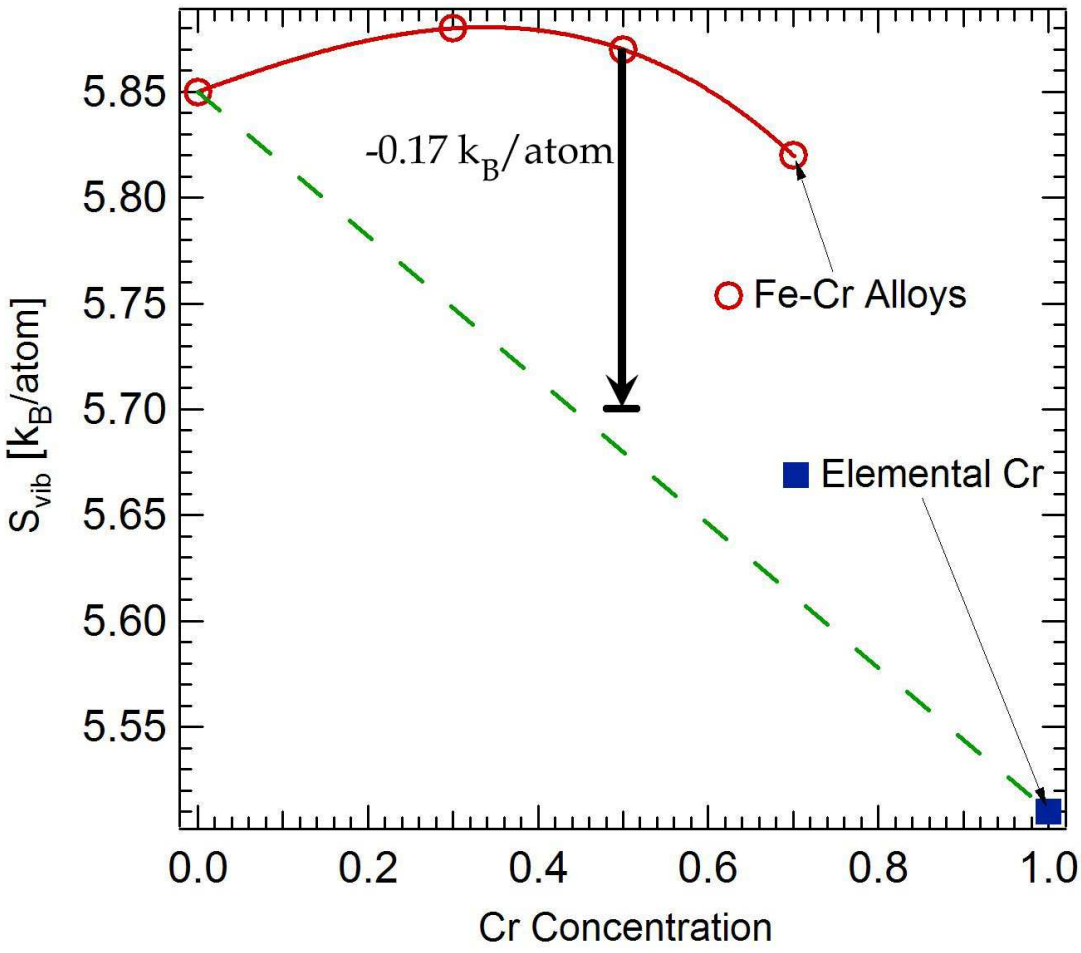

Figure 4.5: Vibrational entropy versus Cr concentration, $S_{\mathrm{vib}}(\chi)$, calculated in the harmonic approximation. The five data points are from triple-axis measurements on Fe and $\mathrm{Fe}_{1-x}\mathrm{Cr}_x$ alloys[24] and Cr.[63] The dashed line connects elemental Fe and Cr. The third order polynomial fit to the alloy data is shown as the solid line and was used to obtain $\mathrm{S}''_{\mathrm{vib}}(\chi = 0.5)$. The magnitude of the measured vibrational entropy of unmixing, $-0.17\,k_{\mathrm{B}}$/atom is shown and labeled.

The low vibrational entropy of the Cr-rich regions does not occur until high Cr concentrations are reached, perhaps correlating with the loss of ferromagnetism. This is consistent with the larger stiffening of phonon DOS for the alloy heat treated for 433 hours, which showed a paramagnetic peak in its Mössbauer spectrum. The change in vibrational entropy after 433 hours (–0.17 k_B/atom), is almost precisely the difference between the entropy of the solid solution and the average entropy of pure Fe and pure Cr, as shown by Fig. 4.5.

The present results, taken with the previous results[24], indicate that the vibrational entropy does not change significantly until zones are formed with high Cr concentration, causing these zones to be destabilized somewhat owing to a higher free energy. The phase boundary for spinodal decomposition therefore should be asymmetrical about the composition of $\chi = 0.5$, being suppressed to lower temperatures at high Cr concentrations. R. O. Williams presented experimental data of the miscibility gap in comparison to theoretical results, see Fig. 4.6.[81] The vibrational entropy would cause an asymmetry such as that seen in these experimental data. It is also possible that the kinetics may be slowed in the later stages of spinodal decomposition owing to this asymmetry of vibrational entropy, but many other factors affect kinetic processes besides the change in free energy. Further study of the vibrational entropy in alloys of high Cr concentration would be appropriate.

4.5 Conclusions

Inelastic neutron scattering spectra were measured for stoichiometric FeCr samples with increasing degrees of spinodal decomposition, giving neutron-weighted vibrational densities of states. It was found that all vibrational modes of the density of states stiffen monotonically as decomposition progresses. Mössbauer spectra confirmed spinodal decomposition of the samples and gave the average Cr concentration from the Fe-rich regions through analysis with the additive perturbation model. A neutron-weight correction was performed, giving the vibrational entropy of decomposition to be –0.17 ± 0.01 $k_B/atom$ after 433 hours of annealing at 500 °C.

The simple model of a perfectly disordered crystal gives the configurational entropy of decomposition to be approximately $-0.19 k_B/atom$, making the vibrational entropy of decomposition approximately equal to the simple configurational entropy of decomposition.

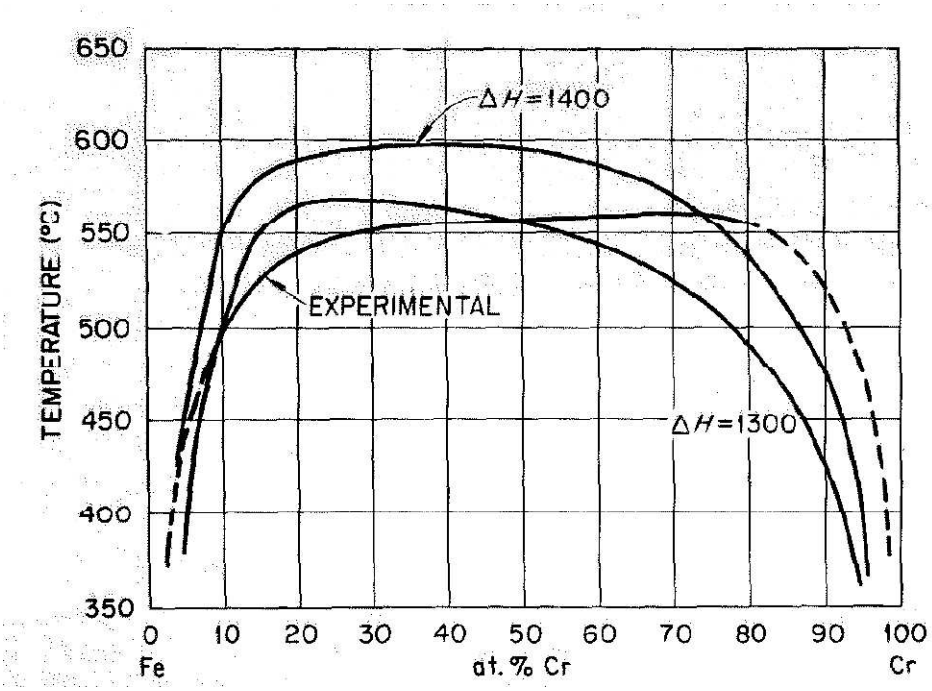

Figure 4.6: Experimental measurement of the miscibility gap in Fe-Cr in comparison to theoretical calculations.[81]

The inclusion of the vibrational entropy term into the free energy calculation was shown to decrease the critical temperature of spinodal decomposition by 20%. The vibrational entropy has been shown to play a thermodynamically significant role in the decomposition of FeCr.

Chapter 5

FeAl Vacancy Effects in Vibrational Entropy

5.1 Introduction

For quite a long time it has been known that aluminum has large vacancy concentrations.[65] However, only more recently has the Al alloy B2 FeAl been noted for its large vacancy concentrations. The phase diagram of Fe-Al is shown in Fig. 5.1[30]. It is now well-known that B2 FeAl has an abnormally high vacancies concentration at high temperature in equilibrium, particularly at off-stoichiometric Al-rich concentrations. Alloys of FeAl have been of interest because of a strong correlation between hardness and heat treatment.[50] It was eventually shown, quantitatively, that the hardness is due to the large vacancy concentration in the alloy, establishing that the hardness is proportional to the square of the vacancy concentration.[14] Chang et al. concluded that vacancies more strongly affect the movement of dislocations in the B2 lattice than do anti-structure atoms. Later, a detailed x-ray diffraction study showed a clear contraction of the lattice parameter with increase in vacancy concentration.[34] Thermodynamic studies of vacancy formation have given valuable insight into the high vacancy concentrations of this alloy. For example, positron annihilation measurements were performed on this system measuring the entropy and enthalpy of vacancy formation.[83]

We have measured the vibrational entropy of vacancy formation in B2 FeAl using inelastic neutron scattering. It was found that vacancies have a relatively small effect on the DOS as a whole. However, the vibrational entropy of formation per vacancy is significant and is negative! Thus the vibrational entropy does not favor vacancy formation.

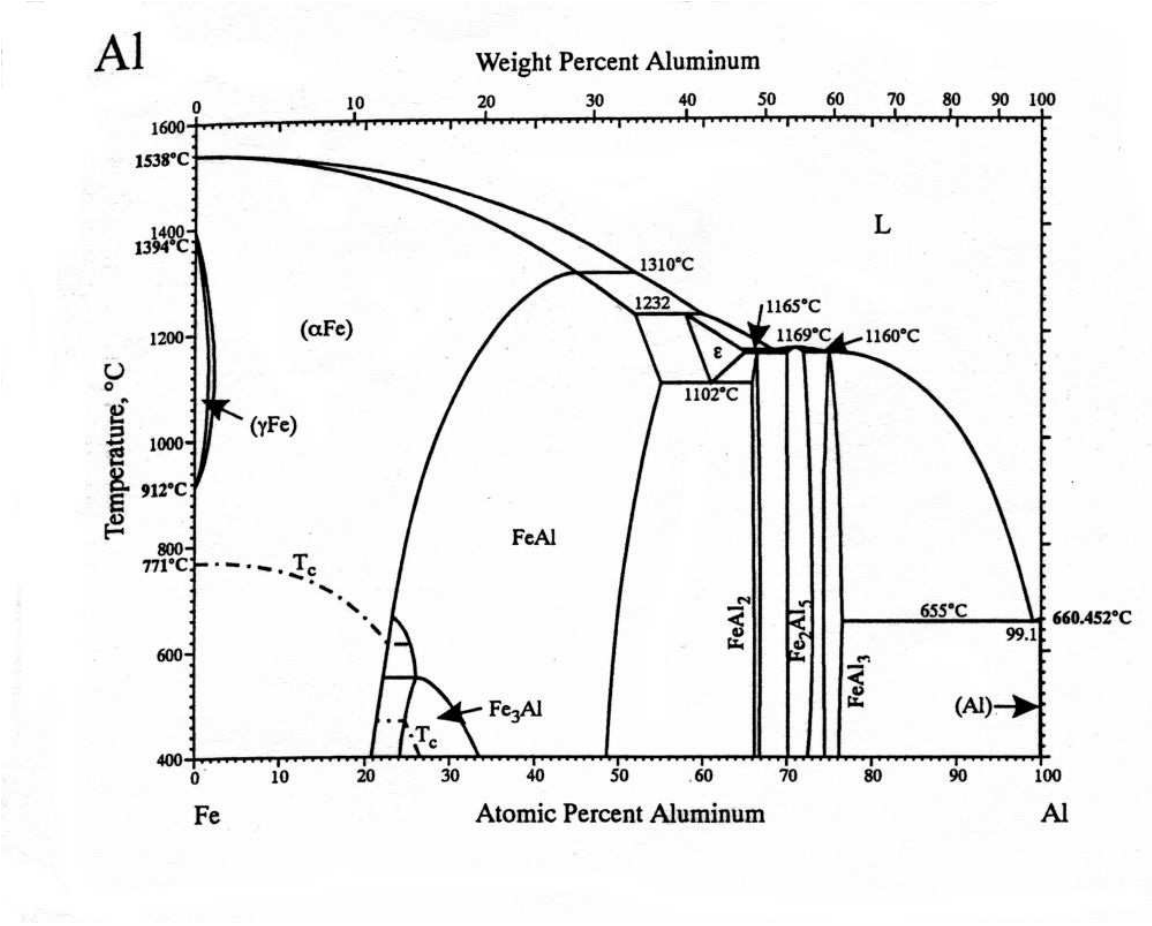

Figure 5.1: Fe-Al Phase Diagram.[30]

5.2 Experimental Methods

Samples of B2-ordered FeAl with 0.5%, 1.8%, 3.1% vacancies were prepared by quenching from 550 °C, 875 °C, and 1100 °C, respectively. The measured samples were prepared as follows. The original ingots were produced by C. T. Liu's research group at the Oak Ridge National Laboratory. These ingots were sliced using electric discharge machining into 1 mm thick pieces to optimize for 10% scattering. The samples were then sealed into argon atmosphere quartz tubes and quenched into iced brine from their respective quench temperatures.

The density, ρ, of each sample was measured via gravimetric analysis using ethanol as the floatation medium. Approximately 22 pieces from each sample were measured giving the statistics in Table 5.1. X-ray diffraction patterns from all samples were acquired using an Inel CPS-120 diffractometer with Co Kα radiation and a position-sensitive detector. A body-centered cubic (bcc) crystal structure was confirmed and lattice parameters were measured by the XRD data. The density measurements along with lattice expansion give the vacancy concentration using a Simmons and Balluffi[65] method of vacancy concentration measurement that was modified to use density, ρ, rather than length, L.

$$\chi_{vac} \approx 3\Big(\frac{\Delta L}{L} - \frac{\Delta a}{a}\Big) \approx \Big(\frac{-\rho}{\Delta\rho} - 1\Big)^{-1} - \frac{3\Delta a}{a} \tag{5.1}$$

The above equation gives the relative vacancy concentration, χ_{vac}, between two samples relative to the low concentration sample. At 550 °C, χ_{vac} does not equal zero. It has been measured that $\chi_{vac} \approx 0.5\%$ at 550 °C.[34] It is necessary to offset the measured χ_{vac} by +0.5% giving the values in Table 5.1.

Sample	ρ [g/cm^3]	σ	a [Å]	χ_{vac} [%]
550 °C	5.57	0.03	2.9168	0.5
875 °C	5.5	0.03	2.9161	1.8
1100 °C	5.48	0.01	2.9079	3.1

Table 5.1: Density measurements

Six pieces were taken from the ingot for electron microprobe measurements. Three to

six positions within these six pieces were then measured for a total of 22 measurements of local chemical composition. The overall average measured alloy concentration was 50.3 ± 0.2 atomic percent Fe and 49.7 ± 0.2 atomic percent Al. Trace amounts of Ni were also measured in the sample, 0.006 ± 0.01. The samples were shown to be reasonably homogeneous in concentration.

We used LRMECS to acquire time-of-flight inelastic neutron scattering data at the Intense Pulsed Neutron Source of Argonne National Laboratory. Samples were mounted in thin-wall aluminum cans, $7\,\mathrm{cm} \times 10\,\mathrm{cm}$, using an incident beam of monochromatic neutrons with an energy of 60 meV. The flat sample packages were tilted at a $45\,^\circ$ angle off the direction of the incident beam to minimize self-shielding. All spectra were measured at room temperature. Background data were acquired from the empty aluminum cans under the same conditions.

The raw data of intensity versus time-of-flight in the different detector tubes were re-processed into intensity versus energy, and then converted into an approximate, or "neutron-weighted" phonon density-of-states using the following steps. The raw data were corrected for detector efficiency using a white beam spectrum from a vanadium plate, and normalized by the incident flux on the samples. The time-independent background was removed. The time-dependent parts of the background acquired from the empty cans were then subtracted. Detector data were re-binned into angular bins of $10\,^\circ$ each, using scattering angles up to $120\,^\circ$. The low-angle data (angles less than approximately $35\,^\circ$) were neglected to minimize contributions from magnetic scattering. After subtraction of an elastic peak centered about 0 meV, the data below approximately 5 meV were approximated as a straight line, as expected in the continuum limit. Corrections were then made for thermal factors and multiphonon scattering (two- through five-phonon processes), using an iterative procedure in the incoherent approximation (see sections 3.1.2 and 3.1.3).

5.3 Results

5.3.1 Inelastic Neutron Scattering

The neutron-weighted DOS are obtained after performing the above corrections. These DOS are seen in Fig. 5.2. The scattering weight ratio Fe:Al of 3.74:1 is quite large, requiring a neutron-weight correction.

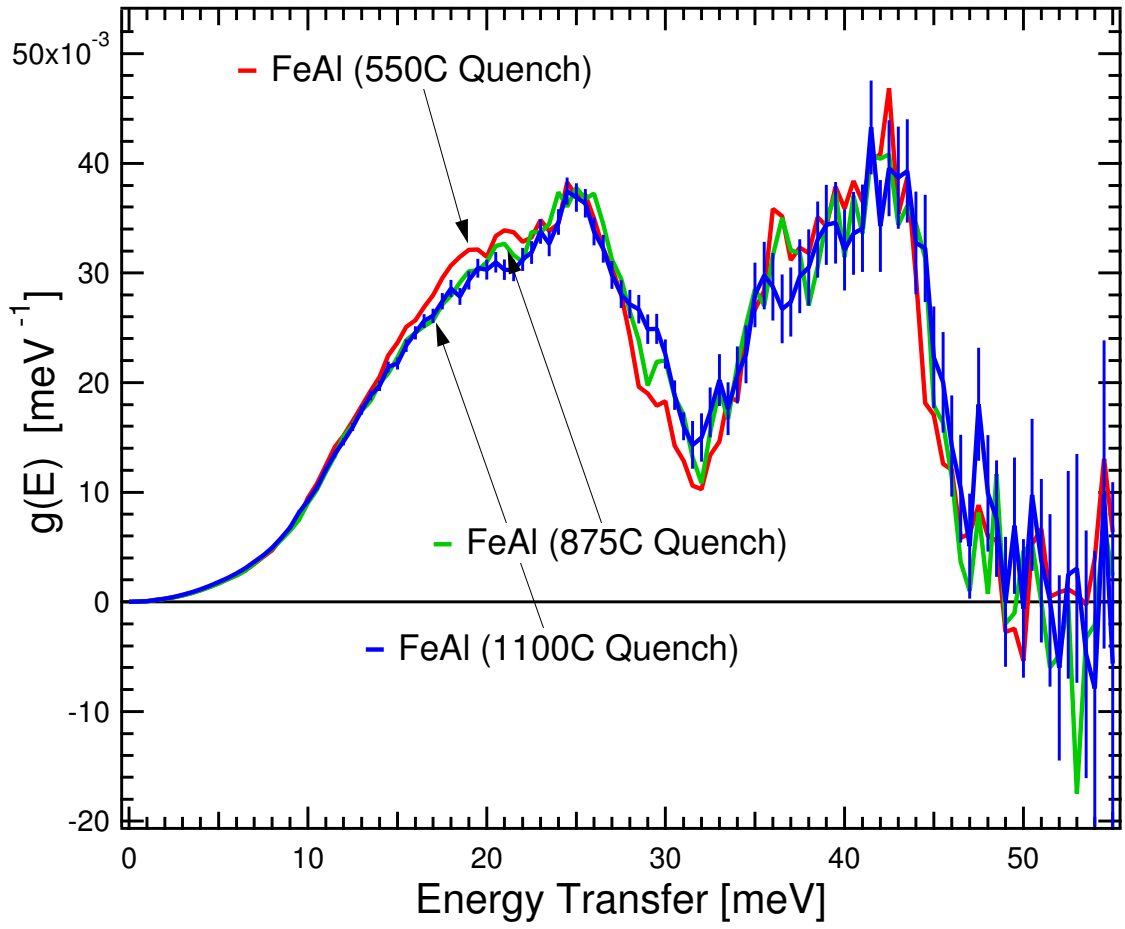

Figure 5.2: Neutron-weighted FeAl DOS.

A neutron-weight correction is possible because B2 FeAl has a two atom basis (i.e., the crystal is ordered). Therefore this system will have both acoustic and optical modes. The number of modes will be divided equally between the optical and acoustic branches. In this particular system the acoustic and optical branches are well-separated. It is therefore possible to simply correct the data such that there are equal numbers of acoustic and optical

modes in the DOS. It is important to understand that this is not a perfect correction, the fine structure of the DOS may be slightly incorrect–peaks associated with the Fe partial DOS will remain slightly over emphasized. However, it is a good approximation. Fig. 5.3 shows the neutron-weight corrected data.

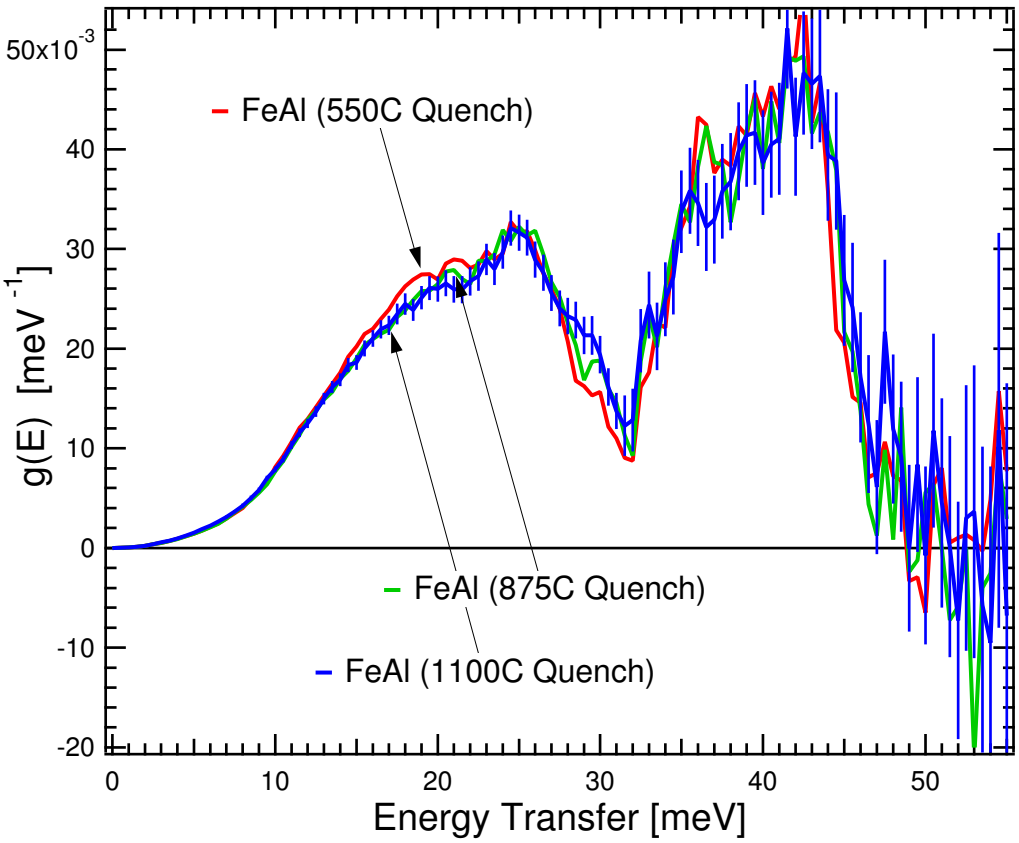

Figure 5.3: The vibrational entropy per vacancy is significant.

B. Meyer et al.[46], calculated the DOS of B2-ordered FeAl using the frozen-phonon and the ab-initio force constant method within the density-functional theory in local density approximation and the ab-initio mixed-basis pseudopotential method, see Fig. 5.4. They calculate phonon dispersion data, which is compared to experiment, Fig. 5.5. The dispersion momentum directions are defined w.r.t. the Brillouin zone in Fig. 5.6. The gap energy between the acoustic and optical modes in the measured DOS data is consistent with calculated DOS of Meyer. We could also use Meyer's DOS to perform a neutron-weight correction. However, as this would not correct the vacancy modes in the low energy gap

region, and as those modes are the only major differences between the measured DOS curves of different samples, this procedure would not affect the measured vibrational entropy of formation.

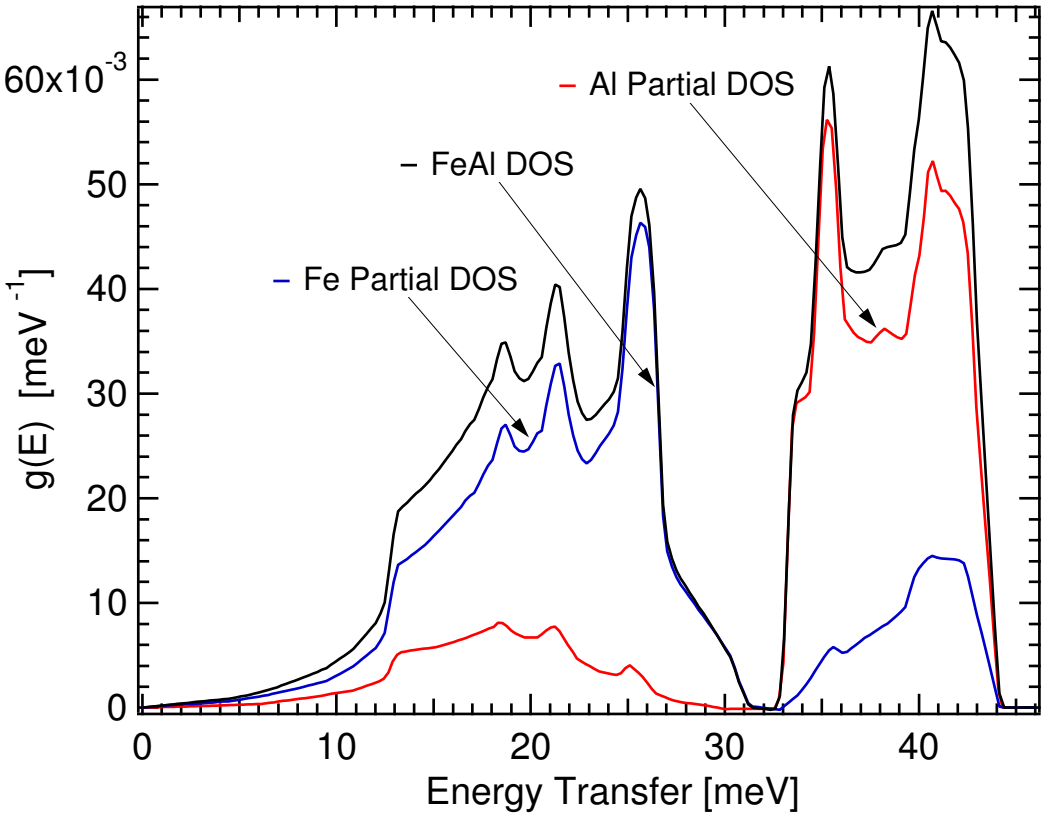

Figure 5.4: Calculated B2 FeAl DOS by Meyer et al.[46]

5.4 Discussion

5.4.1 Changes in the Phonon DOS

We consider crystallographic features that would affect the origin of the observed vacancy effects in the DOS, and we propose an explanation for the changes measured in the DOS. The alloy of B2 FeAl has been studied extensively. In particular, the characteristics of vacancy formation have been a point of extreme interest and much previous work on vacancy configuration as a function of equilibrium temperature will be utilized.

Reasonably modern phase diagrams of the B2 phase region at concentrations near

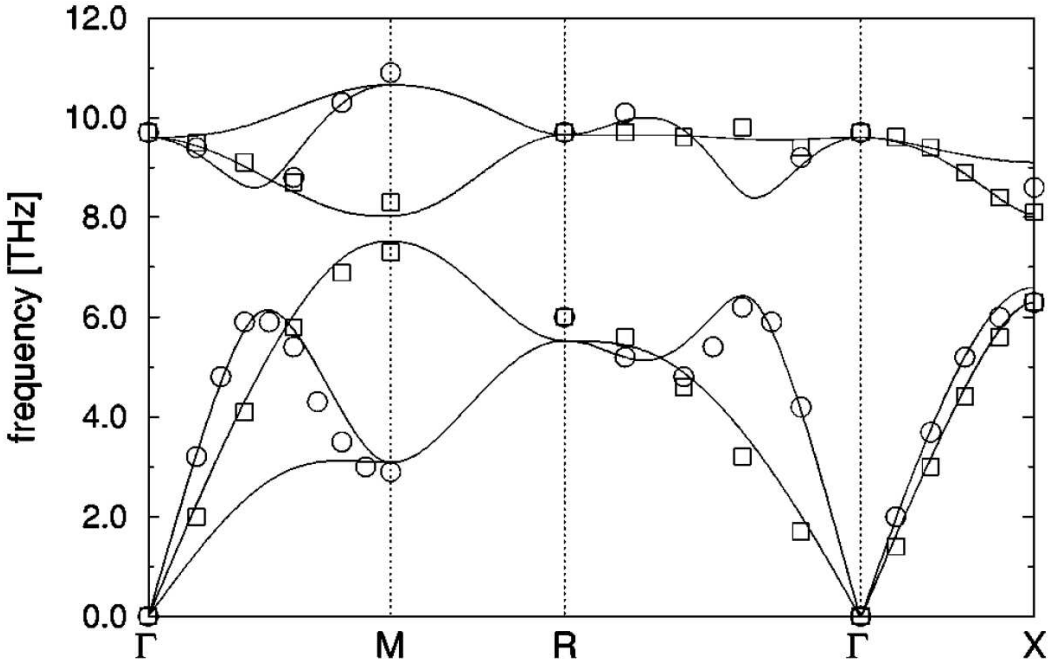

Figure 5.5: Calculated B2 FeAl Dispersions by Meyer et al.[46]

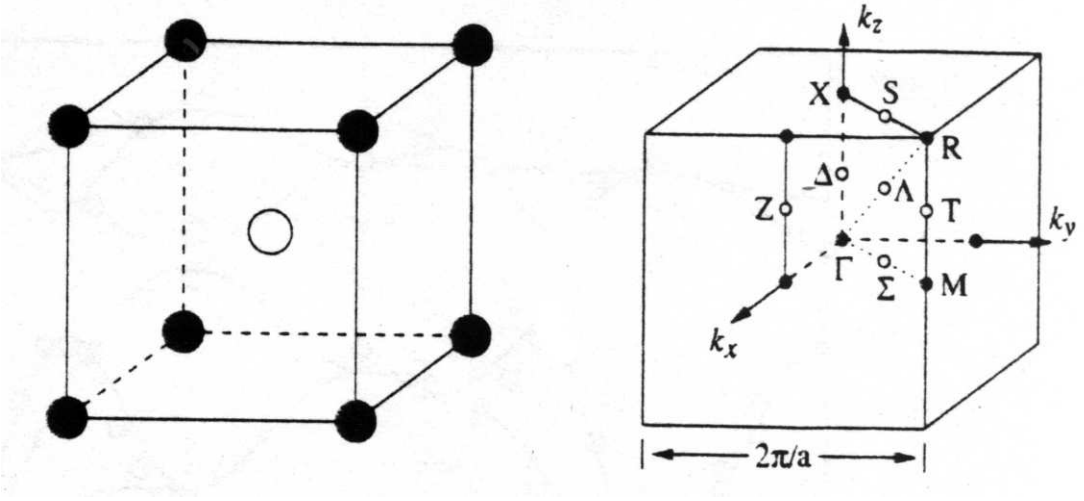

Figure 5.6: Brillouin zone directions used in Meyer et.al.[46]

$Fe_{0.50}Al_{0.50}$ show a high temperature (HT) and a low temperature (LT) region, see Fig.5.7. The two regions are differentiated by their vacancy concentrations. The HT "phase" has a significant increase in equilibrium vacancy concentration.[36]

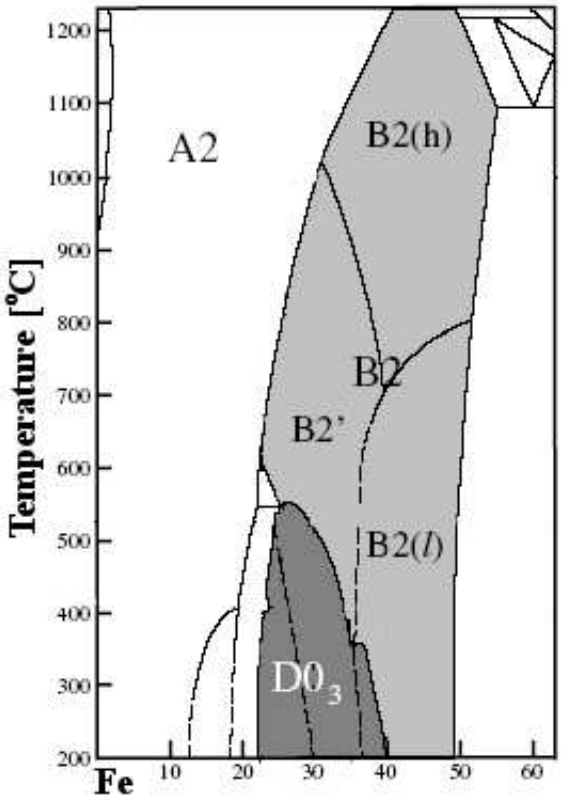

Figure 5.7: Fe-Al phase diagram [36].

Diego et al. have strong evidence that Fe vacancies dominate in the LT region and triple vacancy defects, shown in Fig. 5.8, dominate in the high temperature region of the B2 structure.[15]

Consider which directional interatomic forces will be most affected by the vacancies. All directions will be affected slightly from the contraction of the crystal. However, directions that include both vacancy and interstitial should have larger effects on the force constants. The (1 1 0) direction is an example of this; it also happens to be the most affected direction measured in the DOS.

Figure 5.9 gives a better view of the atomic configuration on a (1 1 0) plane. From

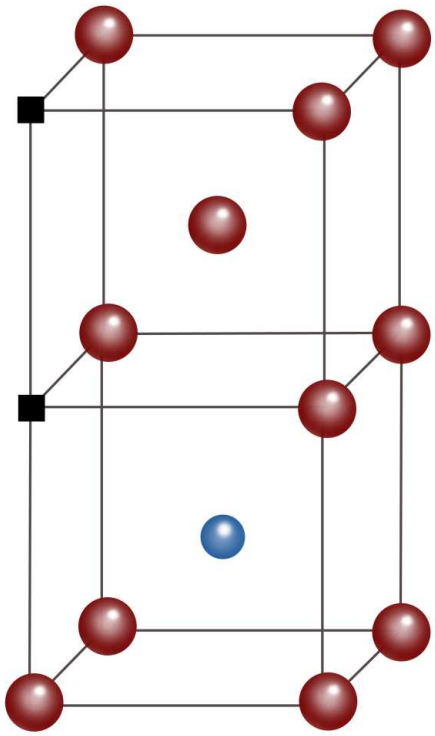

Figure 5.8: Triple-defect configuration at high temperatures.[15] Large balls represent Fe atoms, small balls represent Al atoms, and squares indicate vacancies.

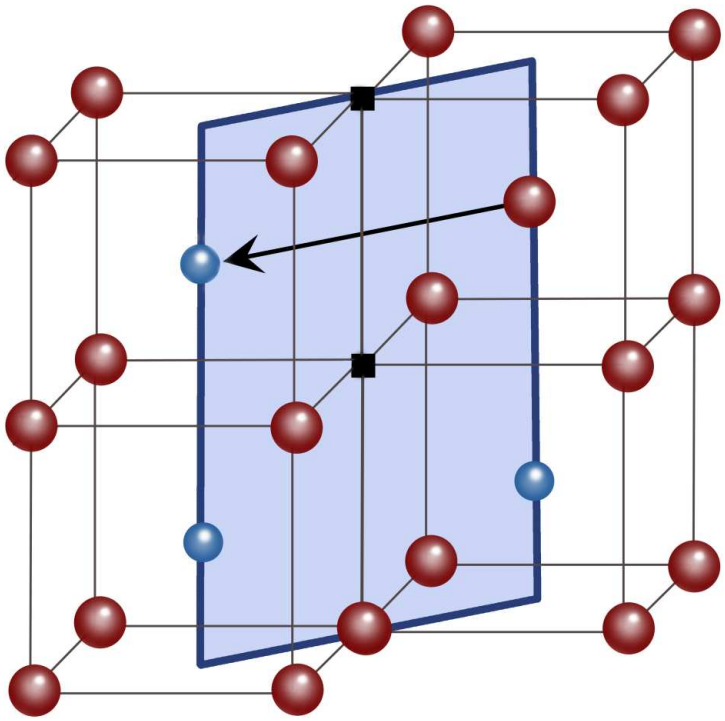

Figure 5.9: (1 1 0) crystal plane is highlighted blue in the triple-defect region of the crystal.[15]

XRD data it is known that the lattice contracts around the vacancy sites. [34] Not only will there be a collapse of the crystal due to the vacancies along that direction which will stiffen the vibrational modes, but the resulting stiffening will most likely be compounded by the anti-site Fe atom.

The anti-site Fe will replace the body-center to body-center Al-Al bond with a Fe-Al bond. Using first nearest-neighbor force constants from Fe, Al, and FeAl we can show that the Fe-Al bond would most probably have a larger force constant than the Al-Al, which would constrain the motions of the Fe and Al in the (0 0 1) direction. This constraint would be along the direction of motion of these atoms in a transverse mode. This is not an exact calculation because the Al crystal structure is fcc (face-center cubic) in comparison to the Fe and Fe-Al bcc structure. The force constants will be affected by the crystal structure and the neighboring bond types of the atoms in question. However, we expect that the forces here are still relevant in their relative magnitude with each other.

To calculate these bond forces we simply use the force constant tensor. When we multiply the direction of motion of the neighboring atom to the tensor the result is the force vector acting on the reference atom caused by the motion of its neighbor. The generic force constant matrix is

$$K = \begin{pmatrix} xx & xy & xz \\ yx & yy & yz \\ zx & zy & zz \end{pmatrix} . \tag{5.2}$$

Both Fe and FeAl are bcc; their K will be simplified by symetry operations to

$$K_{bcc} = \begin{pmatrix} xx & xy & xy \\ xy & xx & xy \\ xy & xy & xx \end{pmatrix} . \tag{5.3}$$

Aluminum is fcc; its K will have a different simplified result:

$$K_{fcc} = \begin{pmatrix} xx & xy & 0 \\ xy & xx & 0 \\ 0 & 0 & zz \end{pmatrix} . \tag{5.4}$$

Consider bcc: the first nearest-neighbor in the bcc structure is along the normalized (1 1 1) direction. Therefore to calculate the force, $\vec{f}_{bcc}$, on the atom at the origin upon motion of the body-center atom in a radial direction w.r.t. the origin atom, we have

$$\vec{f}_{bcc} = K_{bcc} * \vec{r}_{bcc} = \begin{pmatrix} xx & xy & xy \\ xy & xx & xy \\ xy & xy & xx \end{pmatrix} \begin{pmatrix} \frac{1}{\sqrt{3}} \\ \frac{1}{\sqrt{3}} \\ \frac{1}{\sqrt{3}} \end{pmatrix} . \tag{5.5}$$

Values for Fe are $xx = 16.88$ and $xy = 15.01$ arb. units and Fe-Al has values of $xx = 16.563$ and $xy = 18.926$ arb. units. Using these values the magnitude of the force on the atom at the origin is $|\vec{f}_{Fe-Fe}| = 46.9$ arb. units for a Fe-Fe bond and $|\vec{f}_{Fe-Al}| = 54.4$ arb. units for a Fe-Al bond.

The first nearest neighbor in the fcc structure is along the normalized (1 1 0) direction. Therefore to calculate the force, $\vec{f}_{fcc}$, on the atom at the origin upon motion of the face-center atom in a radial direction w.r.t. the origin atom, we have

$$\vec{f}_{fcc} = K_{fcc} * \vec{r}_{fcc} = \begin{pmatrix} xx & xy & 0 \\ xy & xx & 0 \\ 0 & 0 & zz \end{pmatrix} \begin{pmatrix} \frac{1}{\sqrt{2}} \\ \frac{1}{\sqrt{2}} \\ 0 \end{pmatrix} . \tag{5.6}$$

Born von Kármán fits of Al phonon dispersion have measured values of $xx = 10.4578$, $xy = 10.3657$, and $zz = -2.6322$ in arb. units giving $|\vec{f}_{Al-Al}| = 20.8$ arb. units for an Al-Al bond. The Fe-Al bond is significantly stiffer than the Al-Al bond contributing to the stiffening of the transverse acoustic branches. This force constant method is also consistent with the types of bonds that are being dealt with. The Fe-Fe bond is dominated by d-electron bonding, which can be treated in the tight-binding approach. The bond integral, from the overlap of the 3d electrons in a region of potential, is strongly sensitive

to interatomic separation and bond angles. The Al-Al bond is more consistent with a free-electron model, and more sensitive simply to electron density. The Fe-Al bond has been studied by the theory community, and has been found to have significant covalent character.[8, 7, 68, 12] [1] A greater stiffness of the Fe-Al bond than the Al-Al bond is therefore plausible by analysis of bond types and force constants.

As mentioned in Sect. 5.3.1, Meyer et al. calculated the DOS of FeAl using experimental data and a Born von Kármán model. Although Meyer did not include vacancies in their calculations, we can still reference their data to consider which dispersion might be changed by vacancies and cause the shifts seen in our measured DOS. Without having direct dispersion measurements of FeAl with vacancies, it is not possible to know for certain. Because the vacancies produce only very minute changes in the DOS, using Meyer's calculation and previously measured FeAl dispersion data for comparison is quite reasonable. We do not expect the dispersions to change so drastically that a different branch (other than the red branch) would be contributing to this "shoulder." Luckily, only the transverse acoustic dispersion contributes to the "shoulder" at the high energy side of the acoustic modes, thus it is the sole contributor. This dispersion is along the (1 1 0) direction and has been highlighted in Fig. 5.10 as the thick-solid (red) line. The horizontal (green) line in the figure shows the corresponding area in the calculated and measured DOS. It is seen that the increase in modes at the high energy acoustic "shoulder" with increasing vacancy concentration corresponds directly to energies associated with the highlighted (red) (1 1 0) dispersion.

As mentioned, the triple defect could cause a noticeable increase in interatomic forces along the (1 1 0) direction. This would in turn cause the wave velocity, dw/dk, to increase; a dashed (red) line in Fig. 5.10 has been superimposed on the data for an example of what this shift might look like. The dashed line would correspond to the increase in modes at the acoustic "shoulder" caused by vacancies.

[1] Some have even gone so far as to call FeAl intermediate between a metal and a ceramic.

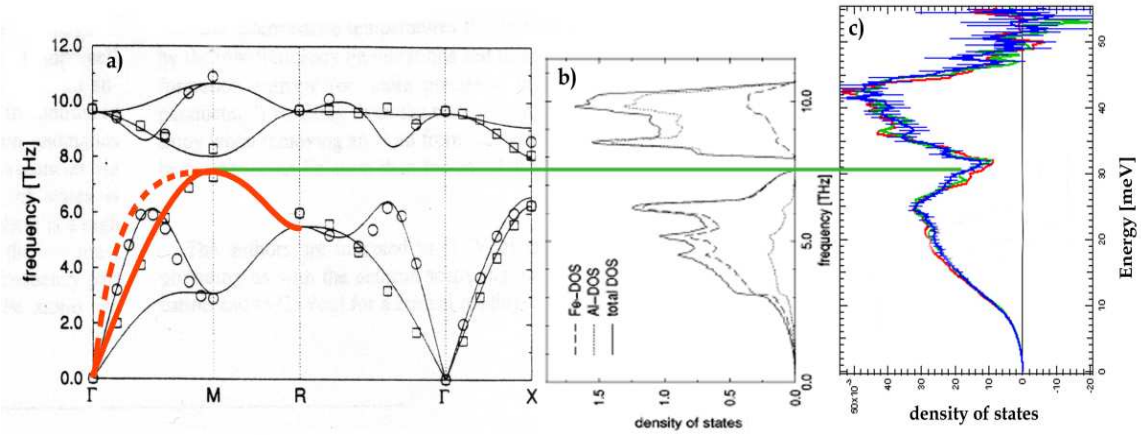

Figure 5.10: (1 1 0) crystal plane in the triple defect.[15]

5.4.2 Vibrational Entropy of Vacancy Formation

Using the quasi-harmonic approximation, Eq. 3.12, the vibrational entropy of each DOS can be determined and results are given in Table 5.2. To convert from vibrational entropy per atom to vibrational entropy per vacancy we use the conversion factor

$$\frac{N-v}{v}\quad\frac{[\#\ of\ atoms]}{[\#\ of\ vacancies]}=\frac{N}{v}-1=\frac{1}{\chi_{vac}}-1\,, \tag{5.7}$$

where N is the number of lattice points in the crystal and v is the number of vacancies in the crystal. So $N-v$ is the number of atoms in the crystal.

Vacancy Concentration [%]	Vibrational Entropy [k_B /atom]	Error [k_B /atom]
0.5	2.95	0.01
1.8	2.93	0.01
3.1	2.93	0.01

Table 5.2: Vibrational entropies if B2 FeAl with quenched in vacancies.

To obtain the average vibrational entropy of vacancy formation between vacancy concentrations 0.5% and 3.1% we have taken the difference in the vibrational entropy per atom from the DOS and then converted using a concentration of 2.6% vacancies to get values per vacancy. The difference in vibrational entropy between the samples with 0.5% and the

3.1% vacancies gives a vibrational entropy per vacancy as $-0.75 \pm 0.53 k_{\mathrm{B}}$/vac. We compare this to the corresponding configurational entropy of formation.

Let us first look at the discrete calculation. We use our measured values for the vacancy concentrations: The $\chi_{vac} = 0.005$ sample would have concentrations $\chi_{Fe} = 0.4975$ and $\chi_{Al} = 0.4975$. Similarly, the $\chi_{vac} = 0.031$ sample would have concentrations: $\chi_{Fe} = 0.4845$ and $\chi_{Al} = 0.4845$. Using the ternary form for the configurational entropy of mixing,

$$S_{conf}(Ternary) = -k_B\Big(\chi_{vac} ln \chi_{vac} + \chi_{Fe} ln \chi_{Fe} + \chi_{Al} ln \chi_{Al}\Big) \,, \tag{5.8}$$

the average configurational entropy of vacancy formation is $S_{conf}(\chi_{vac} = 0.031) - S_{conf}(\chi_{vac} = 0.005) = 3.4 k_{\mathrm{B}}$/vac, making the magnitude of vibrational entropy of vacancy formation 20% of the configurational entropy of vacancy formation.

We can also consider the instantaneous change in the configurational entropy to calculate the configurational entropy of vacancy formation. To do this we use Eq. 5.8 and we set $\chi_{Fe} = \chi_{Al} = (1 - \chi_{vac})/2$, then take the derivative $\partial S/\partial \chi_{vac}$ and evaluate the derivative at $\chi_{vac} = 0.005$ and $\chi_{vac} = 0.031$. By taking the average of these two values we obtain the average configurational entropy of vacancy formation between vacancy concentrations of 0.5% and 3.1%. This was found to be 3.7 k_{B}/atom, similar to the value obtained by taking the discrete derivative in the previous paragraph.

5.5 Conclusions

Due to the small concentration of vacancies with respect to the number of atoms, the vacancies and vacancy related effects on the phonon DOS are small but measurable. When measured per vacancy however, the vibrational entropy of formation is much more significant, –0.75 k_{B}/vac. This is not negligible, however it also is not very large considering that the corresponding configurational entropy of formation is 3.7 k_{B}/vac. The fact that the vibrational entropy of vacancy formation is negative, i.e., not favoring formation, is quite interesting and rather unexpected.

Chapter 6

Anomalous Anharmonicity in FeAl

6.1 Introduction

Most research on FeAl has focused on the thermal vacancies in the system, originating from concerns about the brittleness of this material at temperatures above 400 °C. To date there has been little to no work on the phonon thermodynamics of the B2 FeAl system. Thermal vacancies and point defects could affect the thermodynamics, and are important to know and understand. Our measurements begin to fill this gap in knowledge for the FeAl system.

There has also been much interest in the magnetic states of Fe-Al alloys. Local magnetic moments in Fe around vacancies and defects have been calculated [7, 37] and measured [7] along with magnetic susceptibility [84]. Of most relevance to the present work are the measurements and calculations by Bogner et al. [7], where a compression of the lattice is calculated around Fe anti-site defects due to Fe magnetic moments.

In the present work we found a large softening of the phonon DOS between 10 K and 300 K. However the softening becomes a stiffening of the acoustic modes and a broadening of the optical modes between 300 K and 973 K. This increases even further at 1323 K. The stiffening is quite surprising as the lattice expands between 300 K and 1323 K. We find that the phonons in FeAl show extremely strong anharmonicity even at low temperatures. We explore the possibility that point defects are responsible in part for this anharmonic behavior.

6.2 Experimental Methods

The same B2-ordered FeAl from the last chapter with 0.5%, 1.8%, 3.1% vacancies were used in this experiment. Sample preparation was the same as is described in Ch. 5

Time-of-flight inelastic neutron scattering data were acquired with the LRMECS instrument at the Intense Pulsed Neutron Source at Argonne National Laboratory and the PHAROS instrument at the Los Alamos Neutron Science Center (LANSCE) at the Los Alamos National Laboratory.

Samples for LRMECS were mounted as described in Ch. 5 and the incident energy was 60 meV. Spectra were measured at room temperature and 10 K using the LRMECS displex refrigerator. Time-dependent background data were acquired from the empty aluminum cans under the same conditions.

Samples for PHAROS were mounted in an AS Scientific (ILL) furnace and measured in-situ at 300 K, 973 K, and 1323 K. The samples were placed in a niobium sample holder, made of a single layer of 0.075 mm thick foil. Time-dependent background data were acquired for the furnace without the Nb sample holder. However, the vibrational DOS of Nb has been measured for temperatures 293 K, 773 K, 1773 K, and 2223 K[27]. Negligible softening of the DOS is seen between 293 K and 773 K, and very little softening is observed between 293 K and 1773 K. Low energy modes soften by approximately 1 meV between 293 K and 1773 K, therefore the softening of the Nb sample holder will be less than 1 meV. The cutoff energy undergoes negligible changes between 293 K and 1773 K. Also, because the Nb DOS is at very low energies, with a cutoff energy of 25 meV, the Fe scattering in the sample will dominate over the Al at these energies (see Fig. 5.4). Furthermore, the neutron-weight coefficient of Nb is 1/3 that of Fe. All of this along with the fact that the mass of Nb in the neutron beam was 1/2 that of the mass of Fe means that the Nb scattering intensity is approximately 1/6 that of the Fe scattering. Therefore the scattering from the Nb will not affect the differences between the FeAl DOS at different temperatures. The Nb DOS curves are shown in Fig. 6.1.[27]

All raw inelastic neutron scattering data were processed as before into neutron-weighted DOS curves. The previously described neutron-weight correction was also applied to the 10 K and 300 K data to obtain neutron-weight corrected DOS. Because the high temperature

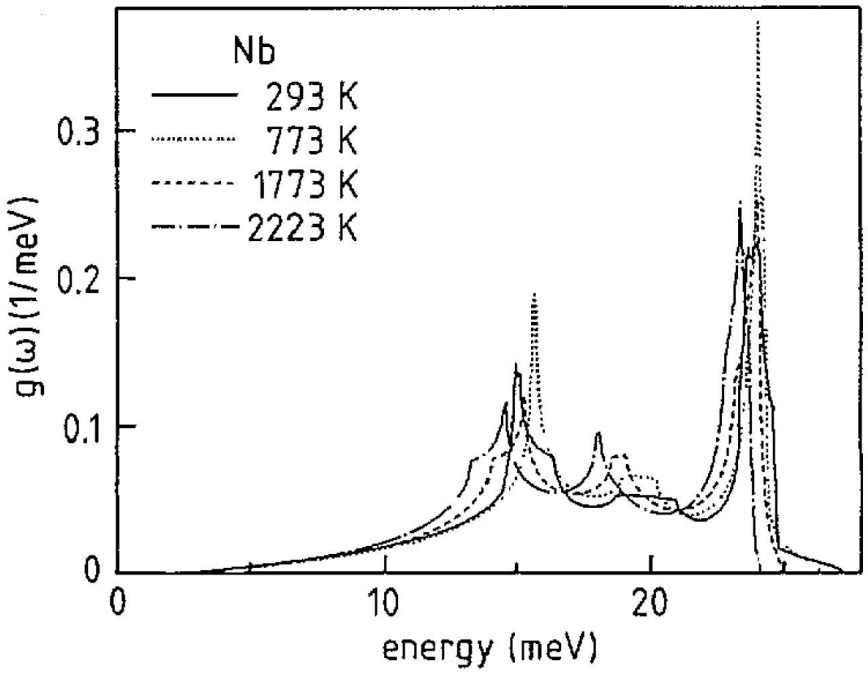

Figure 6.1: The extremely small softening of the Nb DOS with temperature will reduce any effect of the Nb sample holder on the measured temperature dependence of our data.[27]

data do not have well-separated acoustic and optical branches, we are unable to perform a neutron-weight correction.

6.3 Results

6.3.1 Inelastic Neutron Scattering

The room temperature (RT) results are the same data presented in Ch. 5. However the 10 K B2 FeAl DOS proves to be very different from that at RT. There is a large softening of all modes in the RT DOS w.r.t. the 10 K DOS for both vacancy concentrations, as seen in Figs. 6.2 and 6.3.

The DOS from measurements on PHAROS shows a marked stiffening between RT, 700 °C and 1050 °C, this is surprising because the lattice continues to expand within this temperature range. Although states appear in the gap with increasing temperature, modes also expand beyond the original RT cutoff energy. These two effects balance each other

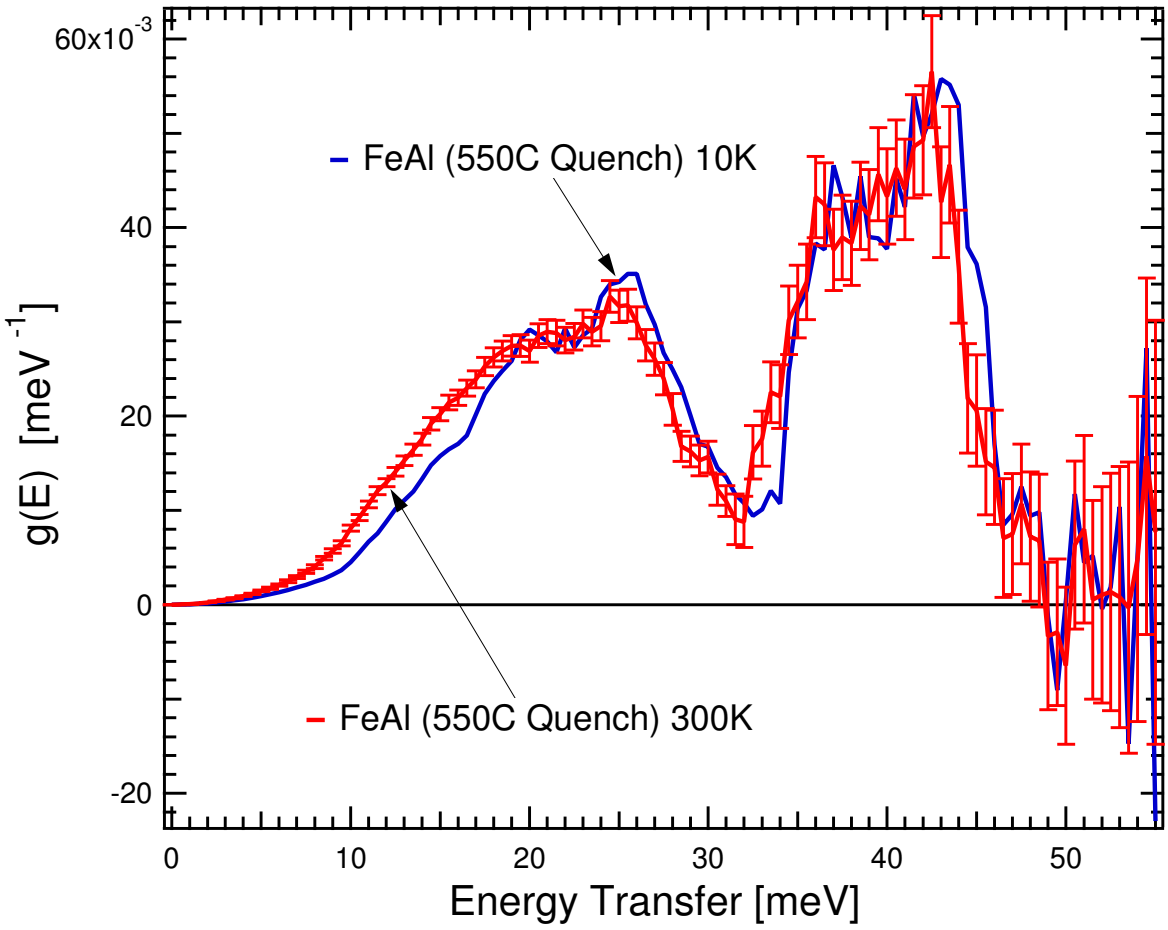

Figure 6.2: A very large anharmonicity is seen considering the extremely low temperatures.

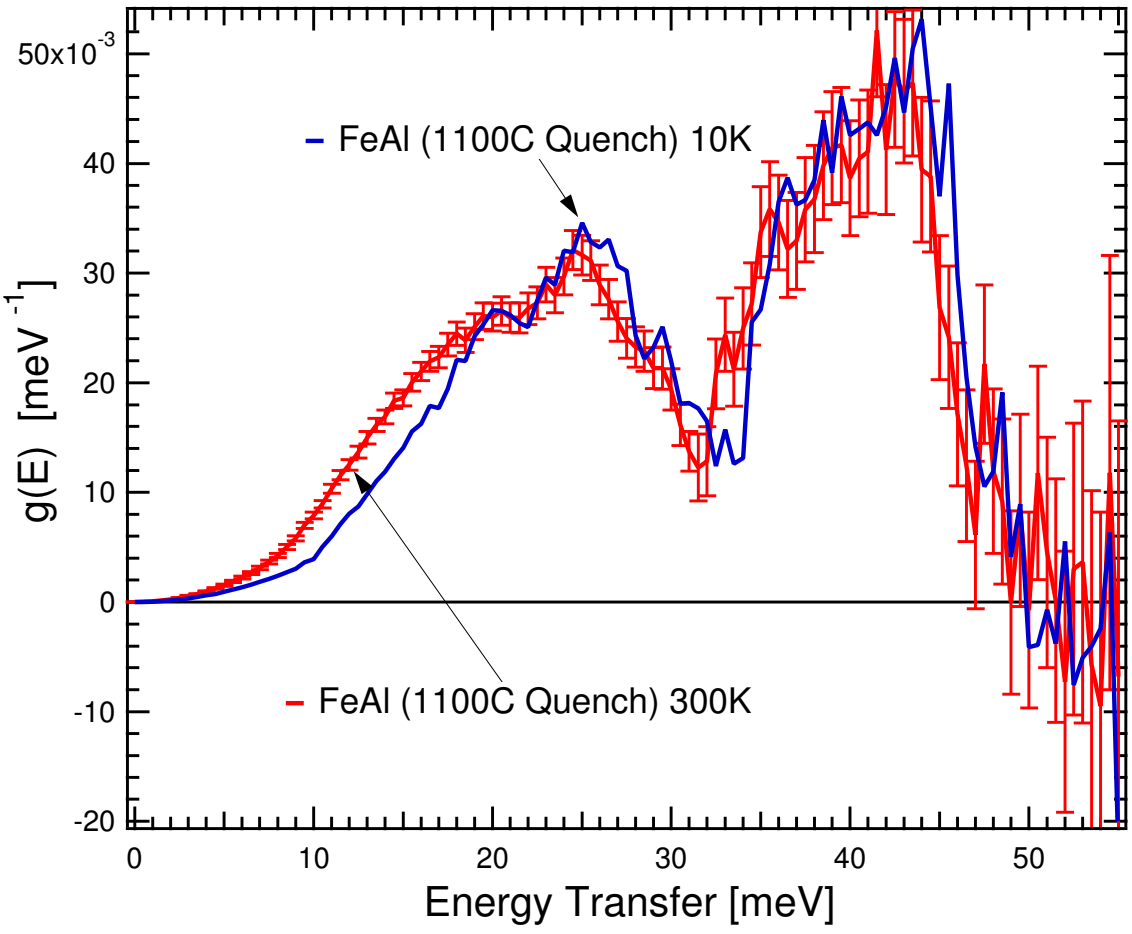

Figure 6.3: A very large anharmonicity is seen at a vacancy concentration of 3.1% (1050 °C Quenched) and is somewhat larger than that of the 0.5% (or 550 °C Quenched) sample.

out entropically, leaving an approximate decrease in vibrational entropy with increasing temperature (see Sect. 6.3.2 for a quantitative calculation).

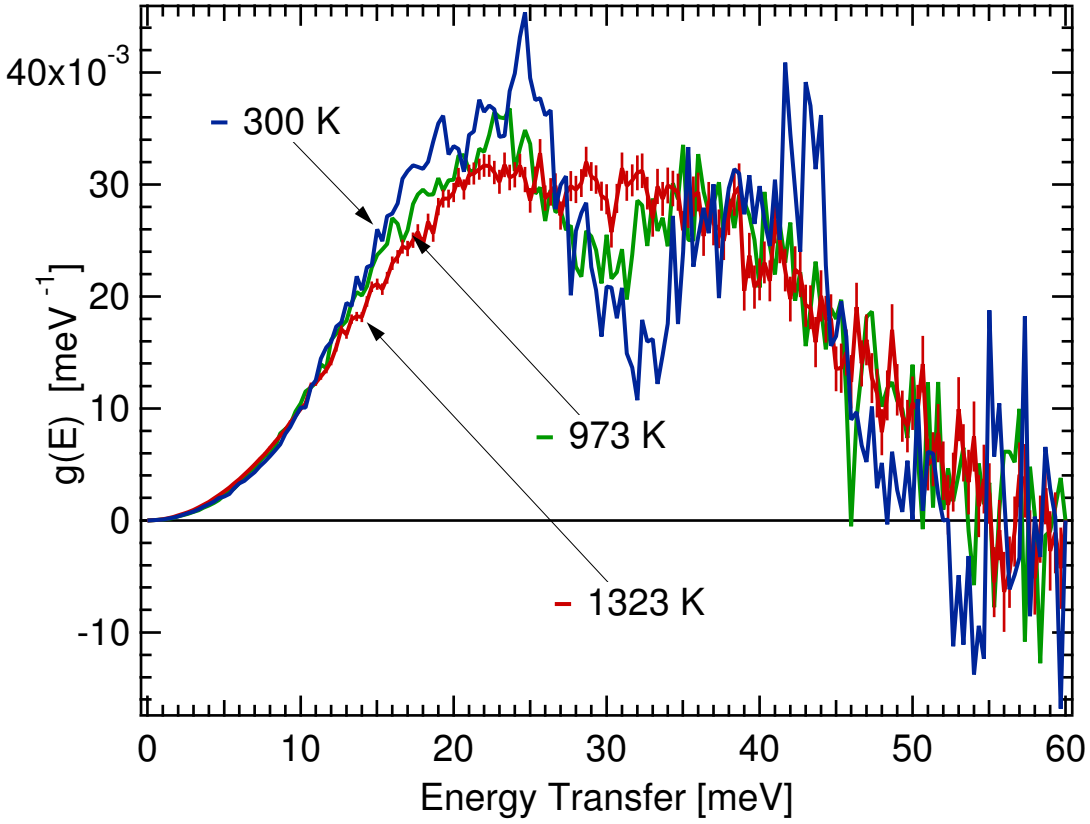

Figure 6.4: In situ DOS measured with corresponding equilibrium vacancy concentrations.

6.3.2 Anharmonic Entropy

The anharmonic vibrational entropy required to balance the elastic energy of lattice expansion between 10 K and 300 K calculated via Eq. 3.19 was found to be 0.04 k_B/atom. The measured anharmonic vibrational entropy calculated via Eq. 3.18 is 0.14 ± 0.01 k_B/atom and 0.17 ± 0.01 k_B/atom for samples quenched from 550 °C and the 1100 °C, respectively. Figure 6.5 gives a comparison of these entropies. The increase in anharmonic vibrational entropy with vacancy concentration is slightly larger than the error bars, $0.03 \pm 0.014 k_B$/atom. We should assume that this is statistically significant. However, it should be noted that there is a certain amount of error in our data analysis routine that is not truly accounted for.

The multiphonon calculation performs a fit to the measured data; this fit has some error associated with it that is not easily incorporated into the DOS error bars and thus the entropy calculation. Unfortunately, incorporating this error would be a very complicated and somewhat subjective maneuver. Thus if we assume this is statistically significant, we are left with the question, why will vacancies cause extra anharmonicity in our DOS in particular an extra softening?

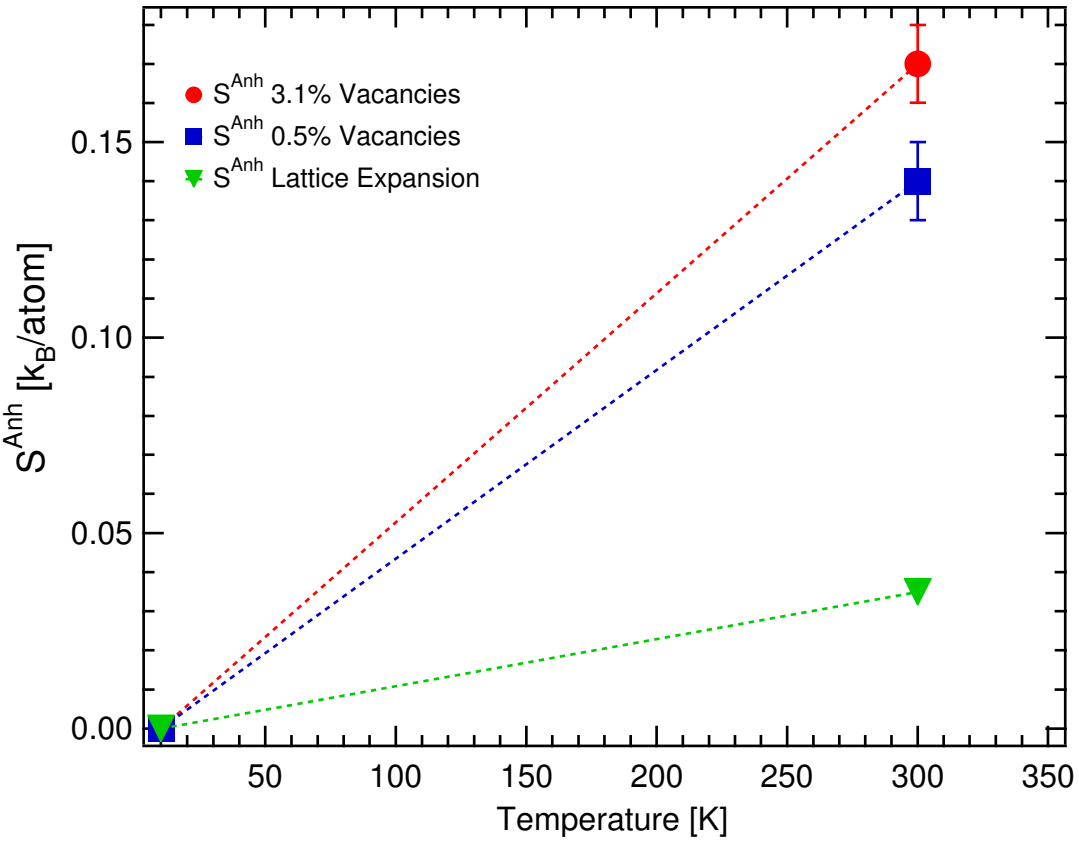

Figure 6.5: Anharmonic vibrational entropy in B2 FeAl as a function of temperature.

The stiffening in the high temperature data w.r.t. room temperature is quite remarkable. In particular, the lattice has been measured to expand with temperature as one would expect[58], meaning that a secondary phenomenon is overpowering the lattice softening of the DOS enough to cause stiffening instead! We will try to explain both the low temperature and the high temperature anharmonicities in the next section.

The anharmonic entropy has been calculated from the PHAROS NWDOS at tempera-

tures 973 K and 1323 K w.r.t. the PHAROS 300 K NWDOS. These measured anharmonicities were then shifted by the anharmonic entropy of the 300 K DOS that was measured on LRMECS. The measured anharmonic entropy calculated via Eq. 3.18 with the above method is plotted as a function of temperature in Fig. 6.6. Also plotted is the anharmonic entropy due to lattice expansion as calculated with Eq. 3.19. One can readily see that the B2 FeAl system has anomalously large anharmonic entropy at 300 K; however, once 973 K is reached the anharmonic entropy is significantly smaller than expected from the lattice expansion.

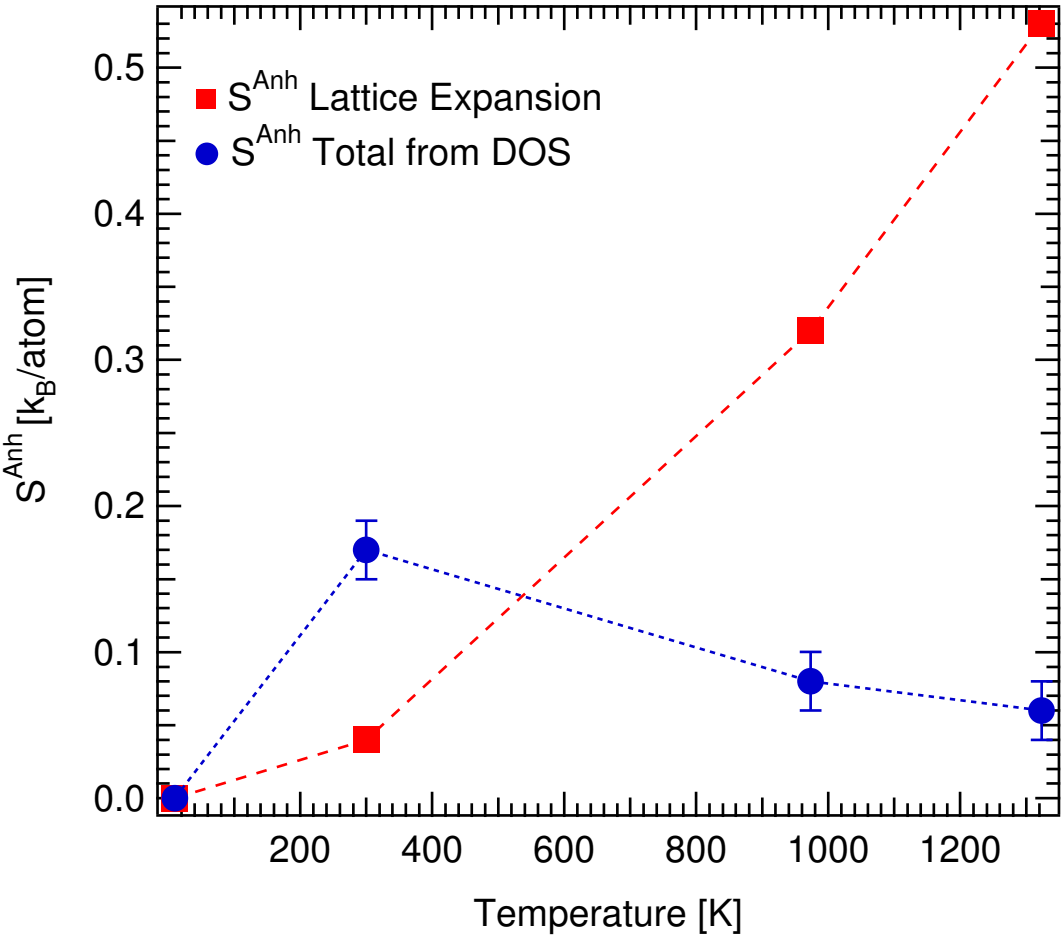

Figure 6.6: Anharmonic vibrational entropy in B2 FeAl as a function of temperature. The data point at 300 K was measured on LRMECS for a sample containing 3.1% vacancies. The data points above 300 K were measured on PHAROS and shifted by the anharmonic entropy at 300 K from LRMECS.

6.4 Discussion

6.4.1 Contributions to the Anharmonicity

Previous linear augmented plane wave (LAPW) calculations in conjunction with Mössbauer spectrometry data on B2 FeAl provide useful information about the local magnetic moment of anti-site Fe atoms[7]. Figure 6.7 shows the two possible point defects considered by Bogner et al. [1] They are the Fe vacancy and the Fe anti-site defect. The arrows in Figure 6.7 show the LAPW calculated relaxation of the atoms in those configurations. Notice that the arrows indicate a compression of the lattice around the Fe anti-site atom.

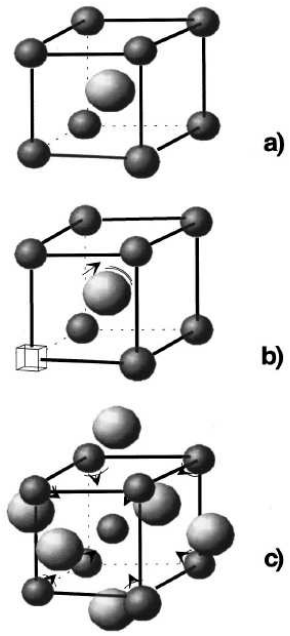

Figure 6.7: (a) Schematic representation of the ordered B2 structure (Al atoms are larger spheres). (b) Inclusion of an Fe vacancy. (c) Environment for an Fe anti-site defect. Arrows mark the relaxation of the atomic positions obtained from the LAPW calculations.[7]

The Mössbauer data analysis by Bogner et al. attributes a magnetic moment only to Fe

[1]They did not include the triple defect defined in Chapter 5. It is not clear whether they do not believe the triple vacancy is probable or whether they chose not to include it for some other reason. Nevertheless we can consider the defects they do include.

anti-site defect atoms and their eight Fe neighbors. The LAPW calculation shows a lattice compression around these Fe anti-site atoms in part caused by the magnetic moment of the cluster. Either the compression of the lattice or the effect of the magnetic moment of the cluster on its force constants could cause a stiffening in vibrational modes. The direction of the stiffening is not so obvious and indeed would most likely occur in more than one direction and in more than one dispersion branch. An overall average stiffening of the DOS may be expected.

Mössbauer data are plotted in Figure 6.8.[7] The spectra have been fit by four separate calculated contributions: perfect B2 ordered Fe, Fe surrounding an Fe vacancy, Fe surrounding an Fe anti-site atom, and Fe anti-site atoms. The largest change in these contributions is seen in the spectrum from Fe surrounding an Fe anti-site atom (dashed-dotted line). This spectrum indicates that these Fe are magnetic, seen as a double peak, at 4.2 K. However this magnetism disappears rapidly with increasing temperature. There seems to be a lingering effect at 10 K, although not nearly as pronounced as that at 4.2 K. Although a double peak is not distinguishable at 10 K the Fe surrounding an Fe anti-site atom spectra is clearly broadened by hyperfine splitting compared to the spectra at 300 K. Therefore, Bogner et al. find that there exists a localized magnetic state created by Fe anti-site defects. This state could cause an increase in the force constants surrounding the Fe anti-site defect. Their Mössbauer spectral analysis shows that this magnetic state occurs below 50 K, and the hyperfine splitting becomes significant between 20 K and 10 K.

This is a distinctly different phenomenon than that discussed in Chapter 5; although both give rise to a stiffening in the FeAl DOS, this stiffening is due to magnetic contraction that only arises at low temperatures and this is most likely affecting many dispersion directions.

The measured magnetic state of Fe anti-site atoms and their nearest neighbors could contribute to the anharmonicity seen in our data between 10 K and 300 K. A stiffening of the 10 K DOS due to the Fe anti-site defects would increase the anharmonicity between the two temperatures. Although we cannot be certain this as the cause for our measured anharmonicity, we can say that the evidence points toward Fe anti-site magnetic effects as a possible cause. This particular explanation would also account for the larger anharmonicity

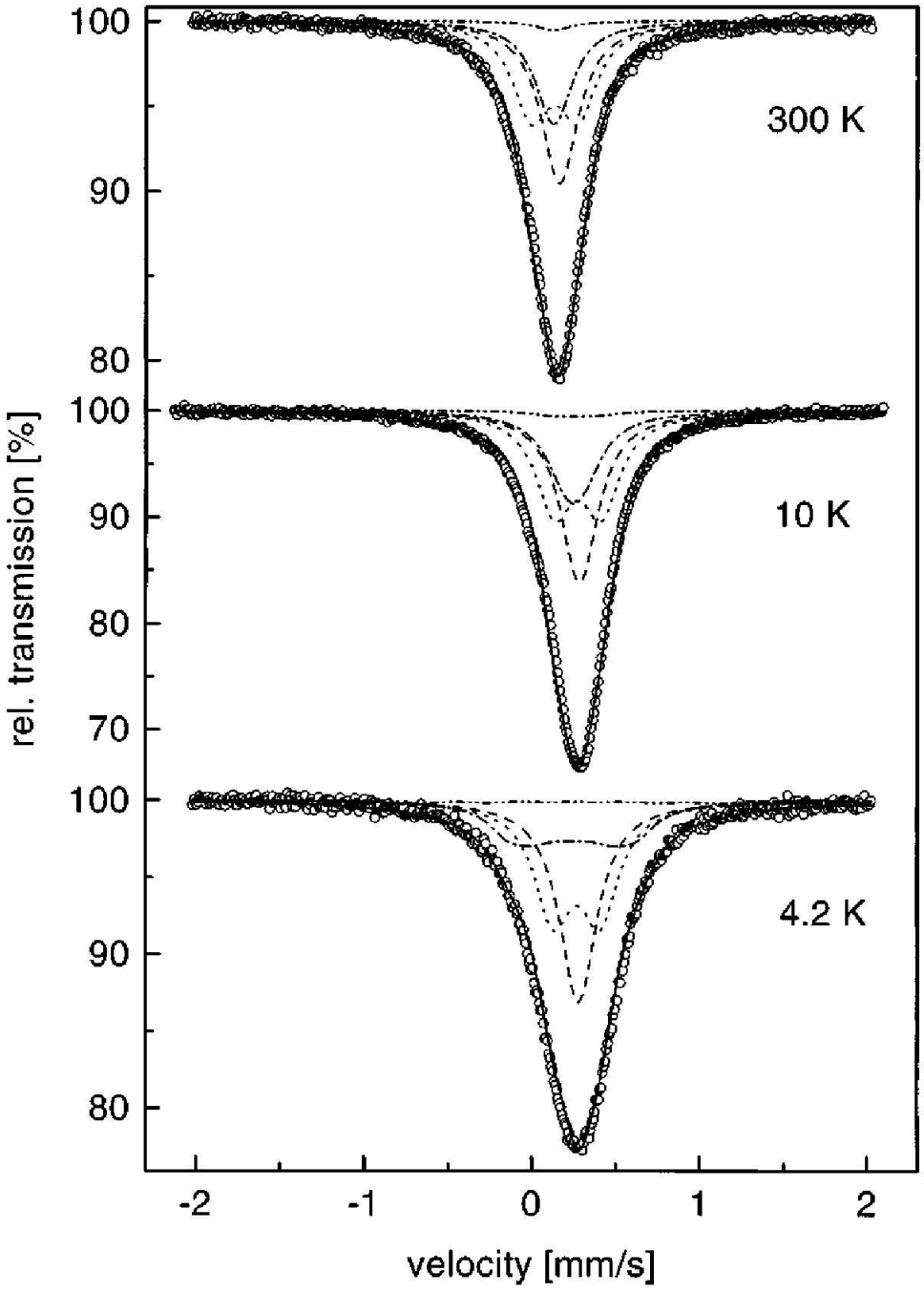

Figure 6.8: ^{57}Fe Mössbauer spectra recorded at different temperatures. Fe in ideally ordered B2 (dashed line), Fe around Fe vacancy (dotted line), corner atoms around Fe anti-site (dashed-dotted line), and Fe anti-site(dash-dot-dot line).[7]

seen in the sample with more vacancies because more vacancies correspond to more Fe anti-site atoms, and thus a larger stiffening at 10 K.

Opposite to the low temperature behavior, between 300 K and 973 K the DOS stiffens with temperature. This stiffening overwhelms any softening of the DOS due to lattice expansion. The vibrational entropy per vacancy was measured to be -0.75 k_B, large and negative, in Chapter 5. At higher temperatures the equilibrium concentrations of both mono- and di-vacancies will increase causing a increasing stiffening in the DOS. Notice that the characteristics of the stiffening in the in-situ data is extremely similar to that of the quenched data in Chapter 5. The low energy acoustic modes stiffen, states appear in the gap, and the high energy optical modes increase in cutoff energy. It is possible that at higher temperatures the vacancy concentration is large enough to counterbalance any softening that would have occurred by the expansion of the lattice.

6.5 Conclusions

We measured the anharmonic vibrational entropy of B2 FeAl at 300 K, 973 K, and 1323 K w.r.t. 10 K. It was found that FeAl has very odd anharmonic behavior, principally an anomalously large anharmonic entropy at 300 K, which becomes anomalously small at 973 K and 1323 K.

A possible explanation for measured anomalous anharmonicities has been given using known point defects within the system. At low temperatures, it was shown that localized magnetic moments of the Fe anti-site defect along with its eight neighbors could cause an extra stiffening of the 10 K DOS, causing a larger than expected anharmonic entropy at 300 K. Above 300 K it is possible that the thermal vacancies are causing a stiffening in the DOS, therefore suppressing the anharmonic vibrational entropy below what would be expected from lattice expansion alone.

It is also possible that the system has electron-phonon or phonon-phonon coupling, which could contribute to the anharmonicities. This direction would be appropriate to pursue in the future.

Chapter 7

Harmonic and Anharmonic Vibrational Entropy in Al-Ag Alloys

7.1 Introduction

The existence of large anharmonicity in elemental aluminum has been known for a long time now. Although the vibrational density of states of Al has not been measured at high temperatures, measurements of the Debye-Waller factor with temperature have been performed.[45, 1, 18, 43, 55] More recently, there have been computational efforts to corroborate the experimental large anharmonicity by calculating the Debye-Waller factor with temperature[64] and the heat capacity as a function of temperature[21]. However the anharmonicity of Al-Ag alloys has not been studied. In this work we measured the anharmonicity of $Al_{0.93}Ag_{0.07}$ and $Al_{0.40}Ag_{0.60}$. The Al-Ag phase diagram is shown in Fig. 7.1[44]

In-band resonance modes of heavy impurities have been been studied theoretically and measured previously.[20, 42, 6, 71, 28] These are quasi-localized vibrations of a heavy impurity atom in a matrix of light atoms. "In-band" is used to describe the case of heavy impurities, as the resonant mode energies are located *within* the allowable normal mode energies of a crystal made of purely matrix atoms. Unlike normal mode vibrations, the resonance modes decay with a finite lifetime into normal modes. The resonance modes peak in the DOS near a resonant frequency, and comprise large amplitude vibrations of the impurity with its interacting neighbors. The intensity of the DOS resonance peak directly corresponds to the impurity concentration.

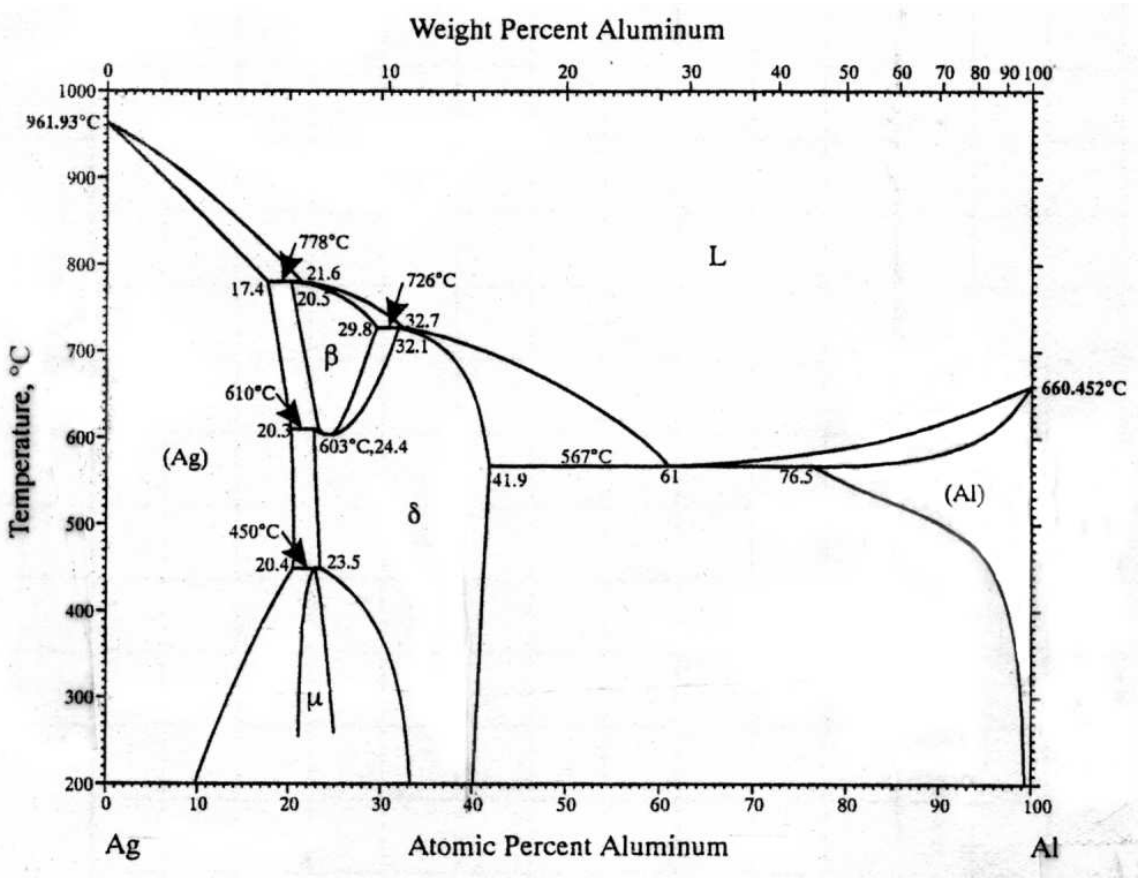

Figure 7.1: Al-Ag phase diagram.[44]

Previously, measurements of the low temperature heat capacity have been utilized to measure the resonance modes in $Al_{0.995}Ag_{0.005}$ and $Al_{0.9905}Ag_{0.0095}$. [71, 28] Both groups were able to measure the central energy of the resonant peak for very dilute Ag in Al.

We have measured the vibrational DOS for $Al_{0.93}Ag_{0.07}$ and $Al_{0.40}Ag_{0.60}$ at room temperature and at 520 °C along with elemental Al at room temperature. Between room temperature and 520 °C we measured a large anharmonicity in both alloys. We also measured a large resonance peak in the room temperature $Al_{0.93}Ag_{0.07}$. We compare our measured peak position with that of Tiwari et al.[71] and Hartmann et al.[28]

7.2 Experimental Methods

$Al_{1-\chi}Ag_{\chi}$ binary alloys with $\chi = 0, 0.07, 0.60$ were prepared by arc-melting under an argon atmosphere, using shots of 99.99% Al and 99.99% Ag. There was negligible mass loss and little visible surface oxidation after melting, so the compositions are expected to be accurate to 0.1 at.%. The ingots were cold-rolled to thicknesses optimizing to scatter 10% of the incident neutrons. The rolled strips were heated to 823 K, and quenched into iced brine to prepare disordered solid solutions.

X-ray diffraction patterns were acquired from all samples using an Inel CPS-120 diffractometer with Co Kα radiation and a position-sensitive detector. These data confirmed that the crystal structure was face-centered cubic (fcc), with no evidence of second phases or obvious compositional non-homogeneity.

Time-of-flight inelastic neutron scattering data were acquired with the LRMECS instrument at the Intense Pulsed Neutron Source at Argonne National Laboratory. Samples were mounted in thin-wall aluminum cans, 7 cm×10 cm, using an incident beam of monochromatic neutrons with an energy of 60 meV. The pure Al and the $Al_{0.93}Ag_{0.07}$ samples were also measured with an incident energy of 35 meV. The flat sample packages were tilted at a 45 °angle off the direction of the incident beam to minimize self-shielding. All spectra were measured at room temperature. Background data were acquired from the empty aluminum cans under the same conditions.

The raw data of intensity versus time-of-flight in the different detector tubes were reprocessed into intensity versus energy, and then converted into an approximate, or "neutron-

weighted" phonon density-of-states using the following steps. The raw data were corrected for detector efficiency using a white beam spectrum from a vanadium plate, and normalized by the incident flux on the samples. The time-independent background was removed. The time-dependent parts of the background acquired from the empty cans were then subtracted. Detector data were re-binned into angular bins of 10 °in width, using scattering angles up to 120 °. The low-angle data (angles less than approximately 35 °) were neglected owing to weak phonon scattering. After subtraction of an elastic peak centered about 0 meV, the data below approximately 5 meV were approximated as a straight line, as expected in the continuum limit. Corrections were then made for thermal factors and multiphonon scattering (two- through five-phonon processes), using an iterative procedure in the incoherent approximation. [5] The error in the resulting phonon density-of-states (DOS) due to neutron-weighting [5] is negligible as the ratio of phonon scattering of Ag:Al is 0.8, almost 1.

7.3 Results

7.3.1 Inelastic Neutron Scattering

The resulting DOS curves for $Al_{0.93}Ag_{0.07}$ and $Al_{0.40}Ag_{0.60}$ at room temperature and 520 °C are shown in Figs. 7.2 and 7.3, respectively. Both samples show a very large softening between 20 °C and 520 °C. In the case of $Al_{0.40}Ag_{0.60}$, all modes shift to lower energies. The cutoff energy decreases by approximately 2 meV. Similarly, the low-energy Debye region where the DOS is parabolic shifts by 1 meV to lower energies. A large number of modes shift from higher energies to energies between 10 meV and 18 meV. The softening of $Al_{0.93}Ag_{0.07}$ does not exhibit a large change in the cutoff energy of its DOS. However, there is a very large shift of modes into energies from 0 meV through 20 meV. We will show later that this is the same energy region as the Ag resonance peak. This may or may not be truly the changes in the resonance peak with temperature, however.

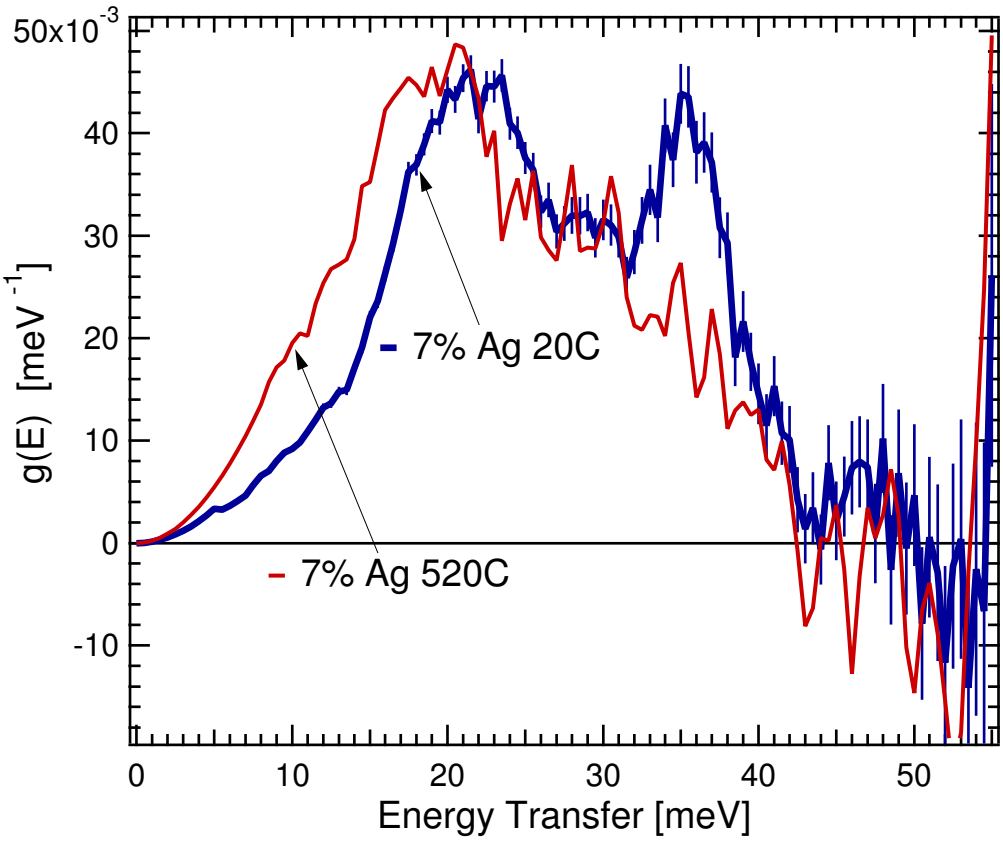

Figure 7.2: Anharmonic softening is seen between 20 and 520 in the vibrational density of states of $Al_{0.93}Ag_{0.07}$.

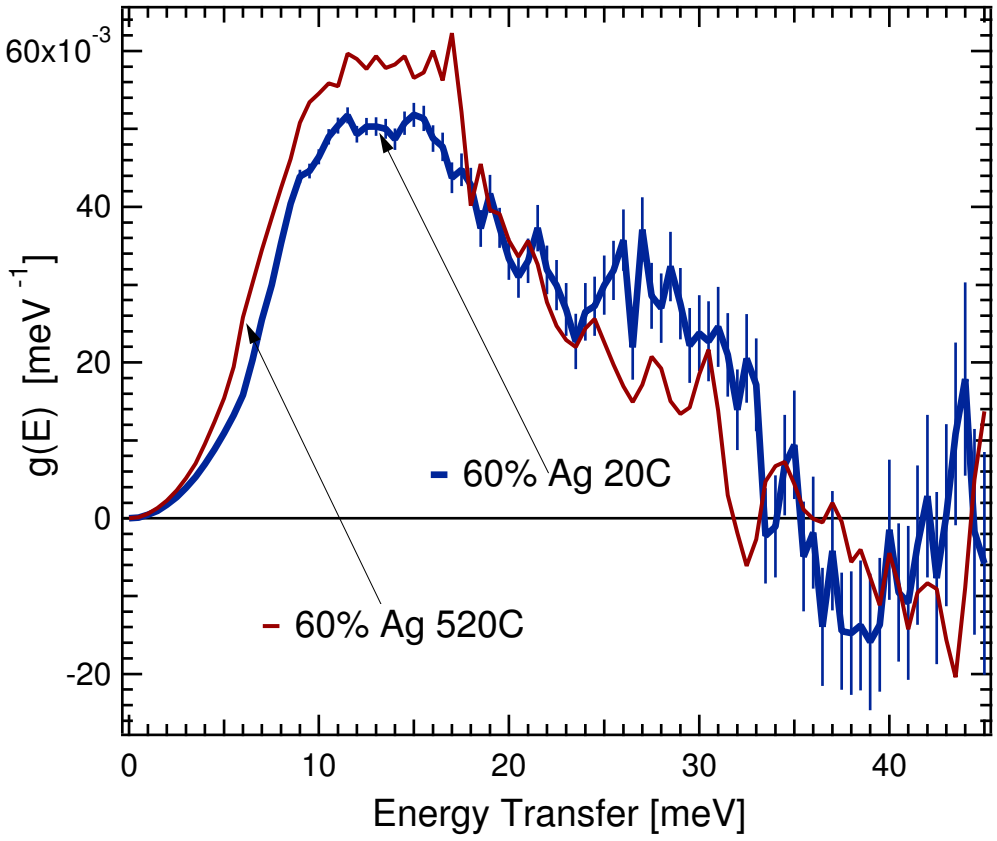

Figure 7.3: Anharmonic softening is seen between 20 and 520 in the vibrational density of states of $Al_{0.40}Ag_{0.60}$.

7.3.2 Anharmonic Entropy

The anharmonic entropy between temperatures 20 °C and 520 °C was determined for both alloys using Eq. 3.18. The results are plotted in Fig. 7.4. Also plotted in this graph is the calculated entropy required for lattice expansion using measured values of the bulk modulus, coefficient of lattice expansion, and density for each alloy, Eq. 3.19. Notice that there is a large discrepancy between this lattice expansion contribution and the total for $Al_{0.40}Ag_{0.60}$. The difference between the two is what we call the "anomalous anharmonic vibrational entropy," which comes from exotic phenomena. The origin of this extra entropy could arise from electron-phonon or phonon-phonon coupling, unknown processes. This is the first measurement of the anharmonicity of this alloy. Although exciting, the repercussions are that there are no supportive experiments to investigate its origins. More experiments and/or calculations will be necessary to gain insight into the cause of this extremely large anharmonicity. On the other hand, the anharmonic vibrational entropy of $Al_{0.93}Ag_{0.07}$, although large, has no anomalous contributions to it. We see from Fig. 7.4 that it is fully explained by lattice expansion.

7.4 Discussion

7.4.1 Resonance Modes

A large resonance peak was measured in the dilute Ag sample, $Al_{0.93}Ag_{0.07}$. The peak is readily seen by comparing the $Al_{0.93}Ag_{0.07}$ DOS with the Al DOS, Fig. 7.5.

Although it proves to be a minor correction, due to its simplicity in this particular instance, a neutron-weight correction was performed for $Al_{0.93}Ag_{0.07}$ at room temperature. This was done by assuming that the Al PDOS in $Al_{0.93}Ag_{0.07}$ is the DOS of pure Al, a very good approximation at such low concentrations of Ag, particularly as the Ag produces resonance modes. The correction is then straightforward using Eq. 3.10; be sure to notice that the PDOS for each element is weighted by their concentrations in the alloy. Therefore, the resonance peak is extracted from the $Al_{0.93}Ag_{0.07}$ NWDOS by subtracting 93% of the Al normalized DOS. This peak must then be de-weighted by the ratio of σ/M for the binary alloy elements leaving the resonance peak that is only weighted by the composition

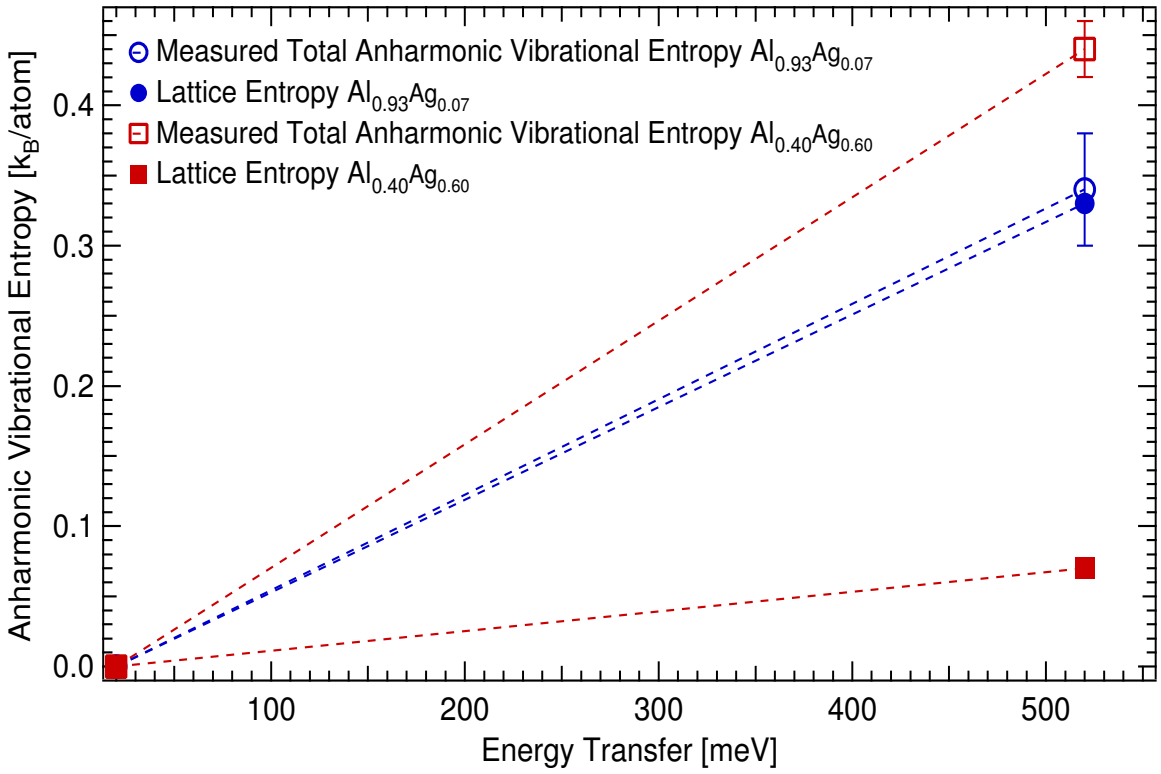

Figure 7.4: The anharmonic entropy due to lattice expansion is not large enough to account for the total anharmonic vibrational entropy of $Al_{0.40}Ag_{0.60}$, but is successful for $Al_{0.93}Ag_{0.07}$.

of the alloy and is shown in Fig. 7.5. The composition weighted peak (Ag PDOS) is then added back to the composition weighted Al PDOS to finalize the neutron-weight correction resulting in the $Al_{0.93}Ag_{0.07}$ DOS. The 35 meV incident DOS was neutron-weight corrected by using the integral of the 60 meV incident neutron-weight corrected DOS for Al and $Al_{0.93}Ag_{0.07}$ from 0 meV to 17 meV.

The DOS obtained with 35 meV incident energy (See Fig. 7.6) has better energy resolution than the DOS for 60 meV incident energy. The vibrational entropy of mixing Ag in Al was measured to be $0.03k_B/atom$ using Eq. 3.12 to calculate the difference between the alloy and a sum of the elemental DOS weighted by concentration. The small vibrational entropy of mixing is not entirely surprising because the Ag DOS is at energy levels very similar to that of the resonance modes.

The resonance peak position was found by fitting the Ag partial DOS with a Gaussian function. Although the peak is not exactly a Gaussian, in principle once instrumental resolution is convolved with the peak the Gaussian function is a reasonable estimate, as seen in Fig. 7.5. The Gaussian fit gives a peak position of 11.0 ± 0.1 meV, a FWHM of 8.0 ± 0.2 meV, and an amplitude of $2.94x10^{-3} \pm 7x10^{-5}$ meV^{-1}.

Calculations of the specific heat on $Al_{0.995}Ag_{0.005}$ and $Al_{0.9905}Ag_{0.0095}$ have been used to measure characteristics of the resonance modes in this system.[71] At low temperatures the specific heat has appreciable contributions from low-frequency resonance modes. By measuring the specific heat it is therefore possible to measure the positions of the resonance peak. Assuming an isotopic defect (i.e., the Ag-Al force constant is assumed to be that of Al-Al) the resonance peak position has been calculated to be $\omega_r/\omega_m = 0.29$ [71] and $\omega_r/\omega_m = 0.28$,[28] where ω_r is the frequency of the resonance peak and ω_m is the cutoff frequency of the DOS. Using a cutoff energy value of 43 meV and $\omega_r/\omega_m = 0.28$, we find that ω_r is predicted to be 12 meV. The value of 12 meV is consistent with our measured value of 11 meV.

It is most probable that the resonance peak changes its characteristics with temperature. Unfortunately, no experimental or theoretical work has investigated the temperature effects on the resonance peak. We are therefore left to conjecture about the possible changes that may occur with an increase in temperature.

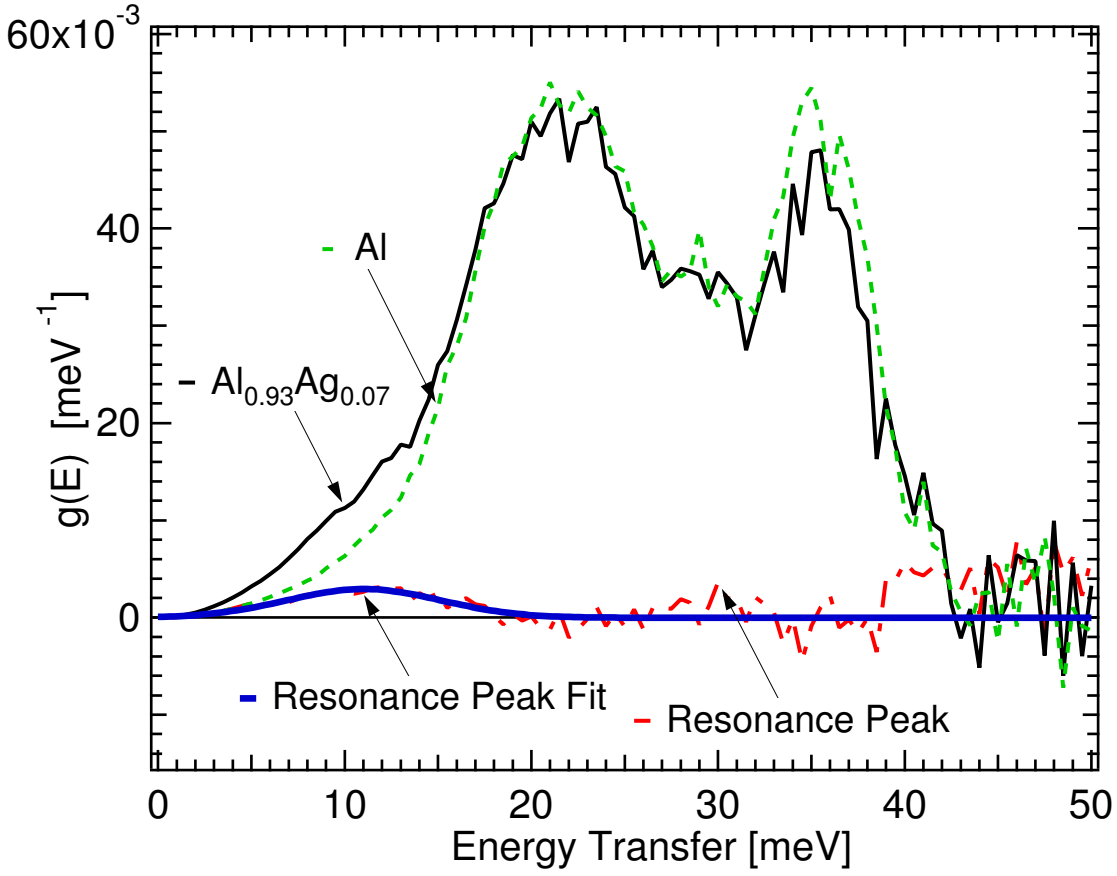

Figure 7.5: An extremely large resonant peak exists at approximately 11meV. Although a small correction, this data has been neutron-weight corrected.

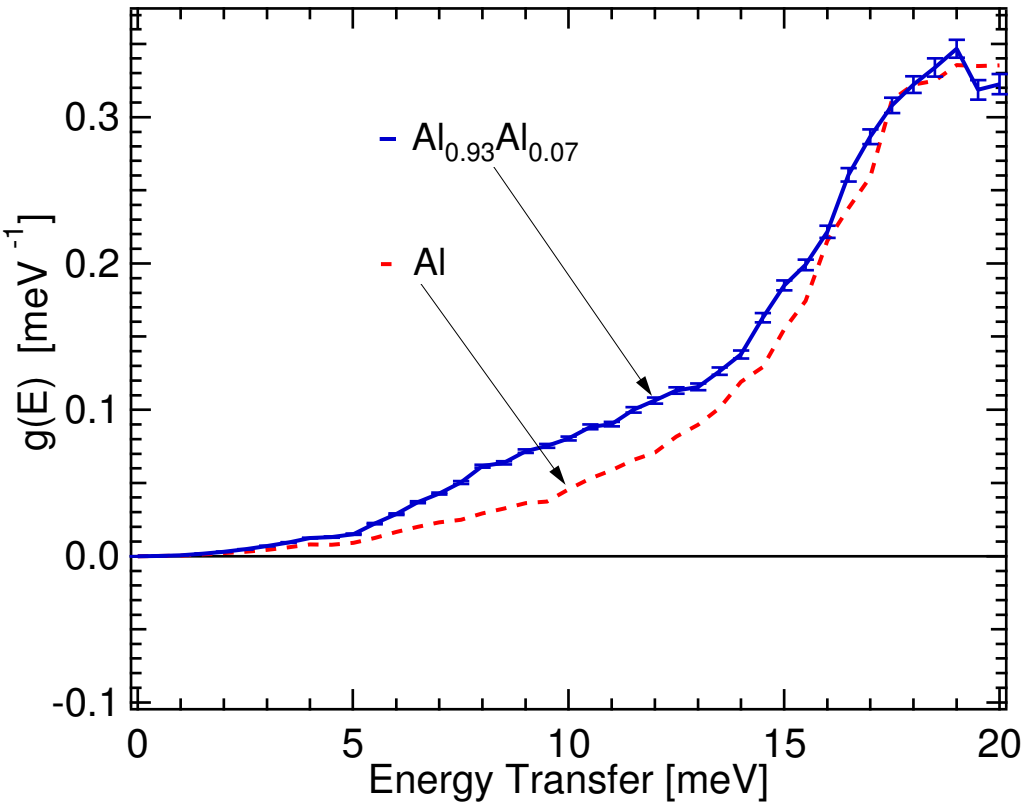

Figure 7.6: An extremely large resonance peak exists at approximately 11meV. Although a small correction, these data have been neutron-weight corrected utilizing the 60 meV DOS.

7.4.2 Resonance Modes and Ag Solubility at High Temperatures

By now it is obvious that the anharmonicity of a system is far from easy to predict. However, there is one anharmonic contribution that is predictable–the change in vibrations due to the expansion or contraction of the lattice with temperature change. If no other anharmonic forces are at work, the typical lattice expands with an increase in temperature and the DOS shifts to lower energies. This shift in energies corresponds to a softening of the force constants in the system. Therefore, to investigate changes in the resonance peak with increasing temperature for $Al_{0.93}Ag_{0.07}$ we considered how the resonance peak changed as we varied the force constants using an impurity defect dynamical theory that uses a Green's function technique.[42, 26] Using these theories, derivations of the partial density of states of the impurity (or resonance peak) utilizing the host atom DOS have been performed.[39, 41, 40, 20, 26, 61]

The largest effect of isolated impurities is on nearest-neighbor forces in the host-lattice. By utilizing this short-range nature of the impurity perturbation to the host lattice, the Green's function technique is able to work in the "site representation." The technique is therefore used on the nearest-neighbor cluster force constants and the pure lattice Green's function enabling closed expressions for all necessary dynamical quantities of the perturbed lattice.

By using the measured Al DOS, the mass ratio of Al:Ag, and the force constant ratio of Al-Al bonds to Al-Ag bonds, we can calculate the resonance peak of dilute Ag in Al using the Green's function method that was developed by Mannheim, et al.[39, 41, 40] There is only one free parameter in this calculation, which is the ratio of the host-host force constant to the impurity-host force constant or A/A'. The modified DOS which includes the impurity modes is given by

$$G'(\omega) = \Big(\frac{M}{M'}\Big)G(\omega)\Big\{[1+\rho(\omega)S(\omega)]^2 + \Big[\Big(\frac{\pi}{2}\Big)\omega\ G(\omega)\rho(\omega)\Big]^2\Big\}^{-1} \tag{7.1}$$

$$+\,\delta(\omega-\omega_L)\frac{M}{M'}\times\Big\{\rho^2(\omega)T(\omega)+\frac{M}{M'}-\Big[1+\rho(\omega)\Big]^2\Big\}^{-1}\quad,$$

where

$$\rho(\omega) = \Big(\frac{M}{M'}\Big) - 1 + \omega^2\Big[1 - \frac{A}{A'}\Big]/\mu(+2) \quad , \tag{7.2}$$

$$S(\omega) = P\int_0^\infty \omega'^2(\omega'^2 - \omega^2)^{-1}G(\omega')d\omega' \quad , \tag{7.3}$$

$$T(\omega) = \omega^4\int_0^\infty (\omega'^2 - \omega^2)^{-2}G(\omega')d\omega' \quad , \tag{7.4}$$

$$\mu(n) = \int_0^\infty \omega^n G(\omega)d\omega \quad , \tag{7.5}$$

ω_L is a localized mode frequency that exists if $1+\rho(\omega_l)S(\omega_L) = 0$ and $\omega_L > \omega_m ax$, δ is the Dirac δ function and P stands for the principal value. The DOS of the pure host crystal is $G(\omega)$. This calculation is described in detail in the paper by Seto et al. [61] As our impurity modes are resonance modes $\omega_L = 0$.

In this way, using the measured Al DOS and the known mass ratio of Al to Ag, we have calculated the resonant peak with a variety of force constant ratios (A/A'): 1:0.5, 1:1, 1:2, 1:3, and 1:5 where the ratio is (Al-Al):(Al-Ag). Figure 7.7 gives the results of these calculations that are labeled by the A' value. The resonance peak softens, increases in amplitude and decreases in width as force constant ratio decreases corresponding to temperature increase.

It was shown in Section 7.3.2 that for $Al_{0.93}Ag_{0.07}$ the total anharmonic vibrational entropy between temperatures 20 °C and 520 °C was fully accounted for by the entropy required to expand the lattice. According to the Mannheim impurity method it would be quite reasonable for the resonance peak to soften and become sharper with increasing temperature. How will the temperature dependence of the resonance peak affect the anharmonicity of the alloy?

Let us assume that the $r_{FC} = 4$ resonance peak is the Ag PDOS for Ag impurities in RT. This is consistent with a resonance peak position of 11 meV like that measured in our DOS. The resonance peak at 520 °C is less clear, but looking at our measured 520 °C DOS for $Al_{0.93}Ag_{0.07}$, the peak could be as low as 8 meV. We estimate that the resonance peak for $r_{FC} = 0.8$ is a good approximation for the Ag PDOS at 520 °C. We can now measure the anharmonic vibrational entropy between 520 °C and 20 °C for any Ag concentration in Al for which there is a resonance peak. It is reasonable to assume that the resonance peak

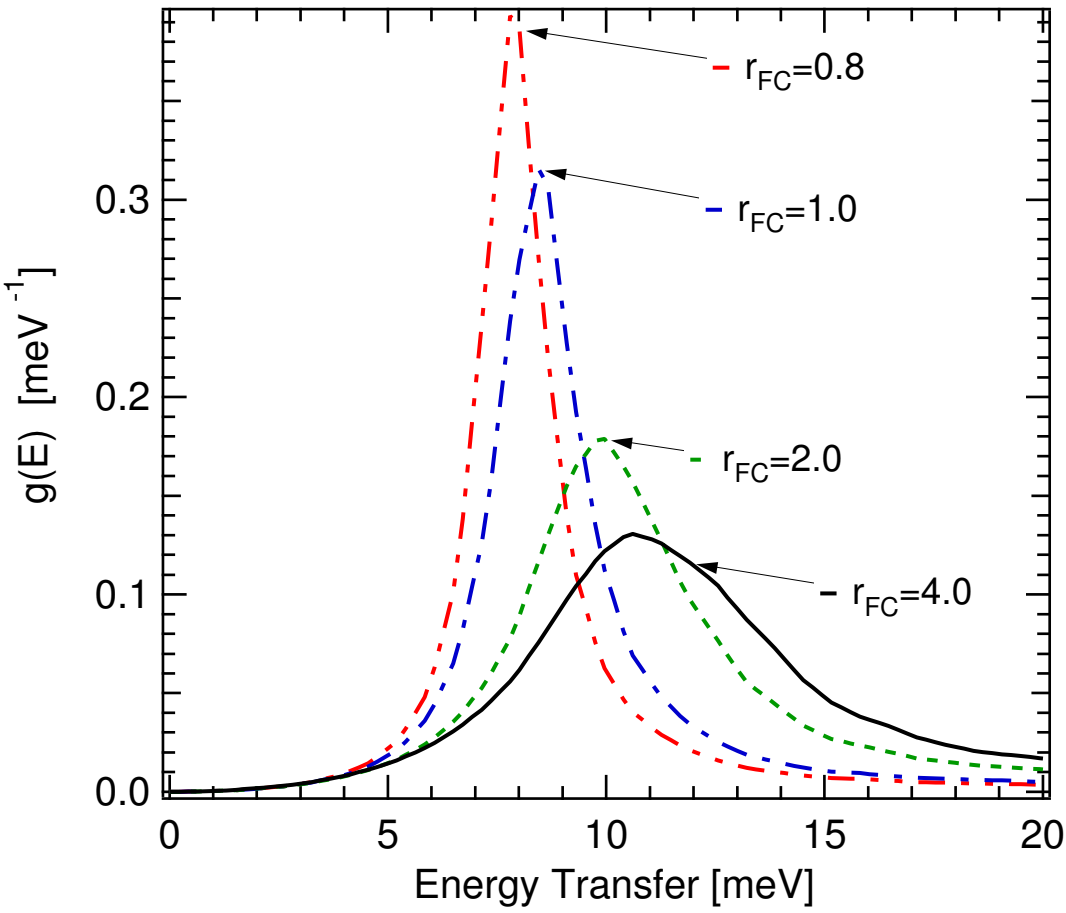

Figure 7.7: Calculated resonant peaks of Ag in Al using the Mannheim impurity method.[39, 41, 40, 26, 61] The curves are labeled according to A', the Al-Ag force constant, $A = 1$ and is the magnitude of the Al-Al force constant.

exists for concentrations of Ag from 0% to at least 20%. It is important to note that the anharmonic vibrational entropy between T_1 and T_2 can be calculated as

$$S^{Anh}_{(T_2-T_1)} = \chi_{Al} S^{Anh}_{Al} + \chi_{Ag} S^{Anh}_{Ag} \ , \tag{7.6}$$

where χ_{Al} and χ_{Ag} are the concentration of Al and Ag, and S^{Anh}_{Al} and S^{Anh}_{Ag} are the anharmonic vibrational entropy of the Al and Ag PDOS between T_1 and T_2. S^{Anh}_{Ag} can be calculated using the peaks in Fig. 7.7 and Eq. 3.18, the result being 1.0 $k_B/atom$. This is quite large. Once we weight it by the concentration of Ag, 0.07, we find that the Ag PDOS contribution to $S^{Anh}_{(T_2-T_1)}$ is only 0.07 $k_B/atom$. Our measured $S^{Anh}_{(T_2-T_1)}$ was 0.34 $k_B/atom$, leaving the $\chi_{Al} S^{Anh}_{Al}$ to be 0.27 $k_B/atom$ and therefore $S^{Anh}_{Al} = 0.29 k_B/atom$. Thus we see that for $\chi_{Ag} = 0.07$ the resonance peak has a very small effect on the thermodynamics of the system. The temperature dependence of the DOS should behave much like Al in this case. Previous publications have offered conflicting information on whether or not Al has anharmonicities that are larger than those of the quasi-harmonic model (i.e., larger than those expected by lattice expansion). Some have calculated that the anharmonicities of measured Debye-Waller factors are much larger than that expected by lattice expansion.[43, 64] However, Pathak et al.[55] have calculated that their measured anharmonic contribution to the Debye temperature is derived totally from the thermal expansion of the crystal up to about 800 K. Our measurement of $Al_{0.93}Ag_{0.07}$ is therefore in agreement with Pathak et al.

We use the above calculated values to calculate the anharmonic vibrational entropy for an alloy of Al-20 at. % Ag instead of our measured Al-7 at. % Ag. It is reasonable to assume that the larger concentration of Ag will not affect the resonance modes or the PDOS of Al. Therefore we keep the values calculated above for S^{Anh}_{Al} and S^{Anh}_{Ag}. Using $S^{Anh}_{Al} = 0.29 k_B/atom$ and $S^{Anh}_{Ag} = 1.0 k_B/atom$ we find that $S^{Anh}_{(T_2-T_1)} = 0.43 k_B/atom$ using Eq. 7.6 with $\chi_{Al} = 0.80$ and $\chi_{Ag} = 0.20$. The anharmonic entropy due to lattice expansion should be the same (if not smaller with more Ag concentration, as the bulk modulus of Ag is much smaller than that of Al) so that $S^{Anh}_{Latt} \leq 0.33 k_B/atom$. This means that for $Al_{0.80}Ag_{0.20}$ there could be an anomalous anharmonic vibrational entropy of greater than or equal to 0.1 $k_B/atom$. The vibrational entropy could be a significant contribution in an explanation for the large solubility of Ag in Al at high temperatures seen in the phase

diagram, Fig. 7.1.

7.5 Conclusions

Inelastic neutron scattering spectra were measured on $Al_{0.93}Ag_{0.07}$ and $Al_{0.40}Ag_{0.60}$ at 20 °C and at 520 °C; a sample of pure Al was also measured at 20 °C.

A large softening in the DOS of both alloys was measured. The softening of $Al_{0.40}Ag_{0.60}$ was anomalously larger than that expected by simple lattice softening. Causes for this anharmonicity may be phonon-phonon or phonon-electron coupling. The softening of the DOS of $Al_{0.93}Ag_{0.07}$, although quite large, is explained within experimental error by lattice expansion.

A large resonance peak was measured at 20 °C in the DOS of $Al_{0.93}Ag_{0.07}$. It was shown that the resonance peak is expected to soften as temperature increases according to the Mannheim method. At 7% Ag, the softening of the resonant peak, although perhaps large, would not have any significant thermodynamic impact because the partial Ag anharmonic entropy is weighted by the Ag concentration. However, at 20% Ag, the resonant peak, in accordance with the Mannheim method, will add at least 0.2 $k_B/atom$ to the anharmonic entropy between 20 °C and 520 °C. This would contribute to the increased Ag solubility in Al at high temperatures.

Chapter 8

Conclusions

8.1 Summary and Discussion

This thesis has explored both harmonic and anharmonic vibrational entropy of Fe- and Al-based binary alloys. We have considered how these vibrational entropies affect the phase stability of these systems. In many cases we have found unexpected behavior.

The vibrational entropy of spinodal decomposition was measured in Chapter 4 as –0.17 $\pm$ 0.01 $k_{\mathrm{B}}/atom$, nearly equal to that of configurational entropy! This is indeed a very large value for vibrational entropy. However, although this in and of itself is significant, what is needed to predict the critical temperature of decomposition using a Cahn-Hilliard model is the curvature of vibrational entropy with respect to Cr concentration. Historically, theoretical models of decomposition have not included vibrational entropy in the free energy calculation of the system. Although our measurement of the vibrational entropy of spinodal decomposition is related to the curvature of vibrational entropy w.r.t. the Cr concentration it is not possible to calculate that curvature with only the vibrational entropy of spinodal decomposition. Therefore, we analyzed previous phonon dispersion measurements of $Fe_{1-\chi}Cr\chi$ alloys in order to measure the curvature of the vibrational entropy of the alloy with respect to Cr concentration. With this curvature, and the curvature of configurational entropy w.r.t. Cr concentration within the point approximation, we showed that the critical temperature would decrease by at least 20% of its original value by the inclusion of vibrational entropy into the free energy calculation of the system. The reason that the decrease is a minimum value and not an exact value is that the model for configurational

entropy does not account for clustering within the solid solutions. A cluster model would reduce the configurational entropy at 50% Cr, which is its maximum point in Cr concentration, thereby reducing the curvature of the configurational entropy with Cr concentration. By showing that the critical temperature of spinodal decomposition is reduced by at least 20% of its previous value by including vibrational entropy in the free energy calculations, we have shown that by neglecting vibrational entropy a significant error is included in the calculation. More importantly, we show that vibrational entropy is a rather important contribution to the thermodynamics of spinodal decomposition in this system.

In Chapter 5, the vibrational effects of thermal vacancies in FeAl were measured for the first time using inelastic neutron scattering. The vacancies were found to cause a small stiffening of acoustic modes into the phonon gap in the DOS. Calculated dispersion curves showed that the (1 1 0) acoustic branch was clearly affected by the vacancies. The (1 1 0) direction is expected to be stiffened owing to the collapse of the lattice around the vacancies along with the stiff Fe-Al bond of the body-center anti-site Fe atom with its neighboring body-center Al atom. We measured the vibrational entropy of formation of vacancies to be –0.75 k_B/vac.

The density of states as a function of temperature of FeAl was measured in detail in Chapter 6. We found two distinctly different anharmonic behaviors:

1) Below room temperature, extra anharmonic softening of the DOS was observed, beyond that explained by lattice expansion.
2) Above room temperature, large anharmonic stiffening of the DOS was observed, keeping the DOS from softening as the lattice expands.

We give possible explanations for both phenomena. Local magnetic moments of anti-site Fe and their first nearest neighbors below 50 K could cause the 10 K density of states to be stiffened, in turn leading to an increased anharmonicity between that and 300 K. At temperatures above room temperature thermal vacancies increase in concentration. These vacancies contribute –0.75 k_B/vac by stiffening the density of states. This could ultimately counterbalance the softening of the density of states due to lattice expansion, causing a large anharmonic stiffening at high temperatures.

The density of states of Al-Ag alloys has been reported in Chapter 7, with some sur-

prising results. We found that there is an extraordinarily large anharmonic softening in $Al_{0.40}Ag_{0.60}$ beyond that of lattice expansion. A large resonance peak was measured in $Al_{0.93}Ag_{0.07}$ and was in good agreement with predictions. We also measured the anharmonic entropy of $Al_{0.93}Ag_{0.07}$ between 20 °C and 520 °C, and found that it is dominated by the Al partial density of states, which should behave mostly like bulk Al. We found that contrary to some calculations, the anharmonic vibrational entropy is described fully by the expansion of the crystal lattice.

Using the Mannheim impurity method, we were able to show that at larger concentrations of Ag the resonance peak in Al-Ag may have a much stronger thermodynamic importance. In fact it could very well be a large part of the reason for the measured increased solubility of Ag in Al at high temperatures.

8.2 Future Work

In many experiments the results are not only of interest but they ignite more questions to be answered. The results presented in this work leave many questions unanswered, and therefore suggest further investigation.

The magnitude of the vibrational entropy of spinodal decomposition in FeCr was unexpectedly large. The effects of the vibrational entropy on the critical temperature of spinodal decomposition was important. We are left questioning whether these findings are isolated to the Fe-Cr system, or whether they are a prevailing characteristic of all spinodal decomposition transformations? The answer to this question would be of great value to the materials science community. Therefore, this work should be pursued. A very good choice for the first system might be Al-Zn. Not only is it a binary alloy, which is much simpler to model numerically if necessary, but also, the neutron scattering weight ratio of the two elements is 0.88–almost 1! This makes a neutron-weight correction unnecessary, which greatly simplifies data reduction. Other systems would be possible, but they would require mixing isotopes to remove the need for a neutron-weight correction. Isotopes are a much more expensive route, and are best left as a last resort.

FeAl has shown extremely unexpected results. We found that defects can have large thermodynamic effects in FeAl, in terms of both vacancy formation and anharmonic phe-

nomena. It is interesting that defects can have such large anharmonic consequences. At low temperatures, we found that the disruption of a paramagnetic state (by removing the atomic order of the crystal and creating a local magnetic moment) has a great effect on the vibrational density of states. It may prove interesting to search for other systems that have similar consequences. Furthermore, measurements of phonon-phonon and electron-phonon coupling would be important to perform on this system. If there is electron-phonon coupling, either point contact spectroscopy or a measurement of the temperature dependence of the electronic density of states would provide evidence for it. Measurements of phonon line-shifts and line-widths by either inelastic neutron scattering or raman spectroscopy can be used in conjunction with theory to measure phonon-phonon coupling phenomena. These measurements could provide invaluable explanations for the measured anharmonicities in this alloy and in $Al_{0.40}Ag_{0.60}$, which had large anharmonicities. Future experiments for both alloys to explore phonon-phonon and electron-phonon coupling contributions to their anharmonic entropy would be a reasonable course of action.

The findings from our investigation on $Al_{0.93}Ag_{0.07}$ leave a gaping hole in current experimental measurements that needs to be filled in order to formulate a final conclusion. Measurements of Al-Ag with larger concentrations of Ag, ideally up to 17 atomic % Ag measured at 550 °C, are necessary to finalize the work on the thermodynamic effects of the resonance modes. It would also be necessary to measure the Al density of states at 550 °C to extract the resonant peak from the alloy data. Once these experiments have been performed, we will know whether the resonant peak has thermodynamic importance at high temperatures.

Experiments not only require insightful theoretical background but also adequate experimental apparatus. The majority of our research has been moving toward in-situ inelastic neutron scattering measurements. There is a great deal to be learned about anharmonicities, but this requires measurements to be performed in-situ. Currently, the furnaces available for our use are extremely inefficient. They have been designed specifically for diffraction measurements. These measurements, of course, use elastic neutron scattering. Elastic scattering experiments use samples that are approximately 1/10 the mass of inelastic samples because elastic neutron flux is very large compared to inelastic flux. When we use a dif-

fraction furnace, we are forced by the geometry of the furnace to use samples with 1/10 the mass of what is appropriate to utilize the full incident beam cross-section. The furnaces are designed with a much smaller beam cross-section in mind, therefore in an inelastic instrument there is a great deal of furnace that is directly in the neutron beam, significantly adding to the background-to-signal ratio. An appropriate step for future experimental success is to design a new furnace that is optimized for inelastic chopper spectrometers. This is something, I am pleased to say, that our research group is currently endeavoring to achieve.

Appendix A

Simple Introduction to Spinodal Decomposition in a Binary Alloy

Spinodal decomposition is a unique occurrence. The process takes place in a binary alloy when the system, which is originally in a random solid solution (i.e., all atoms have equal probability of being located at all lattice points), segregates into two regions with distinctly different alloy concentrations. Unlike other more typical phase transitions the crystal structure does not change during the transformation. Since the crystal structure is the same for both phases, the free energy will be a single curve instead of two different curves (one for each crystal structure). In the case of FeCr, upon reaching equilibrium the spinodally decomposed regions will be $Fe_{0.90}Cr_{0.10}$ and $Fe_{0.10}Cr_{0.90}$. All stages are on a bcc lattice, but not all alloys segregate to such compositional extremes. The solid solution is at equilibrium at high temperatures, and below the critical temperature the system will decompose. The kinetics for this decomposition is very slow in FeCr. Even after one month at 500 °C the system will not have reached equilibrium.

Spinodal decomposition begins with infinitesimal compositional fluctuations throughout the sample that increase over time. Figure A.1 shows how the composition of Cr would change in a hypothetical FeCr alloy. Early in the decomposition process a sinusoidal wave is not a bad approximation. The variation in composition is plotted as a a function of cross-sectional distance in the sample. As time increases ($t_0 < t_1 < t_2$), the segregation of the sample increases. At t_0 the alloy is a random solid solution of $Fe_0.50Cr_0.50$.

We can consider a simple Cahn-Hilliard-type model for spinodal decomposition. In this

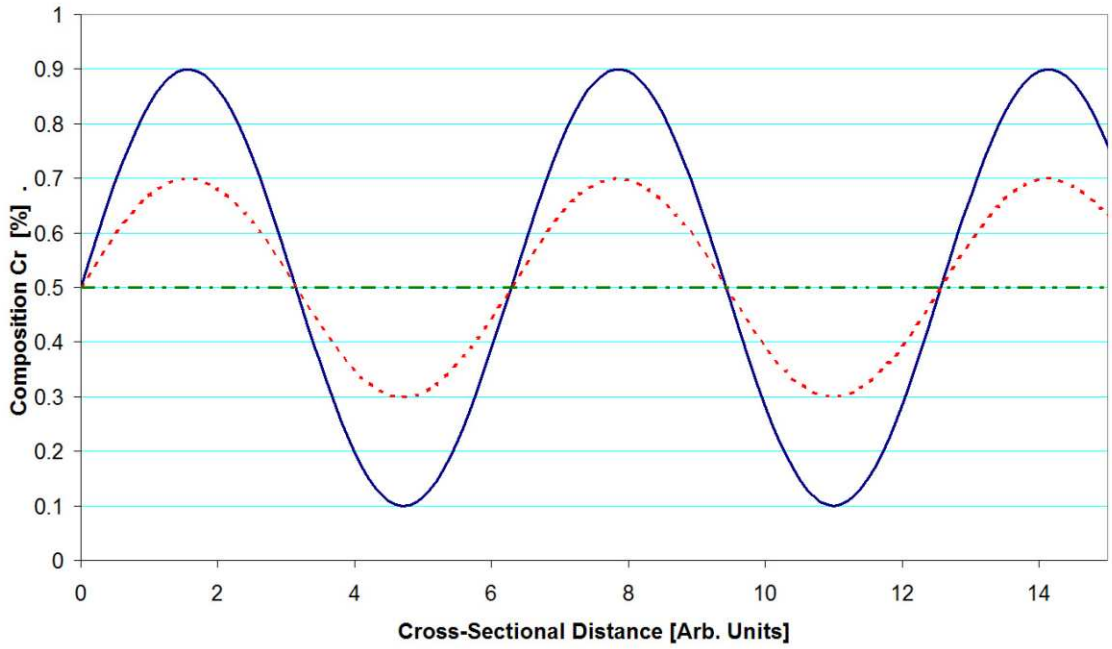

Figure A.1: Compositional fluctuations as a function of aging time in a hypothetical FeCr alloy. The dash-dot-dot line is at t_0, the dash-dot line is at t_1, and the solid line is at t_2.

model the cause for the separation into two phases comes from an energetic instability in the free energy of the crystal when the free energy has negative curvature. Let's calculate the free energy and see what happens in the case of spinodal decomposition.

We know that $\Delta G = \Delta H - T\Delta S$, so we will need to calculate the enthalpy, H, and the entropy, S. To calculate the enthalpy we will use the simple quasi-chemical model for the enthalpy of mixing, where

$$\Delta H_{Mix}^{QCM} = \Omega \chi_A \chi_B \ . \tag{A.1}$$

If $\Omega > 0$ then the possibility of chemical un-mixing exists because energetically like-atoms bonds (A-A or B-B) are preferred over mixed atom bonds (A-B). We will use the point approximation, Eq. 1.2, for the configurational entropy of mixing, ΔS. We can now calculate ΔG and observe how each term contributes to the shape of the free energy curve. Using our theory for FeCr as an example, Fig. A.2 plots ΔH, $-T\Delta S$, and the resulting ΔG. The ΔH term is minimized at the pure concentrations of Fe and Cr; this is an essential characteristic for spinodal decomposition to occur. The $-T\Delta S$ term is minimized at the

random solid solution of $Fe_0.50Cr_0.50$; it prefers a mixed state. Because the entropy curve is approximately the same magnitude as the enthalpy term but is wider in shape, the free energy has double minima. Both minimum positions are energetically equally favorable in this simple case. Therefore the equilibrium state will be segregated into two phases differing only in composition, one with 10 at. % Cr, the other with 90 at. % Cr.

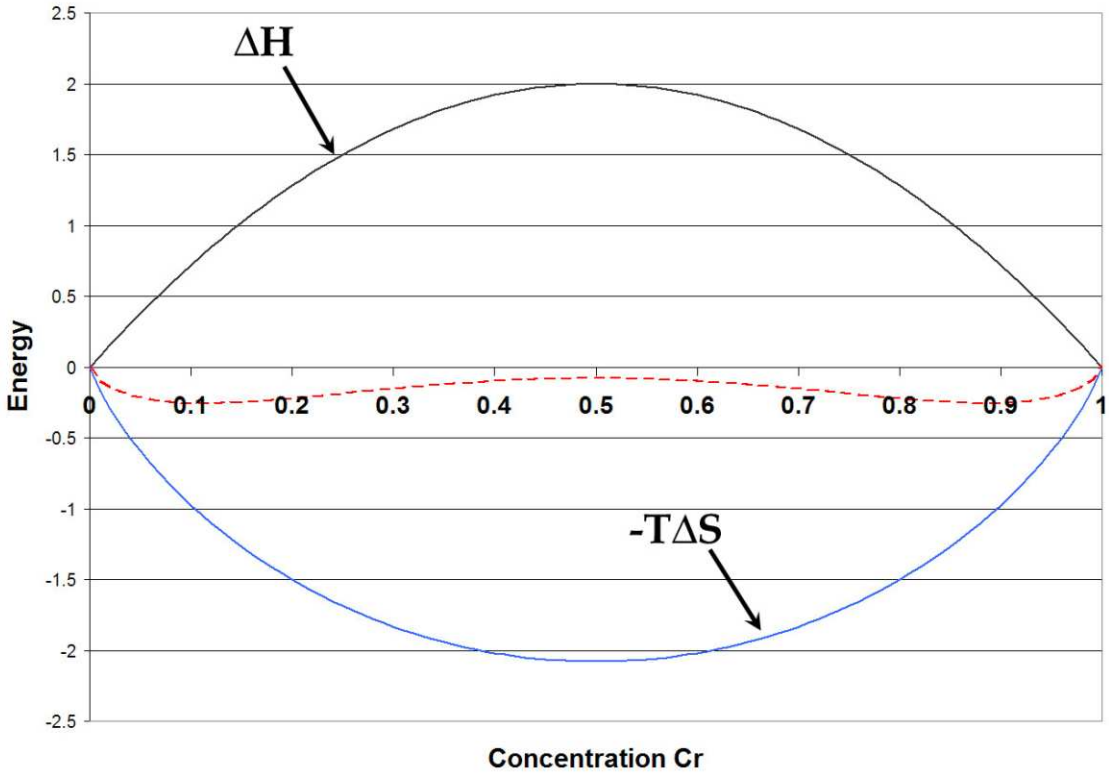

Figure A.2: The free energy of a spinodal system and its component terms. The individual terms of the free energy are labeled, the dashed line is the resulting free energy. In this temperature range the free energy has double minima, and will be spinodally decomposed at equilibrium.

Figure A.2 is plotted at a low temperature where spinodal decomposition is the equilibrium state. Let's explore how the free energy changes at different temperatures. Only the entropy term changes with temperature. At low temperatures the double minima exists. As the temperature increases the magnitude of the entropy term becomes increasingly negative, eventually overpowering the enthalpy term and dominating the shape of the free

energy, t_2 in Fig. A.3. At these entropy dominated temperatures the double minima no longer exists and the equilibrium phase is a singe random solid solution phase.

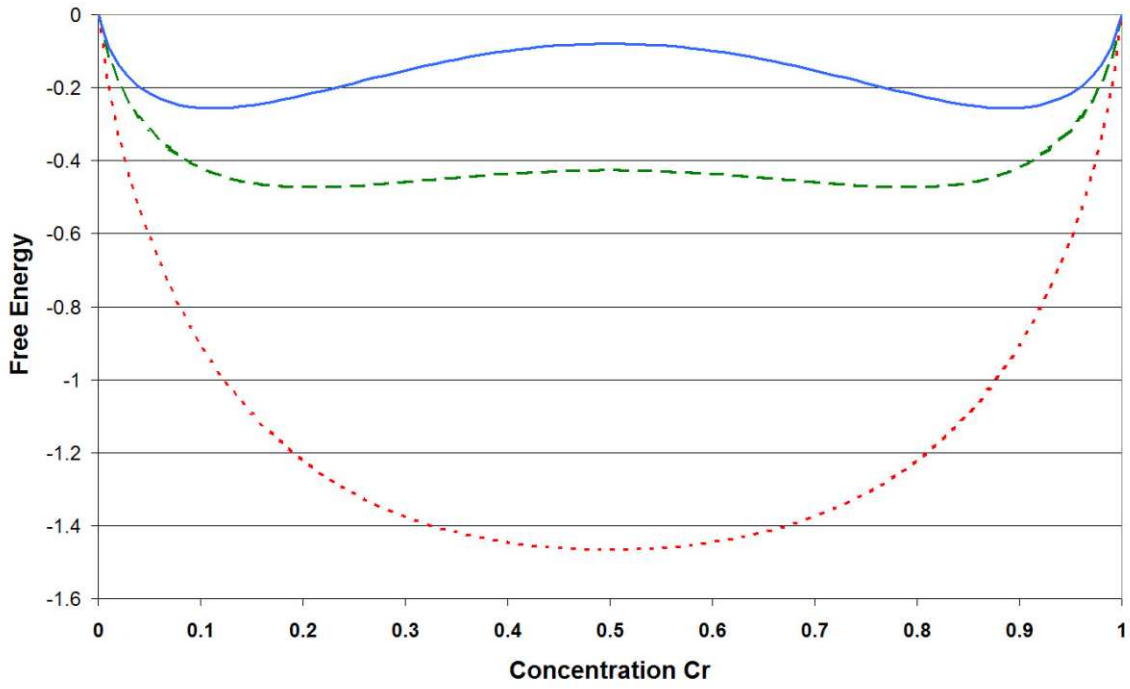

Figure A.3: The free energy of a spinodal system with increasing temperature. The double minima that exist at low temperatures disappears at the highest temperature. The solid line is t_0, the dashed line is at t_1, and the dotted line is at t_2 where $t_0 < t_1 < t_2$

The critical temperature for spinodal decomposition at composition χ occurs when the curvature of the free energy is zero at χ. Figure A.4 shows how the locus of these critical temperature points combine to make the miscibility gap that we see in phase diagrams.[1] Inside the miscibility gap the sample will chemically separate via spinodal decomposition. Because the curvature of the free energy is negative in this region, it is unstable and any fluctuation of composition will start a region of decomposition as the system moves toward the minima points in the free energy.

[1]The curvature of the free energy in these plots has been exaggerated for easier visualization of the $G"(\chi) = 0$ points.

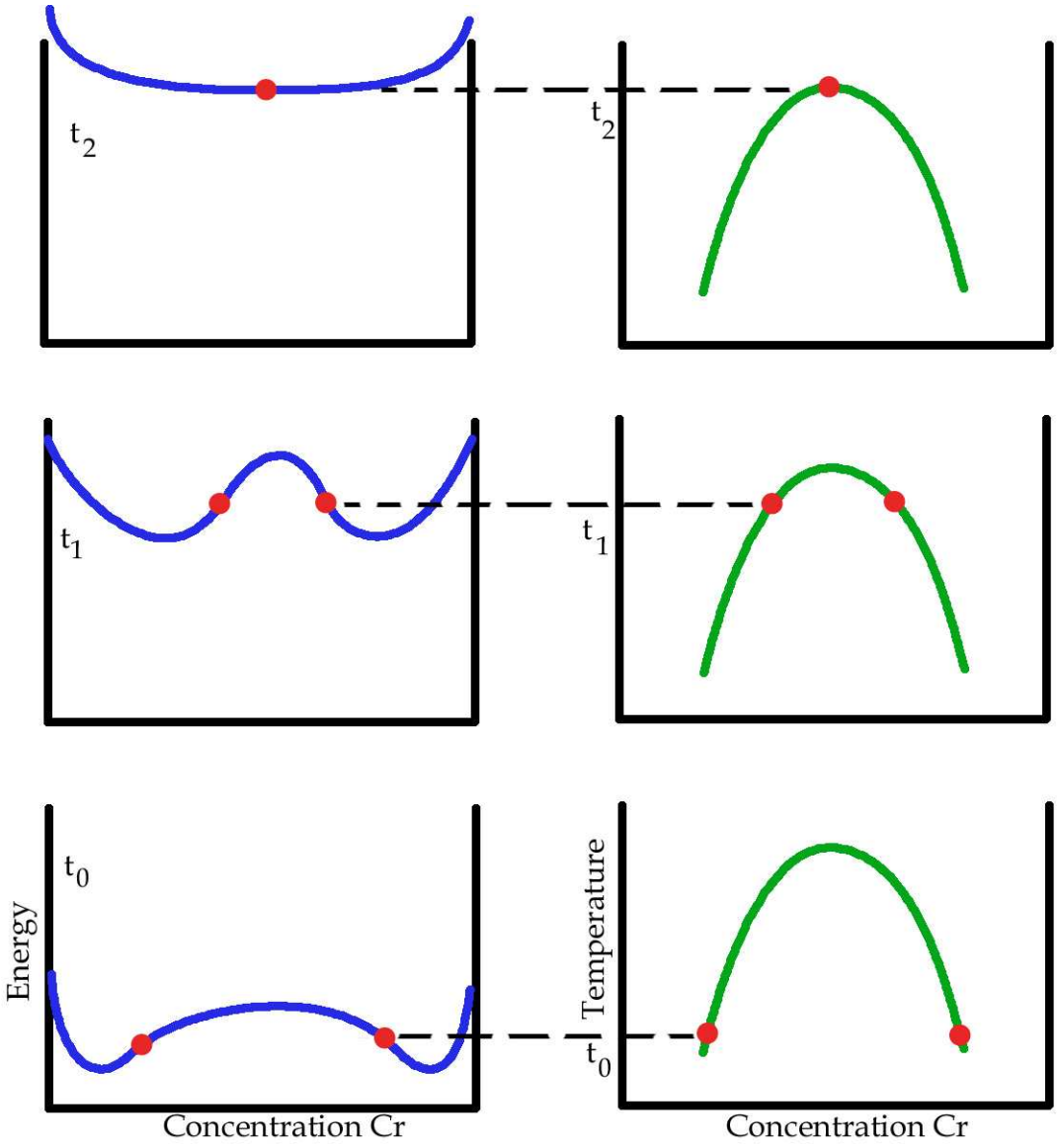

Figure A.4: Free energy curves are plotted on the left at various temperatures ($t_0 < t_1 < t_2$). The points on these graphs at which the curvature of the free energy is zero w.r.t. the concentration of Cr are noted with solid circles (red). These points correspond to points on the miscibility gap, which is plotted on the right.

Bibliography

[1] G. Albanese. *Phys. Rev. B*, 8:1315, 1973.

[2] L. Anthony, J. K. Okamoto, and B. Fultz. *Phys. Rev. B*, 70:1128, 1993.

[3] P. D. Bogdanoff and B. Fultz. *Philos. Mag. B*, 58:5897, 1998.

[4] P. D. Bogdanoff and B. Fultz. *Philos. Mag. B*, 81:299, 2001.

[5] P. D. Bogdanoff, B. Fultz, and S. Rosenkranz. *Phys. Rev. B*, 60:3976, 1999.

[6] P. D. Bogdanoff, T. L. Swan-Wood, and B. Fultz. *Phys. Rev. B*, 68:014301, 2003.

[7] J. Bogner, W. Steiner, M. Reissner, P. Mohn, P. Blaha, K. Schwarz, R. Krachler, H. Ipser, and B. Sepiol. *Phys. Rev. B*, 58:922, 1998.

[8] G. A. Botton, G. Y. Guo, W. M. Temmerman, and C. J. Humphreys. *Phys. Rev. B*, 54:1682, 1996.

[9] J. W. Cahn and J. E. Hilliard. Free energy of a nonuniform system interfacial free energy. *J. Chem. Phys.*, 28:258, 1958.

[10] J. W. Cahn and J. E. Hilliard. *J. Chem. Phys.*, 31:688, 1959.

[11] A. Cerezo, J. H. Hyde, M. K. Miller, S. C. Petts, R. P. Setna, and G.D. Smith. *Phil. Trans. R. Soc. Lond. A*, 341:313, 1992.

[12] 23H. Chachan, E. G. da Silva, D. Guenzburger, and D. E. Ellis. *Phys. Rev. B*, 35:1602, 1987.

[13] D. Chandra and L. H. Schwartz. *Metall. Trans.*, 2:511, 1971.

[14] Y. A. Chang, L. M. Pike, C. T. Liu, A. R. Bilbrey, and D. S. Stone. *Intermetallics*, 1:107, 1993.

[15] N. de Diego, F. Plazaola, J. A. Jiménez, J. Serna, and J. del Río. *Acta Metall.*, 53:163, 2005.

[16] D. de Fontaine. *Solid State Physics*, 34:73, 1979.

[17] D. de Fontaine. *Solid State Physics*, 47:33, 1994.

[18] R. E. Dingle and E. H. Medlin. *Acta Cryst. A*, 28:22, 1972.

[19] F. Ducastelle. *Order and Phase Stability in Alloys*. North-Holland, Amsterdam, 1991.

[20] R. J. Elliot and D. W. Taylor. *Proc. R. Soc. London, Ser. A*, 296:161, 1967.

[21] Mattias Forsblom, Nils Sandberg, and Göran Grimvall. *Phys. Rev. B*, 69:165106, 2004.

[22] B. Fultz. *Mössbauer Spectroscopy Applied to Magnetism and Materials Science Vol. 1.* Plenum, New York, 1993.

[23] B. Fultz, L. Anthony, L. J. Nagel, R. M. Nicklow, and S. Spooner. *Phys. Rev. B*, 52:3315, 1995.

[24] B. Fultz, L. Anthony, J. L. Robertson, R. M. Nicklow, S. Spooner, and M. Mostoller. *Phys. Rev. B*, 52.

[25] G. D. Garbulsky and G. Ceder. *Phys. Rev. B*, 49:6327, 1994.

[26] J. M. Grow, D. G. Howard, R. H. Nussbaum, and M. Takeo. *Phys. Rev. B*, 17:15, 1978.

[27] F. Güthoff, B. Hennion, C. Herzig, W. Petry, H. R. Schober, and J. Trampenau. *J. Phys. Cond. Matt.*, 6:6211, 1994.

[28] W. M. Hartmann, H. V. Culbert, and R. P. Huebener. *Phys. Rev. B*, 1:1486, 1970.

[29] J. M. Hyde, A. Cerezo, M. G. Hetherington, M. K. Miller, and G. D. W. Smith. *Surface Science*, 266:370, 1992.

[30] U. R. Kattner and B. P. Burton. *Phase Diagrams of Binary Iron Alloys*, volume 12–28. ASM International, Materials Park, OH, 1993.

[31] W. Keune and W. Sturhahn. *Hyperfine Interact.*, 123:847, 1999.

[32] R. Kikuchi. *Phys. Rev.*, 79:79, 1950.

[33] R. Kikuchi. *Phys. Rev.*, 81:988, 1951.

[34] Mineo Kogachi and Tomohide Haraguchi. *Mat. Sci. Eng.*, A230:124, 1997.

[35] T. Koyama, T. Miyazaki, and M. Mebed. *Metall. Mat. Trans. A*, 26A:2617, 1995.

[36] O. Kubaschewski. *Iron-binary phase diagrams*. Springer, Berlin, 1982.

[37] N. I. Kulikov, A. V. Postnikov, G. Borstel, and J. Braun. *J. Phys. Cond. Matt.*, 6:6211, 1994.

[38] J. S. Langer, M. Baron, and H. D. Miller. *Phys. Rev. A*, 11:1417, 1975.

[39] P. D. Mannheim. *Phys. Rev. B*, 165:1011, 1968.

[40] P. D. Mannheim. *Phys. Rev. B*, 5:745, 1972.

[41] P. D. Mannheim and S. S. Cohen. *Phys. Rev. B*, 4:3748, 1971.

[42] A. A. Maradudin. *Solid State Physics*, volume 18 p. 273 and volume 19 p. 1. Academic, New York, 1966.

[43] C.J. Martin and D. A. O'Connor. *Acta Cryst. A*, 34:500, 1978.

[44] A. J. McAlister. *Bull. Alloy Phase Diagrams*, 8(6):526–533, 1987.

[45] D. L. McDonald. *Acta Cryst.*, 23:185, 1967.

[46] B. Meyer, V. Schott, and M. Fähnle. *Phys. Rev. B*, 58:673, 1998.

[47] M. K. Miller. *Surface Science*, 246:434, 1991.

[48] M. K. Miller and M. G. Hetherington. *Surface Science*, 246:442, 1991.

[49] T. Miyazaki, A. Takeuchi, and T. Koyama. *J. Mater. Sci.*, 27:2444, 1992.

[50] P. Nagpal and I. Baker. *Metall. Trans.*, A21:2281, 1990.

[51] H. Nishimori and A. Onuki. *Phys. Rev. B*, 42:980, 1990.

[52] E. Obradó, L. Ma nosa, and A. Planes. *Phys. Rev. B*, 56:20, 1997.

[53] V. Ozoliņš and M. Asta. *Phys. Rev. Lett.*, 86:448, 2001.

[54] V. Ozoliņš, C. Wolverton, and A. Zunger. *Phys. Rev. B*, 58:5897, 1998.

[55] P. D. Pathak and N. P. Shah. *Indian J. Phys.*, 53A:283, 1979.

[56] G. Placzek and L. Van Hove. *Nuov. Cim.*, 1:233, 1955.

[57] S. S. Pohlong and P. N. Ram. *J. Phys. Cond. Matt.*, 10:10901, 1998.

[58] B. V. Reddy and S. C. Deevi. *Intermetallics*, 8:1369, 2000.

[59] L. Reinhard, J. L. Robertson, S. C. Moss, G. E. Ice, P. Zschack, and C. J. Sparks. *Phys. Rev. B*, 45:2662, 1992.

[60] T. Ruckert, W. Keune, W. Sturhahn, M. Y. Hu, J. P. Sutter, T.S. Toellner, and E. E. Alp. *Hyperfine Interact.*, 126:363, 2000.

[61] M. Seto, Y. Kobayashi, S. Kitao, R. Haruki, T. Mitsui, Y. Yoda, S. Nasu, and S. Kikuta. *Phys. Rev. B*, 61:420, 2000.

[62] Liu Shaojun, Duan Suqing, and Ma Benkun. *Phys. Rev. B*, 58:9705, 1998.

[63] W. M. Shaw and L. D. Muhlestein. *Phys. Rev. B*, 4:969, 1971.

[64] R. C. Shukla and C. A. Plint. *Phys. Rev. B*, 40:337, 1989.

[65] R. O. Simmons and R. W. Balluffi. *Phys. Rev.*, 117:52, 1959.

[66] M. H. Sluiter, M. Weiner, and Y. Kawazoe. *Phys. Rev. B*, 59:4100, 1999.

[67] G. L. Squires. *Introduction to the Theory of Thermal Neutron Scattering*. Dover, Mineola, New York, 1978.

[68] V. Sundarajan, B. R. Sahu, D. G. Kanhere, P. V. Panat, and G. P. Das. *J. Phys. Cond. Matt.*, 7:6019, 1995.

[69] L. A. Swanger, P. K. Gupta, and A. R. Cooper Jr. *Acta Metall.*, 18:9, 1970.

[70] A. Takeuchi, T. Koyama, and T. Miyazaki. *J. Jpn. Inst. Met.*, 57:492, 1993.

[71] M. D. Tiwari, K. M. Kesharwani, and Bal K. Agrawal. *Phys. Rev. B*, 7:2378, 1973.

[72] T. Tsakalakos. *Scripta Metall.*, 15:255, 1981.

[73] T. Ujihara and K. Osamura. *Acta Metall.*, 48:1629, 2000.

[74] A. van de Walle and G. Ceder. *Phys. Rev. B*, 61:5972, 2000.

[75] A. van de Walle and G. Ceder. *Phys. Rev. Lett.*, 86:5518, 2001.

[76] A. van de Walle and G. Ceder. *Rev. Mod. Phys.*, 74:11, 2002.

[77] A. van de Walle, G. Ceder, and U. V. Waghmare. *Phys. Rev. Lett.*, 80:4911, 1998.

[78] Y. Wang, L. Q. Chen, and A. G. Khachaturyan. *Acta Metall. Mater.*, 41:279, 1993.

[79] K. L. Weng, H. R. Chen, and Y. R. Yang. *Mater. Sci. Eng. A*, 379:119, 2004.

[80] R. O. Williams. *Trans. TMS-AIME*, 212:497, 1958.

[81] R. O. Williams. *Metall. Trans.*, 5:967, 1974.

[82] C. Wolverton and V. Ozoliņš. *Phys. Rev. Lett.*, 86:5518, 2001.

[83] R. Würschum, C. Grupp, and H.-E. Schaefer. *Phys. Rev. Lett.*, 75:97, 1995.

[84] S. Zaroual, O. Sassi, J. Aride, J. Bernardini, and G. Moya. *Mat. Sci. Eng. A*, 279:282, 2000.